

TECHNISCHE UNIVERSITÄT MÜNCHEN
Lehrstuhl für Physikalische Chemie

Scanning Tunneling Microscopic Studies of Nanostructures
at the Solid-Liquid Interface

Sarah Wieghold

Vollständiger Abdruck der von der Fakultät für Chemie der Technischen Universität
München zur Erlangung des akademischen Grades eines

Doktors der Naturwissenschaften

genehmigten Dissertation.

Vorsitzender: Prof. Dr. Hubert Gasteiger
Prüfer der Dissertation: 1. Priv.-Doz. Dr. Friedrich Esch
2. Prof. Dr. Reinhard Nießner

Die Dissertation wurde am 27.06.2016 bei der Technischen Universität München
eingereicht und durch die Fakultät für Chemie am 02.08.2016 angenommen.

Die Neugier steht immer an erster Stelle eines Problems, das gelöst werden will.
Galileo Galilei (1564-1642)

Contents

List of Acronyms	7
Abstract	9
Zusammenfassung	10
1 Introduction	11
1.1 Motivation	11
1.2 Scope of the work	14
1.3 Thesis Outline	16
2 Methods and Background	18
2.1 Surface Preparation Techniques	18
2.1.1 Supramolecular Networks	18
2.1.2 Self-Assembled Monolayers	22
2.1.3 Supported Particles	26
2.2 Scanning Tunneling Microscopy	29
2.2.1 Background on Scanning Tunneling Microscopy	29
2.2.2 Principles of Optically-Assisted STM	31
2.2.3 Electrochemical STM	34
2.3 Electrochemical Methods	37
2.3.1 Cyclic Voltammetry	37
2.3.2 Rotating Disk Electrode	39
3 Experimental Background	41
3.1 ECSTM Setup	41
3.1.1 STM-head and STM-base	41
3.1.2 Electrochemical cell	42
3.1.3 Modification of the setup	42
3.1.4 Tip Preparation	44
3.1.5 Tip coating	45
3.1.6 Electrochemical STM Measurements	46
3.1.7 Photoresponse Measurements	47
3.2 Optically-Assisted STM	49
3.3 Rotating Disk Electrode Setup	49

4 Self-Assembly on All-Carbon Substrates Towards Photovoltaics	51
4.1 Three-Dimensional Bicomponent Supramolecular Nanoporous Self-Assembly on a Hybrid All-Carbon Atomically Flat and Transparent Platform	51
4.2 Photoresponse of Supramolecular Self-Assembled Networks on Graphene - Diamond Interfaces	63
4.3 Conclusion	75
5 Conclusion and Outlook	77
References	81
List of Figures	91
List of Tables	92
Acknowledgements	93
List of Publications	95
Appendix	97

List of Acronyms

AC	alternating current
AFM	atomic force microscopy
Ar	argon
C-100	diamond (100)
CdS	cadmium sulfide
CE	counter electrode
CNT	carbon nanotubes
CV	cyclic voltammetry
CVD	chemical vapor deposition
DC	direct current
DI	deionized water
DMF	N,N-dimethylformamide
DMSO	dimethyl sulfoxide
DOS	density of states
DSSC	dye-sensitized solar cells
EC	electrochemistry
ECSA	electrochemical active surface area
EG	ethylene glycol
EGaIn	eutectic gallium-indium
g	graphene
Ga	gallium
GC	glassy carbon
GHD	graphene transferred on hydrogenated diamond
HMRD	hanging meniscus rotating disk
HOPG	highly oriented pyrolytic graphite
HPLC	high-performance liquid chromatography
LED	light-emitting diode
LDOS	local density of states
MB	methylene blue

Mel	1,3,5-triazine-2,4,6-triamine
MMA	methyl methacrylate
NMR	nuclear magnetic resonance
NP	nanoparticle
NTCDI	1,4,5,8-naphthalenetetracarboxylic diimide
PEMFC	proton exchange membrane fuel cells
PTCDI	3,4,9,10-perylenetetracarboxylic diimide
PTFE	polytetrafluoroethylene
PV	photovoltaic
QD	quantum dots
RDE	rotating disk electrode
RE	reference electrode
RHE	reversible hydrogen electrode
SAM	self-assembled monolayer
SEM	scanning electron microscope
SHE	standard hydrogen electrode
SMA	single molecule absorption
STM	scanning tunneling microscopy
STS	scanning tunneling spectroscopy
TDI	terrylene diimide
TIR	total internal reflection
UHV	ultrahigh vacuum
UPD	underpotential deposition
vdW	van der Waals
WE	working electrode

Abstract

Supported nanostructures on novel support materials attract great attention in the development of tunable conversion and storage systems for renewable energy vectors. Their great potential is related to a high material efficiency and properties that can be tuned by size, shape and interaction with support and solvents. However, advanced preparation methods are required to overcome limitations regarding the ordering of the active layer as well as its stability.

In this thesis, several approaches are explored to generate stable functional nanostructures at the solid-liquid interface: i) Bottom-up self-assembly of hydrogen-bonded, porous mono- and bilayer networks for cluster and nanoparticle trapping; ii) Implementation of all-carbon, transparent films that support ordered, photoabsorbing organic monolayer networks with photovoltaic response; iii) Immobilization of Pt clusters on engineered, transparent Au films for indirect plasmonic activation; iv) Immobilization of wet-chemically synthesized Pt nanoparticles on self-assembled thiol monolayers on Au for electrocatalysis with tunable decoupling from the substrate.

All these nanostructures were studied in a twofold way - on the atomic scale by scanning tunneling microscopy techniques, as well as on the macroscopic scale by investigating the photovoltaic, photocatalytic or electrocatalytic activity. In this way, a sustainable platform for fundamental studies of supported nanostructures at the solid-liquid interface could be established that links mechanistic insight to performance.

Zusammenfassung

Nanostrukturierte Materialien, geträgert auf neuartigen Substraten, sind interessant für die Entwicklung von Speicher- und Energieumwandelungssysteme für erneuerbare Energietechnologie. Ihr großes Potential ist der hohen Effizienz der Materialien, sowie deren Eigenschaften geschuldet, welche durch Größe, Struktur und Wechselwirkung mit Trägermaterialien und Lösungsmitteln optimiert werden können. Allerdings erfordern diese Materialien neuartige Herstellungsmethoden, um die Limitierung, welche durch die Ordnung von aktiven Schichten und deren Stabilität entsteht, zu überwinden.

In dieser Arbeit werden verschiedene Herangehensweisen zur Herstellung von stabilen, funktionalen Nanostrukturen an der fest-flüssig Grenzfläche getestet: i) Selbstorganisation von porösen, ein- und zweilagigen Netzwerken, die durch Wasserstoffbrückenbindungen stabilisiert werden, zur Verankerung von Clustern und Nanopartikeln; ii) Implementierung transparenter Filme auf Kohlenstoffbasis auf denen geordnete, einlagige organische Netzwerke mit photovoltaischen Eigenschaften aufgebracht werden können; iii) Immobilisierung von Pt Clustern auf transparenten Goldfilmen für indirekte plasmonische Aktivierung; iv) Immobilisierung von nass-chemisch hergestellten Pt Nanopartikeln auf selbstorganisierenden Thiol-Schichten auf Gold für Elektrokatalyse mit systematischer Entkopplung vom Trägermaterial.

Alle nanostrukturierten Systeme wurden auf der atomaren Skala mit Hilfe von Rastertunnelmikroskopie sowie auf makroskopischer Skala charakterisiert, wobei die photovoltaische, photokatalytische oder elektrokatalytische Aktivität untersucht wurde. So wurde ein Modellsystem für Grundlagenstudien an der fest-flüssig Grenzfläche von geträgerten Nanomaterialien geschaffen, mit dessen Hilfe mechanistische Informationen mit katalytischer Aktivität korreliert werden können.

1 Introduction

1.1 Motivation

The continued rise of world's energy consumption causes one of the biggest challenges in nowadays society, namely to replace fossil fuel with renewable energy sources [1]. The supply of clean and sustainable energy without creating any additional CO₂ is of major importance concerning the world energy consumption and to prevent increasing greenhouse gases [2]. To achieve a change in today's power generation, new methods are required which include the development of new materials to increase energy conversion and the overall efficiency. Renewable energy sources show an uptrend reaching a record of 3% of global energy consumption, especially the generation of energy by solar power grew notably by 38% [3]. This positive trend of using renewable energy resources will continue during the next decades [4]. Particularly with a view of the world's total energy consumption, this tendency in generating electricity out of renewable energy resources is indispensable since it will increase by approximately 41% until 2030 [3]. Therefore, the need arises to address today's energy problems in order to compensate the world's increasing energy demand.

Today, one of the most important renewable energy source is solar power. The sun is an excellent energy distributor which can be used world-wide due to a uniform distribution of photons all over the Earth [5]. The sunlight can be converted into different forms of energy: electricity and chemical fuels.

Photovoltaics (PVs) are widely employed to convert solar energy into electricity. Photons excite electrons across a bandgap of a semiconductor and thereby create electron-hole pairs (excitons) which are split at a p-n interface where the single electrons and holes travel in opposite directions to their respective electrode. These charge carriers are collected at the electrode, electricity is generated. Nowadays, the best commercially available PVs are based on silicon single-crystals with a conversion efficiency of about 18% [5]. However, one could achieve much better efficiencies. On the laboratory scale, PVs generate efficiencies up to 45% [6]. Unfortunately, the up-scaling for routine use at large scales is nearly impossible due to the tremendous costs of the material.

Alternatively, chemical fuels can be generated in **photocatalysis**. In 2015, a breakthrough in photocatalysis was achieved for the direct solar-to-hydrogen conversion by photooxidation of water [7, 8, 9] yielding a new record conversion efficiency of 14% [10]. Notably, this new record conversion efficiency was only 1.7% higher than the last record which was achieved 17 years ago [11].

This slow increase in efficiency as well as the tremendous costs of material reflects the challenge in improving and developing new stable materials for solar energy conversion system. To further increase the efficiency (in PVs as well as in photocatalysis), the improvement will be enabled by the growing ability to understand and control the fundamental nanoscale processes [5]. These processes at the atomic level are responsible for an effective conversion of photons into electricity or chemical fuels. Hence, different research fields have been dedicated to develop new stable materials [9, 12, 13] and understand the basic principles which prevail in these energy conversion systems.

One promising approach to understand the fundamental details at the interface is based on a **bottom-up strategy**. Bottom-up strategies use techniques e.g. molecular synthesis or colloid chemistry to make structures with nanometer dimension [14]. These nanostructures represent an excellent platform and are simple model systems to study the underlying processes at an atomic level. By using these nanostructures, the dimensions of the systems can be reduced allowing for a detailed characterization, e.g. nanostructure-support interactions at the interface. These structures exhibit tunable properties and include materials as: dyes, clusters, nanoparticles, metal complexes as well as layers of organosulfur compounds. By changing their structure, their absorption properties are changed [9]. Further, engineering novel materials bear the potential of stable materials with an increased efficiency and low costs. Nowadays, these structures are already employed as absorber materials [7, 9, 15], (photo)electrocatalysts [16, 17, 18] or for tailoring surface properties [19, 20].

However, their achieved conversion efficiencies of photons into electrons or hydrogen in these systems are far below their theoretical limits. One of the main problems causing the low conversion efficiency is related to the stability and the ordering of the nanostructures on the respective surface. Whereas the overall (catalytic) efficiency is mainly influenced by the stability of the nanostructures, the charge carrier mobilities are related to their ordering at the interface.

In the following, three approaches are presented to overcome the limitations regarding the stability and ordering of the nanostructures in PVs and (photo)electrocatalysis. Possible strategies are shown in order to improve the stability of the nanostructures as well as develop novel platforms for studying the interface processes:

1. PVs can be employed to generate electricity by the conversion of photons into electrons. According to literature [7, 8, 9], the low photon-to-electron efficiency is attributed to a low ordering of the active molecules at the interface. In these studies, the active molecules are assembled onto the surface using a blending technique. However, this technique has several

- disadvantages: the molecules crystallize out of solution and form multilayers at the surface [7]. In order to address this problem, a bottom-up strategy bears the potential to control the deposition process of nanostructures at the solid-liquid interface. Especially the process of self-assembly allows to form ordered patterns at the solid-liquid interface out of the building blocks in solution [21]. In this process, a stable monolayer is formed at the support-solvent interface [21, 22, 23]. For the self-assembly process, different kinds of support materials can be employed including carbon, gold or silver supports enabling one to change (and tune) the nanostructure-support interactions [24, 25, 26]. In this thesis, the self-assembly process of dye molecules in a supramolecular bicomponent network configuration is studied on all carbon-supports, including highly oriented pyrolytic graphite (HOPG), graphene supported on Cu and graphene supported on hydrogenated diamond (GHD). GHD is developed as novel platform for PVs to study the photon-to-electron conversion of supported network monolayers. On this support, the active network molecules can be excited via a back illumination geometry.
2. The second approach deals with the generation of chemical fuels in electrocatalytic systems. In these systems, platinum nanoparticles are widely employed due to their ease in preparation using a wet-chemical approach [27, 28]. According to literature, only small amounts of platinum are required to catalyze the important hydrogen oxidation and evolution reaction (HOR/HER) in proton exchange membrane fuel cells (PEMFC) [29, 30]. However, during operation a decrease in efficiency is observed which can be related to a change in morphology of the particles [31, 32, 33, 34]. Hence, there is a great interest in studying the underlying processes which are responsible for the morphology change of the supported particles. In general, the particles are supported on a carbon substrate. However, carbon is not stable up to high potentials; carbon corrosion occurs. As a replacement of carbon, gold single crystals can be used. Gold is an excellent platform since it is inactive over a wide potential range [35]. Further, these gold supports bear the potential of a tunable platform due to the possibility of surface modifications. One prominent candidate for these modifications is based on thiolate self-assembled monolayers (SAMs) in which thiols or thiocyanate molecules can be assembled on a gold substrate [20, 36]. These SAMs can be used as spacer molecules and thus, decouple the properties of the particles and the support. Another advantage of using SAMs is that they reduce capacitive currents [37] in the system which enables a more detailed investigation at the interface. In this thesis, the stability of small platinum nanoparticles on a bare gold surface as well as on a

self-assembled monolayer in electrochemical experiments is investigated.

3. The last approach focuses on photocatalytic systems based on small platinum clusters which are supported on a transparent thin gold film. Platinum is one of the most important materials in catalytic applications [28, 29, 30]. Concerning especially photocatalysis, small platinum clusters have an absorption which is not located in the visible range of the spectrum. However, it would be advantageous if one could shift the absorption peak into the visible range which enables their use in today's photocatalytic applications. One approach of exciting these metal clusters is based on plasmonic photocatalysis. Here, a plasmonically active support is employed which can be excited with visible light under total internal reflection (TIR) at the interface. In this thesis, a plasmonic excitation of a gold support is transferred into a localized surface plasmon resonance of small platinum clusters. The enhanced indirect activity of the supported clusters can be used for photocatalytic reactions e.g. oxidative decomposition of dyes under ambient conditions.

1.2 Scope of the work

The main questions which are addressed in this work are related to the formation of stable and extended stable structures at interfaces. It is of special interest to tailor the properties of the supported nanostructures allowing for a systematic and detailed characterization of the nanostructure - support interactions. Especially, two phenomena of supported nanostructures are in the main scope of this thesis - the interaction of light and the stability in electrocatalysis.

In order to gain insights into these phenomena, and thereby to their linked mechanistic details at the solid-liquid interface, three nanostructured systems are employed for energy conversion at surfaces:

- A) **self-assembly** process of dye molecules in PVs and their **photon-to-electron conversion**,
- B) **SAM formation** on gold and their use as support for **nanoparticles** in **electrocatalysis**, and
- C) **indirect plasmonic activation** of clusters in **photocatalysis**.

For studying the supported nanostructures, local and integral techniques are used. A setup of an Electro-Chemical Scanning Tunneling Microscope (ECSTM) is built which allows for surface sensitive experiments. In addition, electrochemical methods, cyclic voltammetry (CV) and rotating disk electrode (RDE) techniques are used to study the catalytic behavior of the nanostructures in aqueous electrolytes. Single molecule absorption detected by STM (SMA-STM) is used to

study the plasmonic coupling of surface plasmons into the nanostructure. An overview of the nanostructures and systems used in this thesis is shown in Fig. 1.

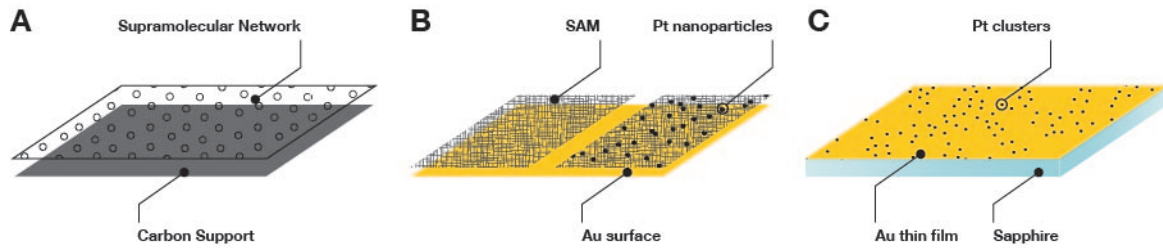


Figure 1: Overview of the used systems in this work. A) supramolecular network formation on different carbon supports, B) self-assembled monolayer formation on gold and its use as support for platinum nanoparticles and C) transparent thin gold films as support for platinum clusters. Image: F. F. Schweinberger.

In the first system (Fig. 1A), a supramolecular network formation on different carbon supports is studied. The results are summarized in two publications: **'Three-dimensional bicomponent supramolecular nanoporous self-assembly on a hybrid all-carbon atomically flat and transparent platform'** and **'Photoresponse of supramolecular self-assembled networks on graphene-diamond interfaces'** in section 4. A bottom-up approach is used to precisely organize the building blocks on a carbon support allowing for detailed investigations at the interface. It is of special interest to study the ordering of the molecules forming a supramolecular bicomponent network at the solid-liquid interface and to extract crucial parameters as network growth rate both in plane and perpendicular to the surface. In order to characterize the photoresponse (photon-to-electron conversion) of the supramolecular monolayer, a method is implemented which allows for a macroscopic characterization of the network under monochromatic illumination.

In the second system (Fig. 1B), a gold surface is employed to study the formation of a SAM. This SAM support is used in a subsequent step as support for platinum nanoparticles. The results are presented in the manuscript **'Mechanistic details on the flattening mechanisms of supported platinum nanoparticles on gold and thiol-terminated self-assembled monolayers'** (Appendix B). The self-assembly process is used to form an ordered and densely packed thiol film on the gold surface. It is of interest to investigate the SAM stability under various preparation conditions. These SAMs are used in a next step as support for Pt nanoparticles in electrochemical experiments. New insights into the mechanistic details on the stability in electrochemical experiments are observed and validated by kinetic Monte Carlo simulations.

In the third system (Fig. 1C), a transparent ultrathin gold surface is used as support for platinum clusters. The results are summarized in the manuscript '**Plasmonic activation of 1 nm platinum clusters for photocatalysis**' (Appendix B). Here, a special focus is placed on the indirect coupling behavior of gold surface plasmons into small metal clusters. In order to get informations of the activity, a photocatalytic decomposition reaction of dye molecules is performed.

1.3 Thesis Outline

This cumulative doctoral thesis is based on scientific papers resulting from my work as a doctoral candidate at the Chair of Physical Chemistry. A graphical overview of the chapters is presented in the roadmap at the end of this chapter in Fig. 2.

After a general introduction of supported nanostructures, the preparation techniques of supramolecular chemistry, the formation of self-assembled monolayers as well as supported nanoparticles are described in the first part of the **Methods and Background** section. In the following subsections, the principles and basic knowledge on STM are presented. Here, two variants of the STM, namely ECSTM and SMA-STM are introduced. The last part of this section focuses on electrochemical methods, CV and RDE experiments. Here, electrochemical equations as well as their explanations are summarized.

The **Experimental** section gives an overview of the employed ECSTM setup which was build at the beginning of this PhD work. A special focus is placed on the setup modifications as well as on the preparation steps which have to be performed prior to start experiments. In addition, the photoresponse measurements, the setup of the optically-assisted STM and the electrochemical setups are described.

In the **Results** section, the assembly process on all-carbon based substrates towards photovoltaics is presented. This section is based on two publications with a special focus on the stability and formation of a supramolecular bicomponent network at the solid-liquid interface. In addition, the optical properties including photoresponse experiments are presented. This work was performed in a collaboration with the group of Prof. J. Barth, E20 at the Physics Department of TUM.

Finally, an overall conclusion and outlook is given in the **Conclusion and Outlook** concerning my whole work at the chair of Physical Chemistry at TUM.

The **Appendix** is divided into two parts, **Appendix A** and **Appendix B**. In part A, additional

STM parameters (RHK and STS parameters and piezo calibration values) are listed. In part B, two manuscripts are presented. The first manuscript is based on the flattening mechanism of supported platinum nanoparticles on a bare gold as well as on a SAM modified gold support.

The second manuscript summarizes the results of optically excited platinum clusters on a thin gold film. This work was performed in a collaboration with the group of Prof. M. Gruebele, Department of Chemistry and Beckman Institute at the University of Illinois at Urbana-Champaign, USA.

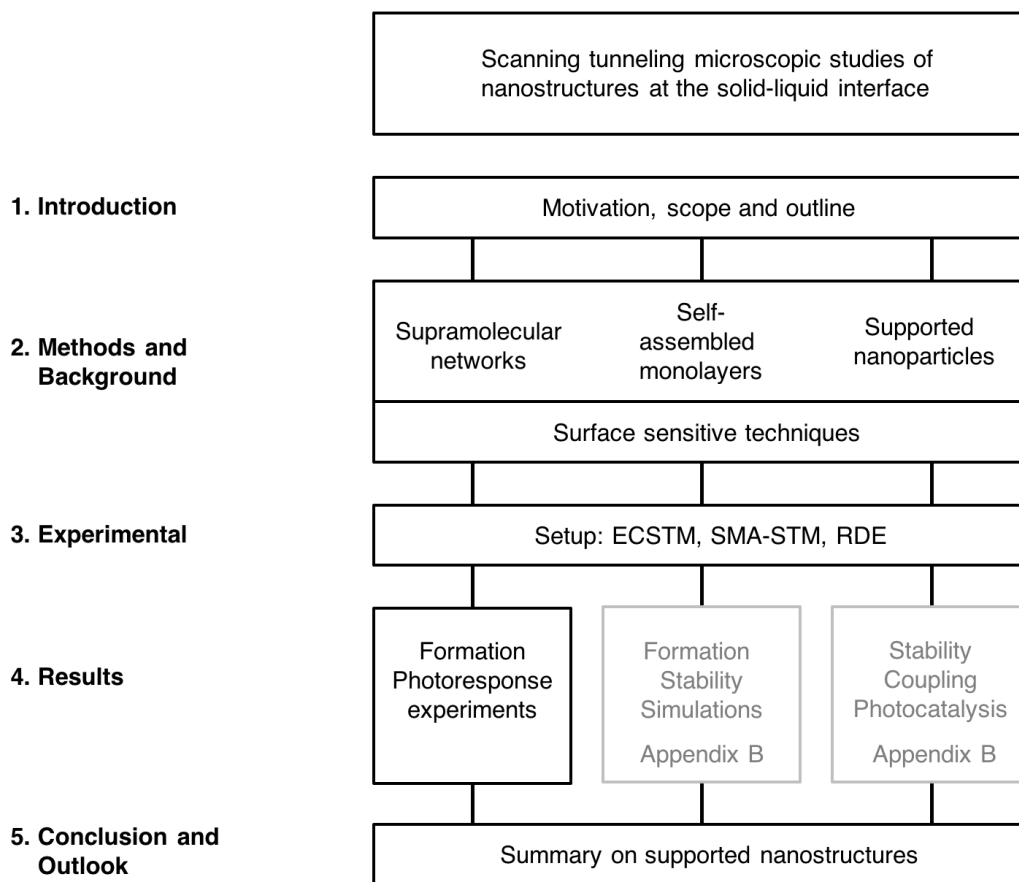


Figure 2: Roadmap of the thesis. The respective sections are listed on the left. The topic is shown in the right column.

2 Methods and Background

2.1 Surface Preparation Techniques

2.1.1 Supramolecular Networks

Supramolecular chemistry refers to the term of molecular assemblies based on noncovalent bonds which can be grown at interfaces [21, 22, 23] towards robust, modular and predictable two-dimensional (2D) optoelectronic materials. In supramolecular chemistry, the network formation is based on intermolecular interactions which include electrostatic, intermolecular and van der Waals forces (vdW) or hydrogen bondings. Here, hydrogen bonded networks are prominent candidates to form well-ordered long-range architectures.

Hydrogen bonds exhibit an ideal interaction to grow architectures from the bottom-up since they are highly selective and directional [38]. These hydrogen bonded networks are formed by a donor and an acceptor molecule. The donor must provide an acidic hydrogen atom that can interact with the nonbonding electron lone pair of the acceptor molecule. These hydrogen bonded networks can be formed via a single, double or triple H-bonding interaction. Networks formed of single H-bonds exhibit more closely packed domains than double or triple H-bonded networks. Further, these single H-bonded architectures show a less stable behavior in air compared to higher H-bonded networks [24, 39]. However, for self-assembling bicomponent networks, a triple H-bonding interaction is required. In the following, a closer look into bicomponent networks is taken:

For self-assembling bicomponent networks, a cornerstone often based on 1,3,5-triazine-2,4,6-triamine (melamine), is employed due its planar and highly symmetrical triangle shape [40]. The recognition of the moieties is based on a complementary triple hydrogen bond formation between melamine and the termination of the linker molecule e.g. diimide [41], carboxylic [39] or carbonitrile groups [42]. A major advantage of this molecular self-assembly based on triple H-bonds is that the layer can have a variety of structures and potential functionalities on many length scales, depending on the choice of building blocks [43, 44, 45, 46]. However, whereas the formation under ultrahigh vacuum (UHV) conditions is straightforward [47], the formation at the liquid-solid interface is more challenging due to phase segregation and polymorphism [25]. Especially the ordering of the molecules at the interface is of major importance since it determines the electronic properties of the layer. Hence, the major challenge which has to overcome prior using a bicomponent network as optoelectronic material in e.g. light-emitting diodes (LEDs)

[48] or photovoltaics (PV) [8], is to get a detailed molecular-level understanding of the ordering process at the interface which also enables a layer-by-layer growth. A great effort has been made of growing such bicomponent supramolecular structures at equilibrium conditions at carbon and gold interfaces. In the following, the progress as well as the challenges of supramolecular bicomponent H-bonded supramolecular networks based on triple H-bonds are addressed.

The first explored bicomponent network at the solid-liquid interface was studied by Madueno *et al.* [24] using melamine and perylene-3,4,9,10-tetracarboxylic diimide (PTCDI) in dimethylformamide (DMF) on a gold surface. A long-range ordered network exhibiting a honeycomb structure was imaged by STM and Atomic Force Microscopy (AFM). However, the network structure was not stable and hence, not reproducible in air. Further developments in the self-assembly process allowed to successfully produce a stable network using melamine and 1,3,5-triazine-2,4,6-triol (cyanuric acid) on HOPG [40] under thermodynamic control. Here, for the first time stacked monolayers forming 3D architectures were observed by employing a higher concentration of melamine and cyanuric acid. This potential of stackability of monolayers had a groundbreaking impact for today's 3D architectures in photovoltaic systems [40]. However, one could not obtain the control of these 3D architectures and hence, they were randomly oriented on the surface. Further investigations in this system revealed that phase segregation and polymorphism [25] hindered an ordered network growth in the third dimension.

In order to address these problems concerning the ordering and layer-by-layer growth of a network, one approach is presented in the results section 4.1: 'Three-dimensional bicomponent supramolecular nanoporous self-assembly on a hybrid all-carbon atomically flat and transparent platform'. Here, the supramolecular network formation of melamine and 1,4,5,8-naphthalene-tetracarboxylic diimide (NTCDI) on HOPG in trichlorobenzene (TCB) is studied (also compare Fig. 3 for an overview of the network structure of melamine and NTCDI). It is of special interest, to study the ordering of the network on the surface depending on the solvent polarity as well as on the molecular concentration of the mixture (ratio melamine:NTCDI). By studying this concentration dependency, new insights into the phase segregation of the molecules on the surface could be gained. In addition, nowadays, supramolecular structures can be grown on different kinds of materials (HOPG, Au and Ag) and even more important, on electronically relevant transparent substrates e.g. supported graphene sheets [26]. Hence, the network formation of melamine and NTCDI is also studied on supported graphene on hydrogenated diamond (GHD) in order to study the ordering on a more technologically relevant support. This support enables the use in photovoltaic experiments due to the transparency which allows for a backside

illumination geometry.

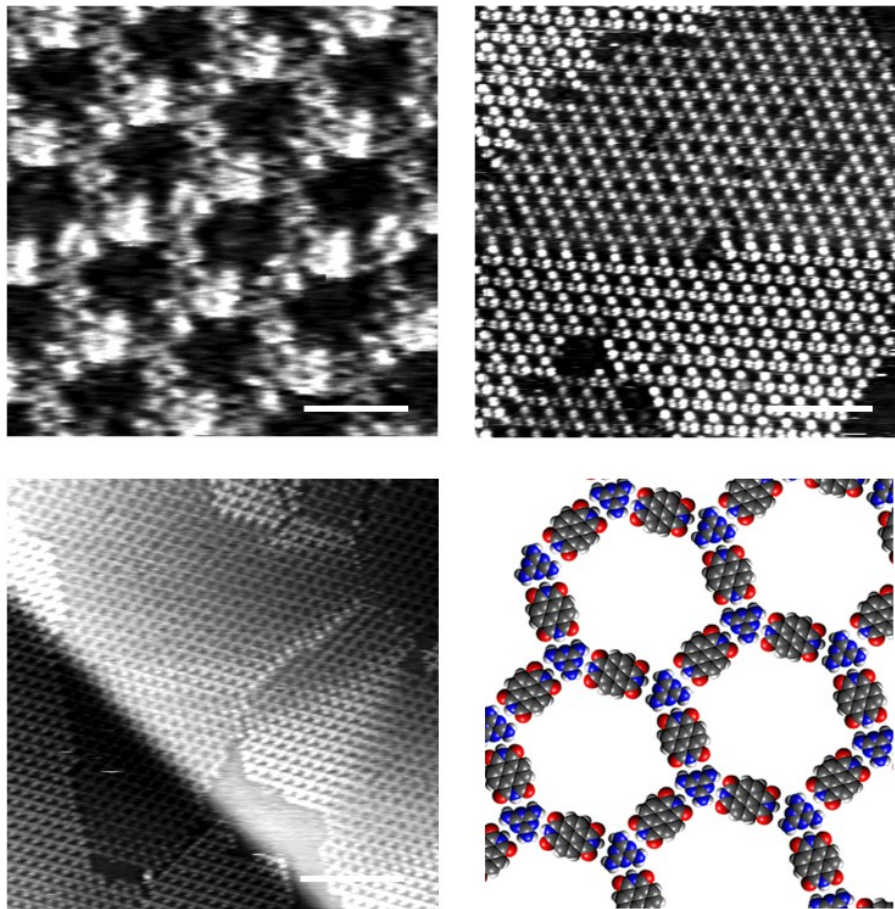


Figure 3: Supramolecular bicomponent network formation of melamine and NTCDI on HOPG. Scale bars: left top 3 nm, right top 15 nm, left bottom 30 nm. Right bottom: molecular model, blue: melamine, grey: NTCDI.

Besides investigating novel platforms for the self-assembly and the network formation process itself, engineering novel absorber materials bear the potential to increase and improve the efficiency for e.g. PVs [9]. Extended π -conjugated systems can be tuned in their absorption properties by changing the scaffold structure and thus, causing a red- or blue-shift in the absorption peak maximum. Here, rylenes, poly(*peri*-naphthalene)s, are prime candidates in the field of dye chemistry [9]. Their basic structure consists of a NTCDI core which can be extended by additional benzene rings and substituted in the *peri* and/or *bay* position (Fig. 4). The simplest rylene dye is perylenediimide (PDI). Rylenes exhibit an outstanding performance regarding photo-, thermal- and chemical stability as well as high extinction coefficients [49].

Rylenes have been employed in photonic applications such as solar energy converter, lasers or organic PV [9]. Here, first experiments (in 1996) achieved power conversion efficiencies up to 1% [8] using a perylene dye in combination with phthalocyanines in a two-layer organic PV

configuration. In 2013, so far, the best known power conversion efficiency of 3% was reported for a bulk heterojunction using PDI as an acceptor [7]. This poor power conversion efficiency was attributed to the tendency of PDIs to crystallize in solution resulting in a non-ordered formation on the surface.

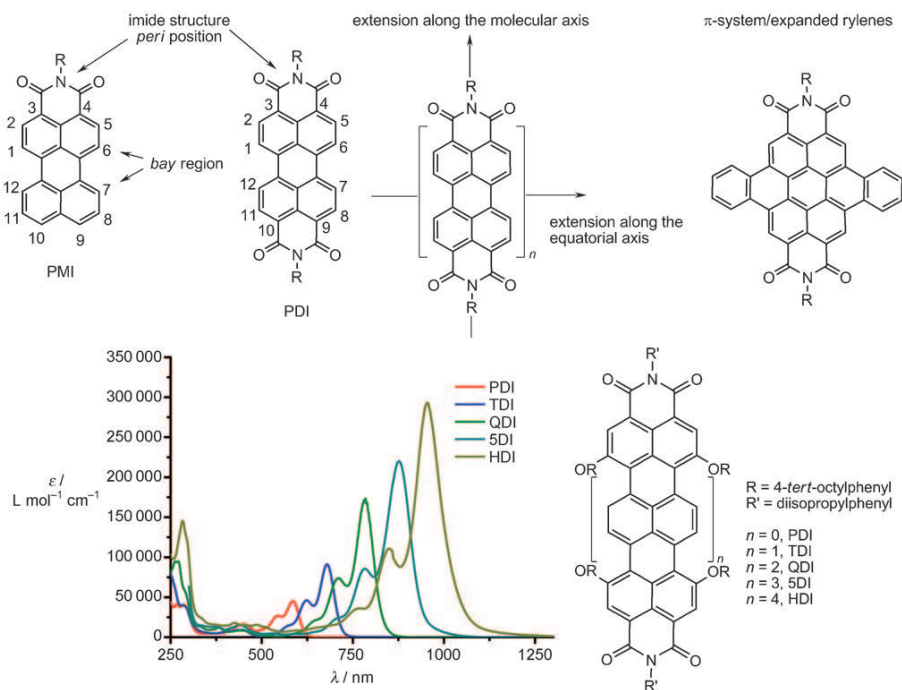


Figure 4: Chemical structures of peryleneimide and its derivatives and corresponding absorption spectra. Reprinted with permission from T. Weil, T. Vosch, J. Hofkens, K. Peneva, K. Müllen, *Angew. Chem. Int. Ed.* 2010, 49, 9068-9093, Copyright © 2010 WILEY-VCH Verlag GmbH & Co. KGaA, Weinheim.

In order to further improve the stability of the active materials as well as increase the power conversion efficiency in PVs, one approach is presented in section 4.2: 'Photoresponse of supramolecular self-assembled networks on graphene-diamond interfaces'. A rylene derivate, namely terylene diimide (TDI) is employed as active material in a bicomponent network configuration with melamine. The network stability is studied on all-carbon supports - HOPG, graphene supported on copper and GHD. This novel platform of using GDH allows one to measure photon-to-electron conversion efficiencies in a back illumination geometry. For measuring the photoresponse of the formed monolayer, a technique is implemented by using a top electrode which can softly contact the monolayer. By employing this top electrode, made of gallium or eutectic gallium-indium (EGaIn), the photoresponse of the monolayer under constant light illumination can be measured.

The advantage of using EGaIn (over pure Ga) is that EGaIn has a lower melting point which allows to form the top electrode droplet. EGaIn shows a metallic behavior and if exposed to air, a roughly 1 nm thick oxide layer (Ga_2O_3) is formed [50]. This layer can be described as flexible but incompressible layer consisting of locally buckled and inclosing small lumps of gallium oxide [51, 52]. The nature of this 'liquid' top electrode allows to contact the monolayer. The photogenerated carriers can be collected with the top electrode and the photon-to-electron conversion efficiency can be estimated.

2.1.2 Self-Assembled Monolayers

Self-assembled monolayers (SAMs) are formed through the spontaneous formation of molecular arrangements at the interface. In comparison to the self-assembly process of network structures, as described in section 2.1.1., where extended architectures can be grown horizontally on a surface by rather exhibiting weak interactions with the support, the formation of SAMs includes linking the molecules to the surface by a strong bond [20].

SAMs have shown their potential in various nanotechnology applications, e.g. sensors [53], molecular motors [54] or in biological systems [55]. Besides their use as 'active' element, they are widely employed as passivating material, including in gold nanoparticle (NP) synthesis [56], lithography [57] or molecular electronics (due to metallization of the surface [58]). Further, for supported systems (e.g. nanoparticles on SAMs), SAMs act as a spacer layer and thus, the properties from the particles and the substrate can be decoupled. This is of major interest in electrochemistry because the SAM layer can reduce double-layer charging currents [37]. By employing a SAM, even small features of the supported metal particles can be seen in electrochemical measurements due to a reduced capacitive current (- the general trend is a decrease of the capacitive current as the chain length is increased [37]).

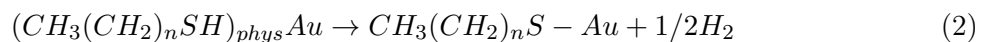
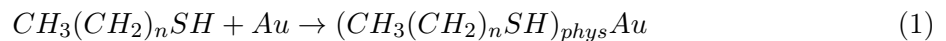
The most studied SAMs are made of thiols or dithiols on Au which have been discovered in 1983 by Nuzzo *et al.* [59]. Their recognition is based on the strong sulfur-gold bond (S-Au bond 50 kcal mol^{-1} [20]) which make them easy to use in preparation processes while exhibiting high stability. The building block molecule, can be divided in three parts: a headgroup (linking group), backbone (main chain) and a specific terminal group (end group).

While the headgroup forms a strong bond with the surface, vdW interactions between the chains allow for a densely packing of the monolayer. The end group defines the chemical properties of the phase boundary of the SAM modified support [20, 36]. These terminal end groups allow

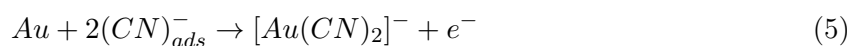
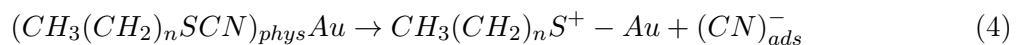
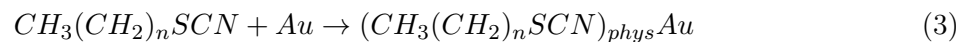
to modify the physical and chemical properties of the phase boundary. Thus, the SAM layer properties can be tuned from e.g. hydrophobic to hydrophilic by introducing $-\text{CH}_3$ or $-\text{COOH}$ end groups, respectively [20]. This modification is especially important for studying supported biomolecules or nanoparticles on top of the SAM, since the adhesion and interaction can be controlled [60, 61].

A wide range of main chains can be employed including aliphatic or aromatic species, however nowadays, the most important and studied SAMs are alkanethiols ($\text{CH}_3\text{CH}_{n-1}\text{SH}$) [62]. These alkanethiol SAMs are easy to prepare from the gas phase or solution and show a high air stability [20]. Further, alkanethiols show a high degree of ordering which can be attributed to weak vdW forces between the alkane chains [61].

Prominent candidates for forming SAMs are thiols on a gold surface due to their rather simple preparation from organic solvents with different terminal groups [63]. For the preparation of thiolate SAMs, two different headgroups can be used, thiols (SH) or thiocyanates (SCN). The main difference between those functional groups involves the mechanistic details of the assembly process. For thiols, the proposed process consists of two reaction steps where the thiol is first physisorbed on the surface followed by a chemisorption in which the hydrogen mercaptan is transferred into a thiolate bond [20]:



For the thiocyanate, additional steps must occur including the etching of Au and complexation which is indicated in eq. 4 and 5 [64]:



Major advantages of using SCN instead of SH are that SCN is more stable with regard to oxidation and does not polymerize in solution [65]. However, one disadvantage is, that SCN molecules must be purified using e.g. high-performance liquid chromatography (HPLC) to remove impurities (thiols or dithiols) prior to use [66]. The quality of the obtained SAMs by using the

two different head groups (SH and SCN) are structurally identical and of the same structural quality [66]. However, the level of impurities in the thiocyanate solution seems to influence the density of Au vacancy islands in the SAM. It was shown by Shen et al. [66] that these impurities inhibit the dissociative desorption of $[Au(CN)_2]^-$ (in comparison to thiols which can easily displace contaminants [67]). The purification of the thiocyanates molecules is mandatory in order to achieve the same quality as for the thiol molecules and thus, makes the use of SCN in the self-assembly process more challenging.

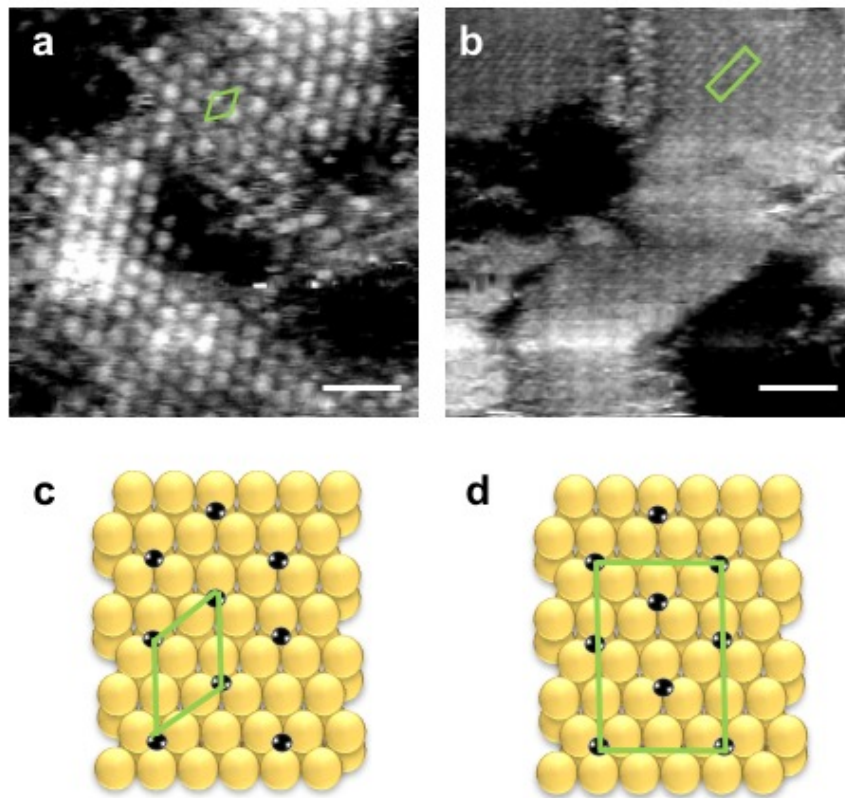


Figure 5: STM images of N-dodecyl thiocyanate on Au(111) (15 mM ethanol, 60 °C, 12h). a) $(\sqrt{3}x\sqrt{3})R30$ structure, b) $c(4x2)$ superlattice structure with the packing structures of a) and b) shown in c) and d) respectively, $I_t = 15$ pA, $U_t = 0.8$ V, scale bars 2 nm.

Self-assembly of thiols or thiocyanates on gold is easy to perform in liquid environments. For the SAM formation, in general, submicromolar concentrations are prepared in organic solvents with absorption times on the substrate ranging from 2 - 24 h (depending on the chain length - longer chains need longer absorption times) [20]. The formation yields long-range ordered patterns with different packing domains, $(\sqrt{3}x\sqrt{3})R30$ and $c(4x2)$ (the different packing domains are shown in Fig. 5 using dodecyl thiocyanate). The first one exhibits a hexagonal symmetry with a nearest neighbor distance of 0.5 nm and a surface coverage of $\theta = \frac{1}{3}$. The latter one exhibits an orthorhombic symmetry and can be described as the superlattice of the $(\sqrt{3}x\sqrt{3})R30$ structure.

Both symmetries can be observed during the absorption process of SCN and SH molecules. However, the origin and the amount of $(\sqrt{3}x\sqrt{3})R30$ to $c(4x2)$ domains is yet controversial [62]. Regarding these long-range ordered patterns, different characteristic features (also referred to as molecular defects) can be linked to the thiol absorption process. Typical defects which occur during the self-assembly process include e.g. missing rows of molecules, Au vacancy islands, pinholes or domain boundaries [20]. In these regions, the molecules have a certain degree of disorder.

The molecular defects can be influenced by the preparation conditions during the self-assembly formation. An example is shown in Fig. 6. Here, the self-assembly process is studied for an alkane chain with a SCN head group under different preparation conditions.

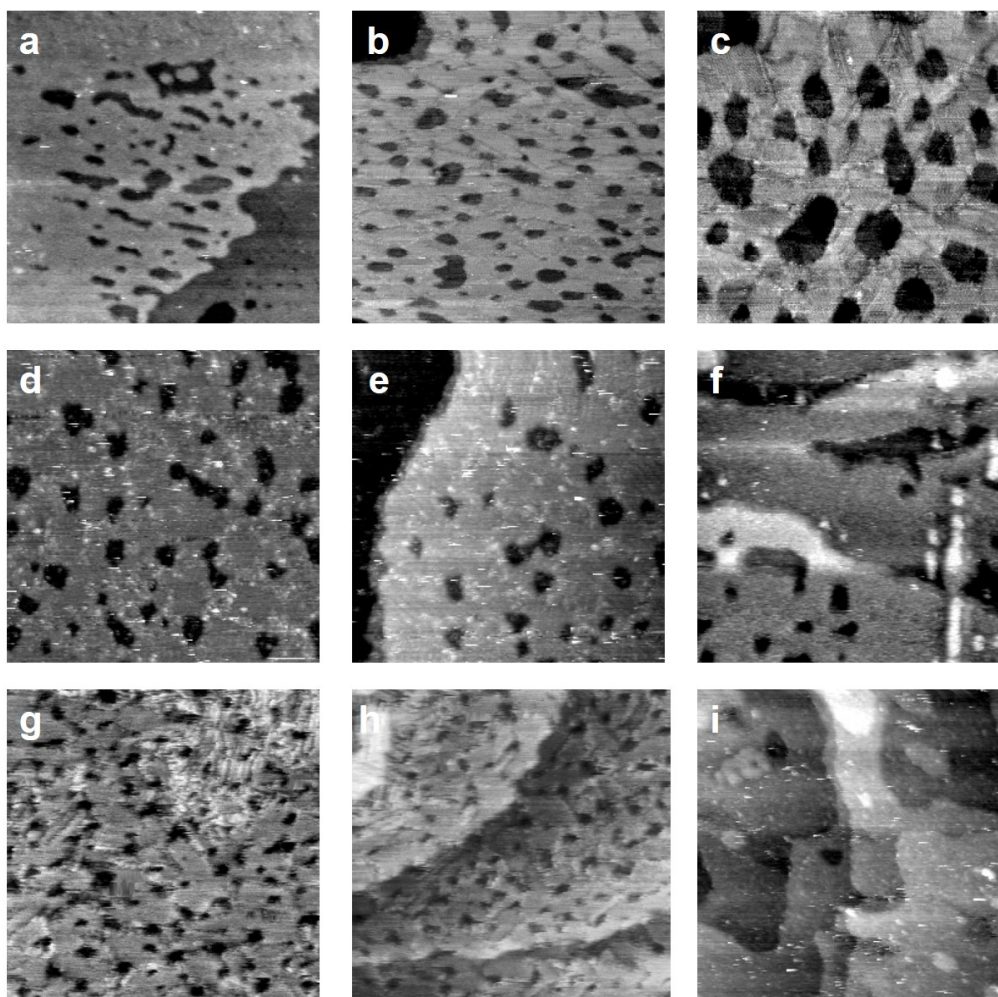


Figure 6: Representative STM images (100x100) nm of N-dodecyl thiocyanate (purified) under different preparation conditions. a) 15 mM, ethanol, RT, 12h, b) 15 mM ethanol, 60 °C, 12h, c) 15 mM ethanol, 60 °C, 72h, d) 5 mM ethanol, 60 °C, 12h, e) 15 mM ethanol, 75 °C, 60h, f) 5 mM ethanol, 60 °C, 72h, g) 1 mM ethanol, 60 °C, 12h, h) 15 mM isopropanol, 60 °C, 12h, i) 5 mM DMSO, 60 °C, 12h, $I_t = 15$ pA, $U_t = 0.8$ V.

Under elevated temperatures (Fig. 6a), an extended structure can be grown which exhibits large Au vacancy islands. However, under these preparation conditions, no distinct symmetry could be resolved. By increasing the absorption temperature for the self-assembly process (Fig. 6b), Au vacancy islands decrease in size and the $(\sqrt{3}x\sqrt{3})R30$ as well as the $c(4x2)$ lattice structure becomes visible. By increasing the absorption time (Fig. 6c), the Au vacancy islands size increases while maintaining the different packing domains. For obtaining small Au vacancy islands, the concentration must be decreased (Fig. 6g) or the solvent polarity must be changed to a slightly non-polar solvent (Fig. 6h).

According to Fig. 6 it can be seen, that the self-assembly process strongly depends on the preparation conditions. These conditions determine the SAM quality. For experiments including SAMs, one must decide which features (small or bigger Au vacancy islands; high level of ordering and symmetry) are essential for the experiments.

2.1.3 Supported Particles

The preparation of stable particles on various support materials is mandatory for electrochemical applications e.g. water splitting or hydrogen combustion. The most studied NP material is platinum due to its high catalytic activity in catalyzing the important hydrogen oxidation and evolution reaction (HOR/HER) [29, 30]. Since only small amounts of platinum are required to catalyze this HOR/HER, there is a great interest of studying submonolayer particle coverages [29, 30]. However, during operation in e.g. a hydrogen fuel cell, a loss of electrochemical active surface area (ECSA) is observed which could be attributed to a change in the morphology of the supported particles. Thus, several attempts have been made in the past to study the prevalent mechanisms occurring at the particle-support interface regarding the detachment of particles (depending on the particle size) [31, 32], particle dissolution [33, 34] and the influence of the support material [35, 68]. Fig. 7 summarizes the observed degradation mechanisms of platinum NPs supported on a carbon disk [18]. It can be seen, that different degradation mechanisms can occur at the interface which can be related to the loss in ECSA (as observed in electrochemical measurements). In the following, the different degradation mechanisms will be explained in more detail.

One of the processes which can occur on a carbon support is **platinum dissolution**. This process seems to be the dominant process especially for small particles (approx. 1.9 nm particle diameter) on carbon black [69]. Since with decreasing size of the particles the surface energy increases, the particles dissolve at already lower potentials as in the bulk [70]. If single particles

are redeposited out of the electrolyte on top of particles at the carbon support, these particles can grow to larger ones. This process is associated with **3D Ostwald ripening**. Another process which could explain the growth of particles is based on **agglomeration**. Due to weak particle-support interactions, the particles can migrate on the carbon support. This weak support interaction can further be lowered by a local corrosion of the carbon support which enables particle movement. This corrosion is also strongly believed to be the reason for **particle detachment**. The **corrosion of the carbon support** occurs especially under the harsh operation conditions in fuel cells: high water content, low pH, high temperatures and high potentials [71].

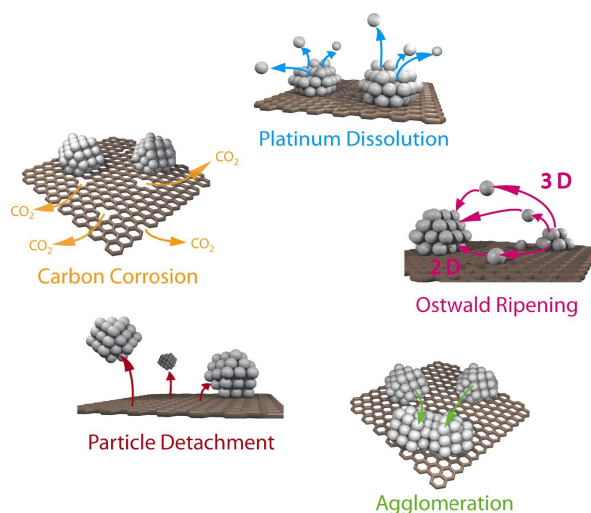


Figure 7: Different degradation mechanisms for supported platinum nanoparticles on a carbon support. Reprinted with permission from J. C. Meier, C. Galeano, I. Katsounaros, J. Witte, H. J. Bongard, A. A. Topalov, C. Baldizzone, S. Mezzavilla, F. Schüth, K. J. J. Mayrhofer, Beilstein J. Nanotechnol. 2014, 5, 44-67, Copyright © 2014 Meier et al.; Beilstein-Institut.

It can be seen, that carbon is not the ideal support since it can induce particle detachment and agglomeration. In addition, carbon can oxidize at high potentials (>1.0 V vs. RHE) and form surface oxides. Here, gold supports have attracted attention in the field of electrocatalysis. Gold single crystals exhibit a well-defined and extended surface structure which is highly reproducible. Au single crystals are an accurate reference system [35] due to their inertness and inactivity in the range of operation (0.05 V - 1.0 V vs. RHE). In addition, gold surfaces bear the potential of surface modification using SAMs.

SAMs (as described in the previous section 2.1.2) are prime candidates to decouple the properties of the particle and the support and hence, provide a route to study the metal-SAM-junction. They can improve the resolution in electrochemical measurements because they can act as spacer or blocking layer and thus, reduce the capacitance of the system. However, most of the NP materials (Au [72], Cu, Ag, Pt [58]) are not stable on top of SAMs (the SAMs are functionalized with a $-\text{CH}_3$ end group). They either degrade or penetrate through the SAM by forming 2D patches at the Au-SAM interface [73, 74]. Several attempts have been made in order to stabilize NPs on the support including, ligand-protected NPs, crosslinking of the end groups [61] as well as decrease the absorption temperature [75].

In this thesis, the stability of platinum NPs is investigated on a bare as well as on a alkanethiol covered Au surface. A manuscript is presented in Appendix B with the title: 'Mechanistic details on the flattening mechanisms of supported platinum nanoparticles on gold and thiol-terminated self-assembled monolayers'. Here it is observed, that the particles undergo a flattening process on both surfaces - on the bare gold as well as on the self-assembled monolayer covered gold surface. It was of special interest to study the mechanistic details which are responsible for the morphology change of the nanoparticle shape at the interface. The obtained electrochemical experiments are related to STM results which reveal the formation of a platinum monolayer on gold which is also measured in an enhanced HER/HOR activity. If a self-assembled monolayer is employed, it was found that the particles penetrate through the SAM and form a monolayer which is sandwiched between the thiol molecules and the gold support. Different degradation rates could be estimated based on CV, STM as well as on kinetic Monte Carlo simulations.

2.2 Scanning Tunneling Microscopy

2.2.1 Background on Scanning Tunneling Microscopy

STM is a surface sensitive technique which allows imaging of surfaces down to the atomic level. It was first developed by Binnig and Rohrer at IBM Zürich in 1982 [76, 77, 78]. In 1986, they received the Nobel Prize in Physics for their outstanding invention. A schematic overview of a STM setup with the basic working principle is shown in Fig. 8.

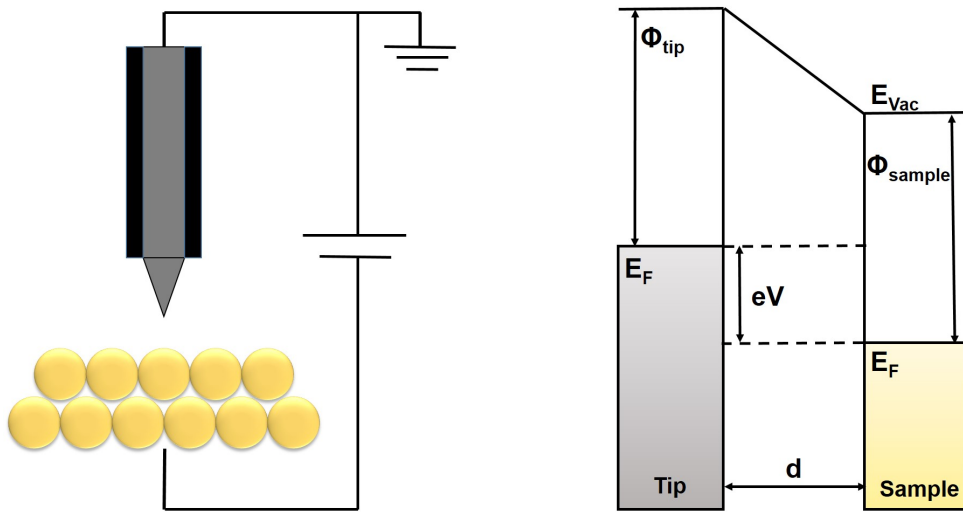


Figure 8: Left: schematic of the STM principle. Right: energy level diagram for a positively biased sample compared to the tip allowing electrons to tunnel from the tip to the sample.

In general, a sharp metal tip usually made of W or Pt/Ir [79, 80, 81] is brought in close proximity to a conducting surface and a voltage is applied between the tip and the sample. The electrons can only pass the vacuum/air barrier by tunneling either from the tip to the sample or vice versa depending on the sign of the applied bias voltage. If the tip is moved in the normal direction of the sample plane, the change in the tunneling probability can be mapped corresponding to the density of states (DOS) of the sample or the tip. A height dependency originates from the electron density probability which decays exponentially with increasing distance caused by a weakened overlap of the sample and tip orbitals. The tip is moved line-by-line over the surface with a scanner piezo based on the piezoelectric effect. Here, a voltage is applied to segments of the piezo which causes an electric polarization and hence, either a deflection in the z- or xy-direction.

The STM can be operated either in constant current or constant height mode. In constant current mode, the tip-sample distance is regulated by a feedback circuit to a given setpoint. By scanning the surface line-by-line and recording the z-position of the tip, a topography image can

be generated. In constant height mode, the tip is held at a certain distance and the change in the tunneling current is recorded. The latter mode is only used, if the surface is very flat preventing the tip from crashing due to non-uniformities of the surface.

STM measurements are based on quantum tunneling enabling electrons to pass an energy barrier with a finite height between tip and surface. In classical physics, an electron can not overcome a barrier if its energy is lower than the potential within the barrier. However, from a quantum mechanics point of view, there is a certain probability that electrons can overcome this barrier. The electrons can hereby be described by a wave function $\psi(r)$. The Schrödinger equation can be solved by the wave function yielding:

$$\psi(z) \propto e^{\pm ikz} \quad (6)$$

with $\kappa = \sqrt{\frac{2m_e E}{\hbar}}$. An electron entering a barrier with a finite height and width will have an oscillating wave function which decays exponentially within the barrier which is approximately proportional to $|\psi(z)|^2$:

$$|\psi(z)|^2 = |\psi(0)|^2 e^{-2\kappa z} \quad (7)$$

with $\kappa = \sqrt{\frac{2m_e \Phi}{\hbar}}$. Hence, there is a certain probability that the electron can be found behind the barrier. This probability is proportional to the absolute square of the wave function behind the barrier $|\psi(d)|^2$. A transmission coefficient can be expressed as:

$$T = \frac{|\psi(d)|^2}{|\psi(0)|^2} \approx e^{-2\kappa d} \quad (8)$$

This transmission coefficient is proportional to the tunneling current in STM experiments. In a STM tunneling junction, the barrier height is in the order of the work function of the metal Φ and the barrier width reflects the tip-sample distance d . The tunneling current I_T through such a barrier is then given by:

$$I_T \propto I_0 \frac{V}{d} e^{-\kappa \sqrt{\Phi} d} \quad (9)$$

with V the applied potential, I_0 the current, $\kappa = \left[\left(\frac{4\pi}{\hbar} \right) 2m \right]^{\frac{1}{2}}$ and m the free-electron mass. According to this equation it can be seen, that if the distance between the tip and the sample is changed by 1 Å, the tunneling current changes by an order of magnitude.

In addition to surface topography studies obtained by STM, scanning tunneling spectroscopy (STS) experiments can be performed to obtain spectroscopic information as a function of electron energy. In STS experiments, the tip is placed over the sample and the tunneling current is recorded by varying the applied bias voltage with the feedback circuit switched off. This generates a current-voltage (I-V) spectrum yielding information of the local density of states (LDOS) of the sample. The derivative, conductance dI/dV , can be used to gain additional information of the actual band structure and band gap. Such dI/dV spectra can be obtained by either numerical differentiation or by using a lock-in amplifier. The lock-in technique will be described in the next section 2.2.2.

2.2.2 Principles of Optically-Assisted STM

The effect of light on the tunneling current/junction can be studied indirectly by acquiring the tunneling current changes induced by light with single molecule absorption (SMA) detected by STM [82]. In SMA-STM experiments, many challenges have to be overcome prior reaching sub-nanometer resolution, including coupling light into the substrate while preventing heating effects. To avoid this heating effects of the junction, a prism is attached to the back of a sample allowing for a back illumination geometry in the Kretschmann configuration [83]. Here, a p-polarized laser is used undergoing TIR at the surface-vacuum interface while generating an evanescent field. The evanescent wave decays exponentially perpendicular to the surface with increasing distance. This evanescent wave can be used to excite supported nanostructures on top of a (semi-)transparent substrate. A schematic of the light coupling device with a prism in the Kretschmann configuration is shown in Fig. 9. This configuration minimizes tip heating effects at the tunneling junction and prevents thus tip crashes when switching on the light and leads to a stable average tip position during on/off cycles [82].

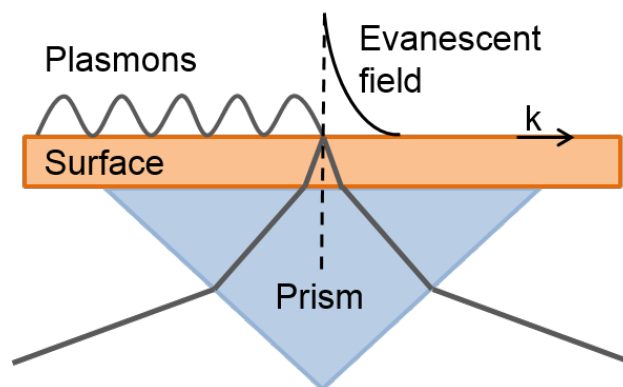


Figure 9: Schematic of the Kretschmann configuration used in SMA-STM studies.

By employing this setup, different effects of light on the tunneling current can be studied under intensity modulated light illumination. In order to understand these phenomena at the tunneling junction, first, a closer look is taken at the inverse process.

It is well known, that photon emission can occur from the tunneling junction by applying a high bias [84, 85]. Gimzewski *et al.* [85] reported resonance phenomena in photon emission spectra for polycrystalline silver films. Two distinct features are observed which are independent of the applied bias. They attributed this phenomena to resonant excitation and radiative decay of localized surface plasmon modes. They showed for the first time, that a STM can be used to investigate the inverse photoelectric effect stimulated by electron tunneling in a STM junction. Further, Berndt *et al.* [86] studied the light emission from a tunneling junction in more detail for metallic systems. They showed, that inelastic tunneling electrons can excite localized surface plasmons and the resulting emitted light appears to be red-shifted with respect to the high-voltage field emission regime. Besides investigating extended surfaces, Nilius *et al.* [87] studied photon emission for different sizes of Ag nanoparticles. The light emission stimulated by electron injection from the STM tip was assigned to a Mie-plasmon resonance of the particles. They showed, that the resonance position shifted to higher energies when the size of the nanoparticles is decreased.

When studying the direct effect of light on the tunneling current, either tip or surface phenomena can be observed. Since the STM tip can act as an antenna, field enhancement is a predominant effect which can induce tip plasmons when a metal surface (usually Ag or Au [82, 88]) is imaged, analogous to the enhanced Raman signal of molecules adsorbed on rough metal surfaces [89]. Savage *et al.* [90] showed, that a nanoscale plasmonic cavity can be formed by two Au-coated tips which support plasmonic resonances created via the strong coupling between localized plasmons on each tip. Besides the tip, also nanostructures can act as antenna resulting in an enhanced local electric field. Stamplecoskie *et al.* [91] reported an enhanced electronic transition when clusters are within close proximity of metal particles.

Surface phenomena include the excitation of surface plasmons. This excitation leads to an additional bias-independent electron flow between tip and the sample in a STM. This electron flow is directed into the sample and if the sample is biased positive, the tunneling current increases upon illumination [88]. Due to the non-linear characteristics of the tunneling junction [92], the surface plasmon field manifests itself as a rectified DC component [82]. The surface plasmon excitation can be transferred into a localized surface plasmon resonance (LSPR) of supported structures on a plasmonically active support. An increased tunneling current can be observed on

top of the excited nanostructures. This increased tunneling current can be explained by a higher LDOS of the structure under illumination which opens up further channels in which the electrons can tunnel or a reduced tunneling barrier caused by LSPR. Besides the coupling behavior, the propagation length of surface plasmons can be measured [93].

In this thesis, the coupling behavior of gold surface plasmons into a platinum cluster LSPR is investigated and presented in Appendix B: 'Plasmonic activation of 1 nm platinum clusters for photocatalysis'. Plasmonic excitation and electron transfer enhance the light-induced tunneling current on the clusters relative to their gold support. To investigate the improved catalytic activity, an oxidative decomposition reaction of a methylene blue film is performed. The platinum cluster catalytic activity under illumination exceeds the bare gold surface baseline activity by more than an order of magnitude per active area.

In addition to the presented phenomena, direct absorption can be studied using a STM. Direct absorption is demonstrated e.g for supported carbon nanotubes (CNT) or quantum dots (QD) on an ultrathin, transparent gold film [94, 95]. The excitation of the supported CNTs/QDs lead to a transition of electrons in occupied or unoccupied states of the supported structures depending on the bias polarity. For a positive sample bias, a tunneling current decrease is observed under illumination (which is the opposite effect when compared to surface plasmons as mentioned above). Since CNTs and QDs show a direct absorption, electrons are excited into higher states and hence, less tunneling electrons can tunnel into these states. By employing the SMA-STM technique, chiral junctions of CNTs can be imaged with nanometer spatial resolution under chopped monochromatic light illumination. Nienhaus *et al.* [94] showed, that the bandgap of a CNT with a semiconducting-metallic junction can be tuned into resonance with the excitation laser light by varying the electric field from the STM tip. They concluded, that the combination of laser and tip field Stark effect can tune the junction from strong semiconductor-metallic character to nearly equal optical properties for the two halves of the junction [94]. For supported QDs on a transparent gold film, electronic excitation leads to different angular momentum states depending on the sample bias which are imaged with SMA-STM [95]. For single dots, S- or P-like orbitals are observed, whereas adjacent pairs of QDs reveal orbital alignment which is an indication for electronic coupling between the dots.

In order to detect either the direct or indirect absorption, a sensitive detection technique of the tunneling current is mandatory to detect the modulation of the density of states upon absorption. A lock-in technique allows to measure the difference of the tunneling current on the chopped laser light. The lock-in technique is a phase-sensitive detection technique in which the input signal is

multiplied by a sinusoidal reference input signal and integrated over time. The output signal is then the product of the two waves at the difference ($\omega_r - \omega_L$) and sum ($\omega_r + \omega_L$) frequency.

$$V_{out} = V_{sig}V_L \sin(\omega_r t + \theta_{sig}) \sin(\omega_L t + \theta_{ref}) \quad (10)$$

$$V_{out} = \frac{1}{2}V_{sig}V_L \cos([\omega_r - \omega_L]t + \theta_{sig} - \theta_{ref}) - \frac{1}{2}V_{sig}V_L \cos([\omega_r + \omega_L]t + \theta_{sig} + \theta_{ref}) \quad (11)$$

If the signal passes a low pass filter, a DC signal which is proportional to the signal amplitude will be generated if the frequencies are $\omega_r = \omega_L$ according to:

$$V_{out} = \frac{1}{2}V_{sig}V_L \cos(\theta_{sig} - \theta_{ref}) \quad (12)$$

By using two channels X and Y which are shifted of $\vartheta = 90^\circ$, two signals can be generated representing the 'in-phase' (X) and 'quadrature' component.

$$X = V_{sig} \cos \vartheta \quad (13)$$

$$Y = V_{sig} \sin \vartheta \quad (14)$$

By appropriate adjustment of $(\vartheta_{sig} - \vartheta_{ref})$, the absorption signal can be maximized (X-channel), while the signal at 90° phase shift vanishes (Y-channel). Once this setting is optimized, the values ϑ_{sig} and ϑ_{ref} do not change.

2.2.3 Electrochemical STM

Initially, the invention of the STM allowed for measurements which take place at the solid-gas interface under vacuum conditions. However, many interesting phenomena occur at the solid-liquid interface, e.g. corrosion of metals [96], various redox and biological processes [97] including hydrogen generation for energy conversion [17]. Thus, four years after the invention of the STM [77], the first paper was published in which a STM was successfully employed in a liquid environment using oil and liquid nitrogen as electrolyte [98]. Afterwards, Sonnenfeld *et al.* [99] reported the first results obtaining atomic resolution of HOPG and gold substrates in a water-based electrolyte. This first generation of ECSTM were only based on a two-electrode setup which allowed the control of the tip and sample potential. In a further development, a three-electrode setup was developed which allowed to adjust the tip and electrode potentials independently [100, 101]. In this configuration, a potentiostat is used to control the potential

of the working electrode (WE) with respect to the reference electrode (RE) by adjusting the current at the counter electrode (CE).

Until then, many groups have reported *in-situ* ECSTM studies in various electrolytes e.g. in aqueous, organic or ionic liquid environments [102, 103, 104, 105]. A schematic overview of the ECSTM setup as used in our lab, with the peculiarity that the tip potential is at the ground potential, is shown in Fig. 10.

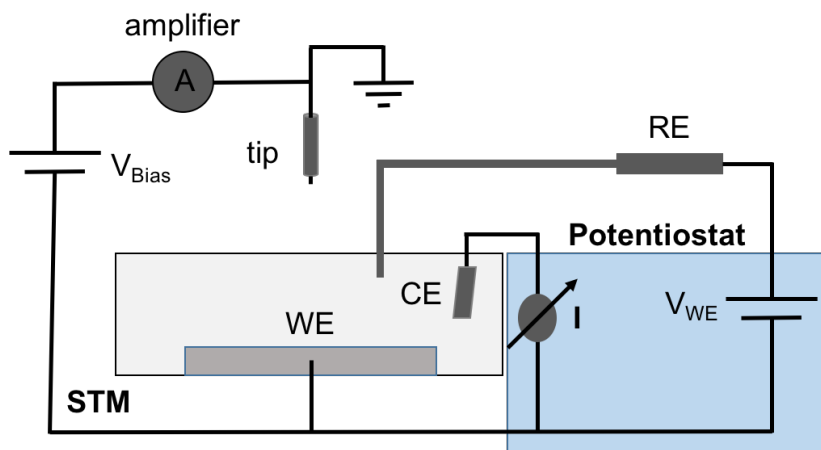


Figure 10: Schematic overview of an ECSTM setup.

In comparison to a conventional STM, two major elements are introduced: a suitable tip and a potentiostat which controls the electrochemical potentials. Whereas studies in UHV and air can be performed with a common STM tip, STM experiments in liquids are more challenging. The tip which is used in liquids has to be covered with a thin insulating layer due to redox processes and prevent and minimize faradaic currents at the tip shaft [106, 107] (except when operating in electrolytes with low relative permittivity).

Moreover, the tunneling process through an electrolyte can be influenced by adsorption of solvent molecules such as water at the tip and surface that shift the work function of the interacting surfaces and thereby, lower the tunneling barrier [108]. Furthermore, hydrogen and oxygen atoms stemming from water molecules can change the lateral modulation of the potential energy surface [109].

The ECSTM can mainly be operated in 2 modes:

- i) the surface is scanned before and after a potential sweep, also referred to as cyclic voltammetry (CV), explained in detail in section 2.3.1, or
- ii) the WE potential can be stepwise increased while scanning the surface at a fixed bias potential.

An example for the two operation modes is shown in Fig. 11. In Fig. 11a, a dodecanethiol SAM on a gold surface is imaged in 0.1 M HClO₄ with an insulated tungsten tip. A CV, in the potential range of 0.0 V - 0.6 V vs. RHE, is recorded while the tip is in tunneling range. After the CV, the surface is imaged again. In Fig. 11b, a dodecanethiol SAM is used and scanned in the first image at a WE potential of 0.0 V vs. RHE. After completing the image, the WE potential is increased to 0.1 V vs. RHE and the surface is imaged in STM mode again. The fourth image was therefore imaged at a total WE potential of 0.3 V vs. RHE.

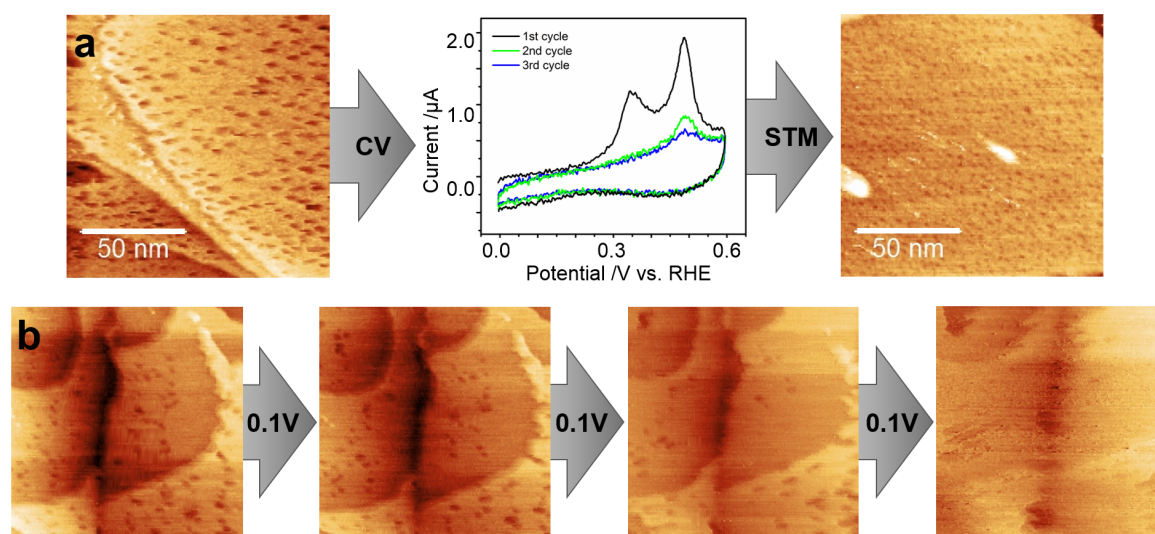


Figure 11: Scanning principle of an ECSTM. a) STM image taken before and after a CV. b) stepwise increase of the electrochemical potential while scanning at a fixed bias potential. The images are recorded at a WE potential of 0.0 V, 0.1 V, 0.2 V and 0.3 V. All potentials are measured vs. RHE.

ECSTM has limitations regarding the dissolution of the insulating layer of the tip leading to drift and instabilities due to higher effective electrical resistance and thus, higher tunneling current values [110]. In addition, adsorption of molecules at the tip apex, e.g. thiols, can prevent recording high-resolution images.

Further, the potential of ECSTM is, that the tip (after retraction) can also be used as sensor to detect local reactivities of supported structures e.g. nanoparticles [111].

2.3 Electrochemical Methods

2.3.1 Cyclic Voltammetry

Cyclic voltammetry is a potential sweep technique to measure electrochemical properties and redox potentials of surfaces. Two types of currents can be measured: Faradaic (reduction and oxidation of chemical species) and nonfaradaic (capacitive charging) currents. In CV experiments, the potential is ramped linearly over time until it reaches the first maximum vertex potential E_1 . Afterwards, the potential is reversed to the initial minimum potential E_2 (Fig. 12). A cyclic voltammogram is generated by plotting the applied potential versus the measured current.

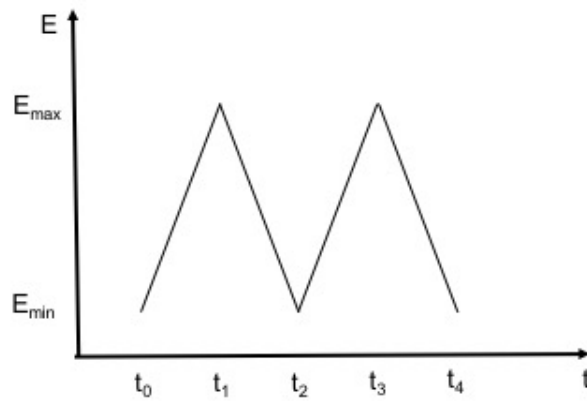


Figure 12: Cyclic voltammetry potential waveform. Adapted from Ref. [112].

The change in the potential over time can be described by the following equation (where v is the scan rate):

$$E(t) = E \pm vt \quad (15)$$

In a more broader context, by applying a potential at the substrate, ions are adsorbed onto the electrode surface forming a molecular dielectric (inner Helmholtz plane). In addition, (solvated) ions are creating the second layer attracted to the first layer via Coulomb forces or electrical screening effects (outer Helmholtz plane). The thickness d of these layers can be described by the Helmholtz model according to:

$$\frac{C}{A} = \frac{\varepsilon\varepsilon_0}{d} \quad (16)$$

where C is the capacitance [F], A the area [m^2], ε the dielectric constant of the material [F/m], ε_0 the permittivity [C/V m] and d the thickness [m]. The capacitance cannot be neglected when

investigating supported nanoparticle systems: low generated particle currents get superimposed by the capacitance of the support (offset currents). To overcome this limitation, the capacitance can be reduced e.g. by using SAMs that act as surface blocking layer, as described in 2.1.2. Since the distance d in eq. 16 increases by the SAM, the capacitance of the system decreases.

To calculate structural parameters e.g. the ECSA and the roughness factor r_f (which will be explained later in the text), the starting point is the total charge of ad- and desorption. In aqueous electrolytes, the total charge of adsorption Q_a or desorption Q_d of protons is used as standard reaction. The protons are adsorbed and reduced in a one-electron process. These charges reflect the number of electrochemically accessible surface sites which is also referred to the real active surface area of the electrode. The charges can be determined from faradaic currents for the hydrogen underpotential deposition (H_{upd}), ranging from $E_2 = 0.05$ V to $E_1 = 0.35$ V with respect to a reversible hydrogen electrode (RHE):

$$Q_{a,d} = \frac{1}{v} \int_{E_2}^{E_1} IdE \quad (17)$$

It is based on the assumption that a monolayer of hydrogen is adsorbed above the equilibrium potential in which one surface atom adsorbs one hydrogen atom. The roughness factor r_f [dimensionless] is the ratio of the real active surface area and the geometric surface area [113, 114]:

$$r_f = \frac{Q_{a,d}}{\rho_Q \pi r^2} \quad (18)$$

where r is the radius of the electrode [cm] and ρ_Q the charge per surface site [C/cm^2]: $\rho_Q = \rho_{at} \cdot e$. For planar platinum surfaces, an experimentally determined value is $210 \mu\text{C}/\text{cm}^2$ [115]. Typically, single crystals exhibit low roughness factors while especially supported particles show an increased roughness [116].

If the material loading m [g/m^2] on the electrode is known, the ECSA [m^2/g] can be calculated:

$$ECSA = \frac{r_f}{m} \quad (19)$$

If the material loading m is unknown, a value can be estimated using TEM. According to TEM micrographs, an average diameter of the supported particles can be estimated and converted into an $ECSA_{TEM}$ [29]: $ECSA_{TEM} = \frac{6}{\rho d}$, with ρ the density of the material and d , the average particle diameter. In a good approximation, the two values for the ECSA yield similar values.

The ECSA is an important figure of merit for the intrinsic activity. In addition, influences occurring at the interface can be identified which limit the electrochemical active surface area [117].

2.3.2 Rotating Disk Electrode

RDE experiments are performed to study the electrode kinetics of reactions. The setup of a RDE is shown in Fig. 13 and consists of three electrodes (WE, CE and RE) which are controlled by a potentiostat, in analogy to the previously described ECSTM setup (section 2.2.3). The WE is now mounted on a rotator allowing for a defined convection. The mass transport in front of the sample surface (that points downwards into the electrolyte) is the sum of convection and diffusion.

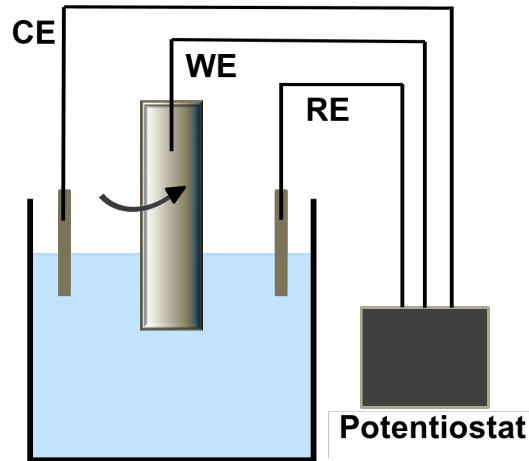


Figure 13: Setup of a RDE with potentiostat and electrodes.

If the kinetics of the reaction are faster than the mass transfer, the overall reaction rate is limited by diffusion. This diffusion limited current i_d , also known as Levich current I_L , can be expressed by [118]:

$$i_d = 0.620 n F A D^{\frac{2}{3}} \omega^{\frac{1}{2}} \nu^{-\frac{1}{6}} c \quad (20)$$

with n the number of transferred electrons [mol], F the Faraday constant [C/mol], A the electrode area [cm²], D the diffusion coefficient [cm²/s], ω the angular rotation rate [rad/s], ν the kinematic viscosity [cm²/s] and c the analyte concentration [mol/cm³]. In order to extract the kinetic

current i_k of a reaction from the measured total current at the electrode, one can calculate:

$$\frac{1}{i} = \frac{1}{i_d} + \frac{1}{i_k} \quad (21)$$

The kinetic current density of a reaction, $j = \frac{i_k}{A}$, is given by the Butler-Volmer equation (equation 22) [119, 120]. The rate of an electrochemical reaction depends exponentially on the driving force of the reaction:

$$j = j_0 \left[\exp\left(\frac{\alpha_a n F}{RT} \eta\right) - \exp\left(-\frac{\alpha_c n F}{RT} \eta\right) \right] \quad (22)$$

where j_0 is the exchange current density [A/m²], α the charge transfer coefficient for the cathodic (*c*) and anodic (*a*) sweep [dimensionless], n the number of electrons [mol], F the Faraday constant [C/mol], R the universal gas constant [J/mol K], η the overpotential [V] and T the temperature [K]. For a single step reaction with symmetric electron transfer, α is 0.5. The exchange current density j_0 is the rate of reaction when the overpotential is zero. The overpotential is the higher potential which is required for a reaction than one would expect according to thermodynamics.

In general, two limiting cases of the Butler-Volmer can be distinguished:

- at high overpotentials $1 \ll \frac{\alpha n F}{RT} \eta$, the Butler-Volmer equation can be written in a semilogarithmic form yielding the Tafel equation:

$$\eta = a + b \cdot \log j \quad (23)$$

with two constants a and b , where b represents the Tafel slope $b = \frac{RT}{\alpha n F}$, whereas the value of a is usually 0.5 for a single step reaction (symmetric electron transfer). The intercept with the y-axis can be calculated by extrapolating the Tafel line to $\eta = 0$, yielding the logarithm of the exchange current density j_0 .

- at low overpotentials $1 \gg \frac{\alpha n F}{RT} \eta$, the equation can be linearized (by using an approximation: $e^x = 1 + x + \dots$) to:

$$j = j_0 \frac{F}{RT} \eta \quad (24)$$

The overpotential is positive at the anode and negative for the cathode for a galvanic cell ($i > 0$). The Butler-Volmer equation is used in order to extract the exchange current density, e.g. in the HOR/HER [29, 33].

3 Experimental Background

3.1 ECSTM Setup

3.1.1 STM-head and STM-base

The ECSTM used in this thesis was developed by M. Wilms [103] in the group of Prof. Wandelt at the University of Bonn. This beetle type setup is based on two major components, a STM-head and a STM-base (Fig. 14) which are placed in an aluminum cubus for isolation from external vibrations and for gas atmosphere control. For decoupling the cubus from long wave vibration frequencies, it is placed on a heavy granite plate and mounted with climbing ropes at the ceiling. It is controlled and operated by the XPMPPro software (Version 2.0.1.6) by RHK Technology (Schaefer Technologie GmbH).

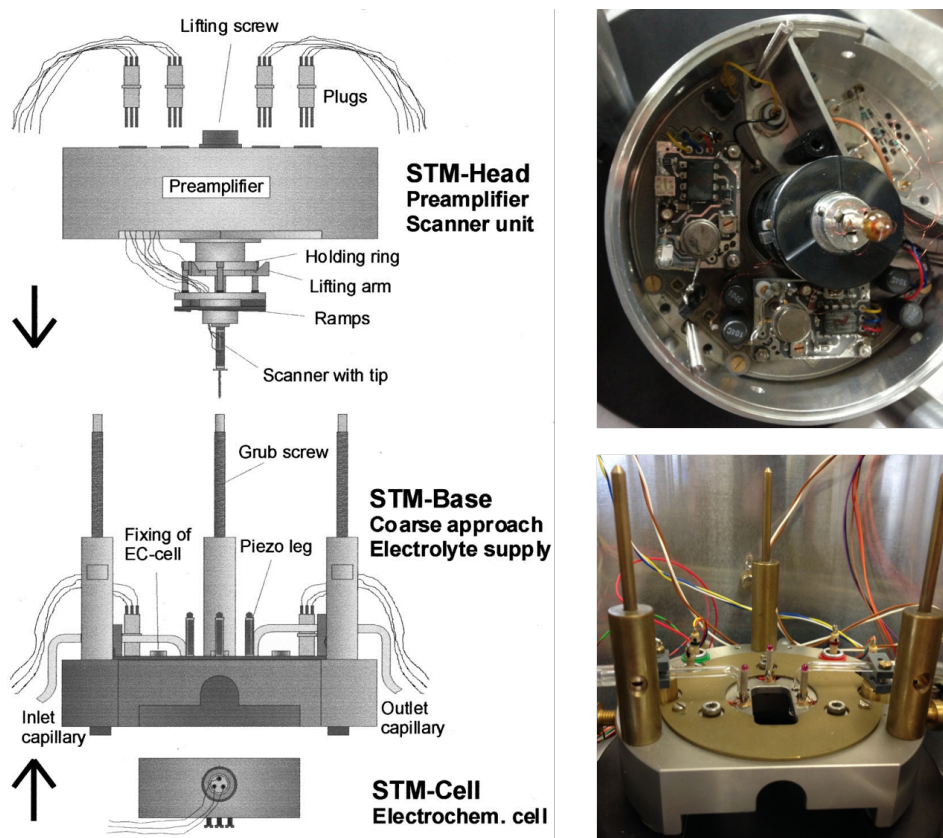


Figure 14: Left: schematic of the original STM setup. Reprinted with permission from M. Wilms, M. Kruft, G. Bermes, K. Wandelt, *Rev. Sci. Instrum.* 1999, 70, 3641-3650. Copyright © 1999 American Institute of Physics. Right top: image of the STM-head, right bottom: image of the STM-base.

The STM-head includes the RHK preamplifiers (IVP-200 and IVP-300) inside the housing as well as the scanner unit. The scanner unit consists of a holding ring, lifting arms, ramp and

the scanner piezo. Prior to mounting the STM tip in the scanner piezo, the length of the tip has to be adjusted precisely since the coarse approach can only drive a distance of 0.3 mm at maximum. The ramp for the coarse approach is divided into 3 slopy 120° segments to overcome this distance. For tip mounting, a special tip device is used to adjust the tip height with an accuracy of 0.1 mm (Fig. 15 left). The STM-head is then placed upside down on the STM-base columns and a lifting screw on the top unblocks the ramp that is thereby placed onto the 3 piezo base legs.

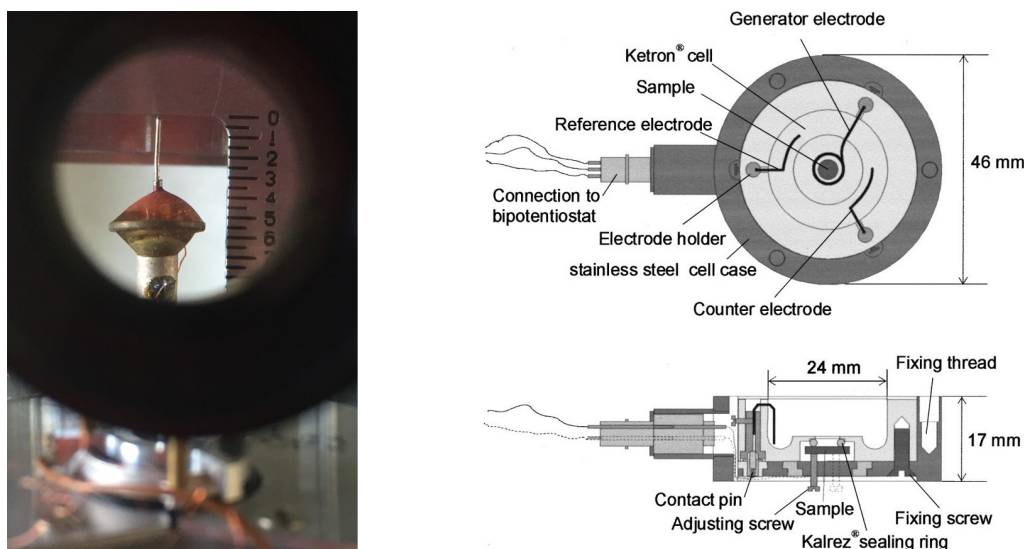


Figure 15: Left: tip adjusting device for STM tips. Right top: top view of the original electrochemical cell with cross section of the cell. Reprinted with permission from M. Wilms, M. Kruff, G. Bernes, K. Wandelt, *Rev. Sci. Instrum.* 1999, 70, 3641-3650. Copyright © 1999 American Institute of Physics.

3.1.2 Electrochemical cell

The sample is mounted inside the electrochemical cell (Fig. 15 right). For fixation, the sample is pressed against a Kalrez[®] ring and contacted with 3 fixing screws at the back. The cell is made of Ketron[®] which is highly resistant to all kinds of acids and has a low thermal expansion coefficient. For electrochemical measurements, a Pt wire was used as CE and fixed inside the cell. The cell can then be attached from below to the STM-base by fixing 3 screws.

3.1.3 Modification of the setup

Modifications of the original STM setup were made allowing for experiments in aqueous electrolytes as well as for tunable scanning conditions. The setup was modified and further developed for low-noise fast STM measurements in solution (Fig. 16 (1)). To this purpose, variable pream-

plifiers (FEMTO[®] LCA-S and DLPCA-200) were connected from outside the cubus. Screws are mounted at the connection which allow for two different grounding scenarios. If the screws are fixed, they connect the grounding of the amplifier with the cubus grounding (DPLCA-200) or separate the grounding of the preamplifier from the grounding of the cubus (LCA-S) when they are not fixed.

Additionally, an external RE was designed and connected via a Luggin capillary from outside the cubus to the cell (Fig. 16 (2)). With this improvement, a RHE can be employed for aqueous electrochemical experiments.

The RHE is a subtype of a standard hydrogen electrode (SHE) in which a hydrogen atmosphere is generated by electrolysis [112]. The potential correlates with the pH of the electrolyte:

$$E_0 = 0.000 - 0.059 \cdot pH \quad (25)$$

The advantage of using a RHE, instead of a SHE, is that the RHE can be used directly in the electrolyte without a salt bridge (as in the case for a SHE) and thus, contaminations by chloride or sulfate ions are prevented. In addition, the hydrogen ion concentration corresponds to that of the electrolyte solution enabling a stable potential with a changing pH value. For preparation of a RHE see 3.1.6.

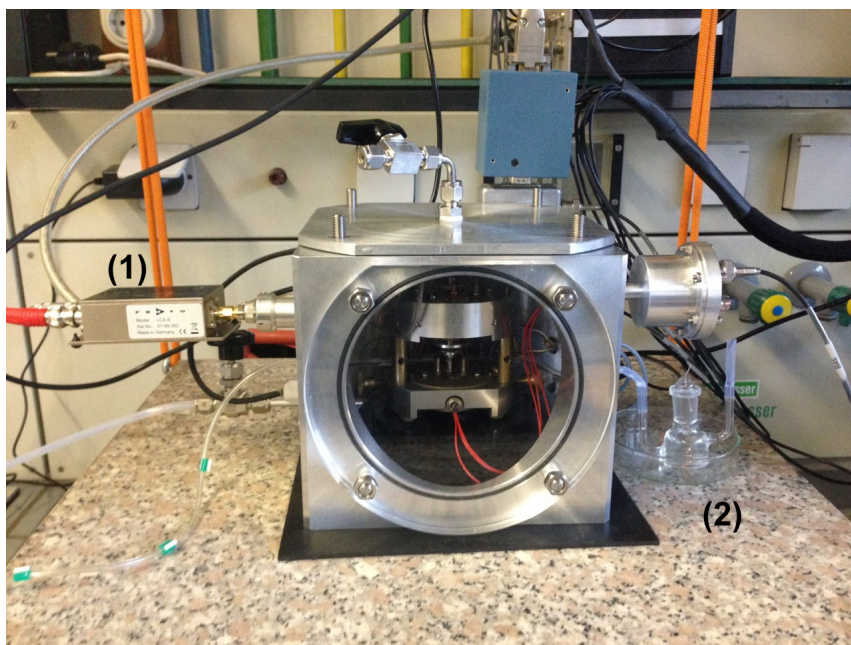


Figure 16: Modified STM setup with an external FEMTO[®] amplifier (1) and external RHE connected via a Luggin capillary to the electrochemical cell (2).

3.1.4 Tip Preparation

Sharp STM tips are required to achieve atomic resolution while scanning the surface. They can be prepared via electrochemical etching [121] or mechanical cutting. Two different tip materials are used in this work: tungsten and platinum/iridium. Tungsten tips are made via electrochemical DC etching while platinum/iridium tips are made via mechanically cutting or electrochemical AC etching.

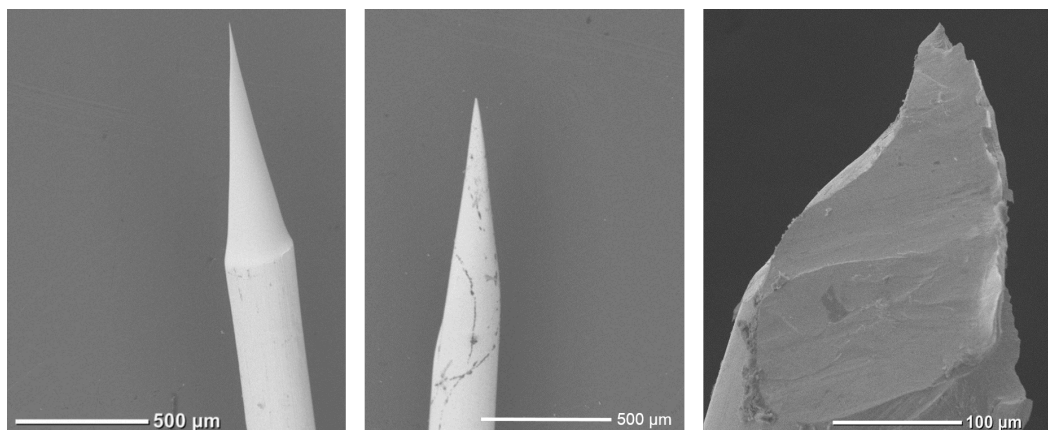


Figure 17: SEM images of STM tips taken at an acceleration voltage of 15 kV. Left: etched tungsten tip, middle: etched Pt/Ir wire and right: mechanically cut Pt/Ir tip.

Tungsten tips are electrochemically etched in a thin lamella of 3 M aqueous $NaOH$ suspended by a ring cathode made of gold. A 6 V DC voltage is applied until 80% of the wire is etched followed by a 3 V DC voltage for fine etching. After etching, the lower part is dropped off and caught by a holder. The tip is rinsed in deionized (DI) water and dried in a nitrogen stream.

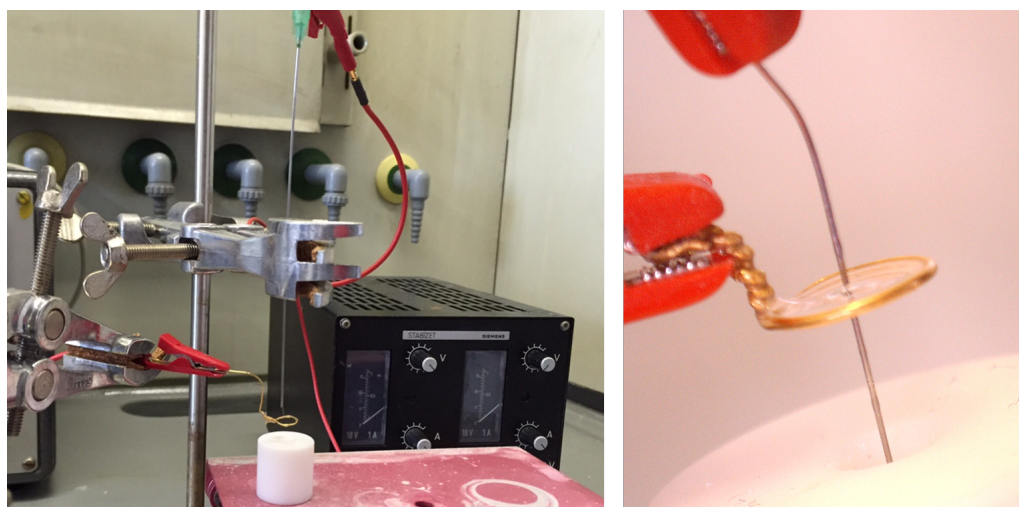


Figure 18: Left: setup for etching W tips, right: close-up of the W tip while etching in a lamella.

In this work, 2 different ways of making sharp Pt/Ir STM tips are used, either by mechanically cutting a Pt/Ir wire, or by etching, based on a recipe of Peter M. Albrecht (University of Illinois at Urbana-Champaign Center for Nanoscale Science and Technology (CNST), April 25, 2007). This procedure is divided into 2 steps which involves a coarse and fine etching. In a first step, a saturated solution of calcium chloride (75 g $CaCl_2$ and 100 mL with DI water) is mixed with DI water in a ratio of 1:2. A 1 cm long Pt/Ir wire is placed on a holder above the etching solution and lowered by approximately 1 mm into the solution. A graphite counter electrode is employed for electrochemically etching of the Pt/Ir wire by applying a voltage of 30 Vrms at 60 Hz. After 3-5 min a small teardrop-shaped piece of the wire is left. The etching solution is switched to the fine etching electrolyte containing a saturated $CaCl_2$ solution ($CaCl_2$ and DI water in the weight ratio 2:1). An AC voltage of 50 Hz is slightly increased until small bubbles are observed at the surface (typically voltages of 1 - 2 V). Afterwards, the tip is rinsed in DI water and dried in a nitrogen stream.

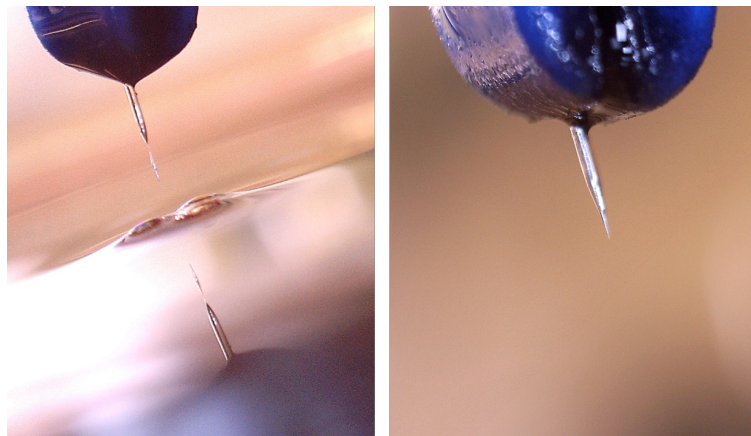


Figure 19: Left: Pt/Ir tip after the first stage of etching, right: final etched tip.

3.1.5 Tip coating

A polymer coating is used to isolate the tip to reduce capacitive currents flowing through the tip. To this purpose, the tip is pushed through hot glue resulting in an isolated shaft and uncovered tip apex. Since the glue is a thermoplast, it takes considerably time for hardening - up to 12h are advisable.



Figure 20: Etched tungsten tip coated with glue.

3.1.6 Electrochemical STM Measurements

For electrochemical experiments inside the STM cell, a LabView program $EC4^{TM}$ is used (Nordic electrochemistry). For CV experiments, the voltage is increased linearly over time until it reaches the 1st vertex potential. After that, the voltage direction is switched and linearly decreased until it reaches the 2nd vertex potential. All CVs are recorded in degassed 0.1 M $HClO_4$ starting with a positive scan direction at 0.5 mV while employing a Pt wire as CE. A RHE is used as RE and fixed outside the STM cubus via a Luggin capillary.

To prepare the RHE, a beaker is filled with 0.1 M $HClO_4$ and a Pt/Ir wire is used as CE. The RHE glass body (compare Fig. 21) is filled with the electrolyte and placed inside the beaker. A potential of 4 - 5 V is applied for 5 min. H_2 is generated at the negative potential (cathode) and thus, a gas atmosphere is created inside the vessel. The RHE can be used for approx. 12 h. Afterwards, a new RHE is prepared for the experiments.



Figure 21: RHE electrode.

3.1.7 Photoresponse Measurements

For photochemical measurements, a hole is drilled into the bottom part of the electrochemical cell allowing for back illumination of the sample. The setup can be used in two configurations: the light can be guided onto the back of the sample either via a fiber or directly via LED close-by. For the first configuration, a diode-pumped solid state (DPSS) green laser diode (Thorlabs) with a wavelength of 532 nm and 10 mW is coupled into a polarization-maintaining single mode fiber using two dielectric mirrors and an aspheric lens (Fig. 22).

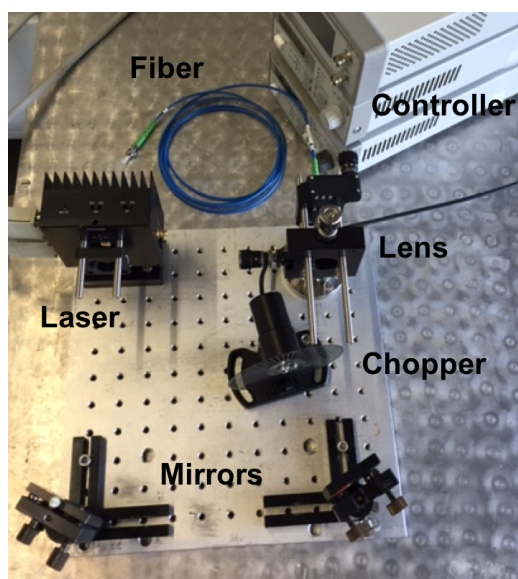


Figure 22: Optical setup for photochemical measurements.

The latter configuration with a LED placed directly under the sample, was used to measure the photoresponse of the bicomponent network on a transparent substrate (see section 4.2). For the photocurrent measurements, a 710 nm LED (30 mW/sr, 18°, Roithner Lasertechnik) and a 520 nm LED (9600 mCd, 30°, Nichia, Japan) were used. The light on-off cycles were measured independently with an Agilent STM (Agilent Technologies 5100) equipped with a logarithmic current amplifier.

In order to pick up the photovoltaic response from the molecular layer, an approach developed by the Whitesides group [50, 52] has been used. The tungsten wire, used in this case, is dipped into heated Ga ($\pm 75^\circ\text{C}$) or EGaIn (at room temperature) to form a droplet on the apex of the tip. The tip is then mounted on the scanner piezo and approached to the surface with a tunneling current setpoint of 2 nA and a bias of 0.1 V. STS spectra are recorded with a FEMTO preamplifier (LCA-S) and a forward sweep rate of 200 mV/s.

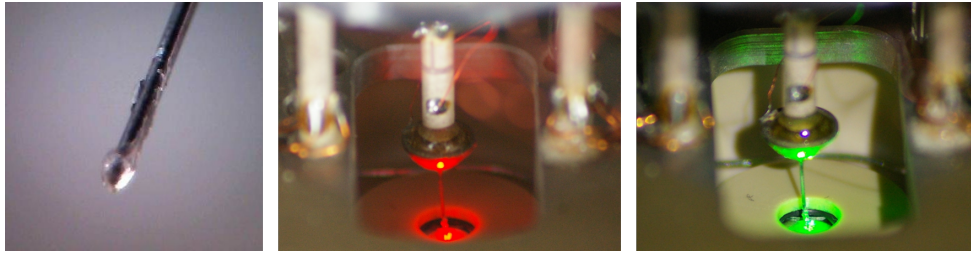


Figure 23: Left: tungsten tip with a gallium droplet, middle: STM under 710 nm and right: 520 nm illumination.

For an estimation of the contact area, 10 μL of a saturated Rhodamin B solution in ethanol were spin-coated three times onto a HOPG surface and mounted in the STM setup. The Ga (or EGaIn) drop was approached towards the surface again with a tunneling current of 2 nA and a voltage of 0.1 V. The droplet contacted the surface with the dye molecules by forming a physical contact. Afterwards, this droplet was retracted and imaged under a fluorescence microscope (Leica DMI 3000B, Wetzlar). The fluorescent parts belong to the dye molecules and hence, the upper limit of the contact area can be estimated by integrating of these parts.

Other methods (compare Fig. 24) were employed to estimate the contact area of the Ga droplet, but without success.

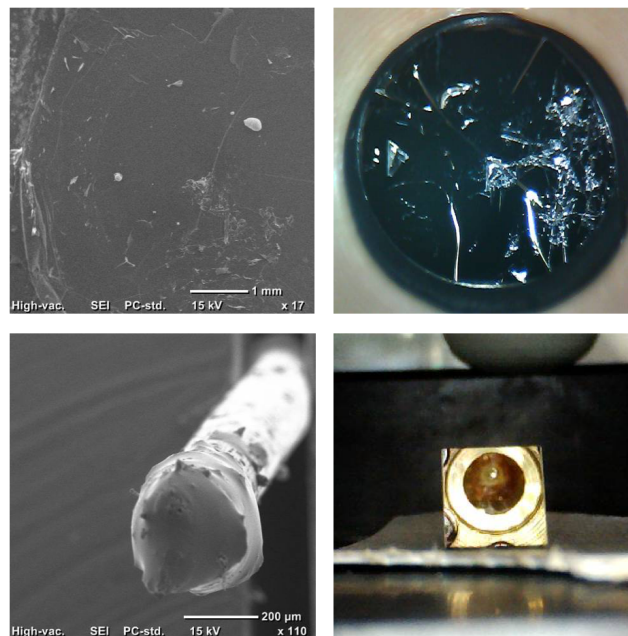


Figure 24: Different methods employed to determine the contact area of a Ga droplet. Top left: SEM image of a HOPG surface coated with methyl methacrylate (MMA). Top right: MMA coated HOPG surface under a USB-microscope. In both cases, the tip was approached to the surface and an imprint of the tip in the MMA was tried. Bottom left: SEM image of a tungsten tip with a Ga droplet which has contacted the surface. Bottom right: deflection mirror showing the surface and tip from underneath.

3.2 Optically-Assisted STM

SMA-STM experiments were performed at the University of Illinois at Urbana-Champaign, USA in the lab of Prof. Martin Gruebele. The setup is shown in the following Fig. 25 and described in detail in Ref. [94, 95].

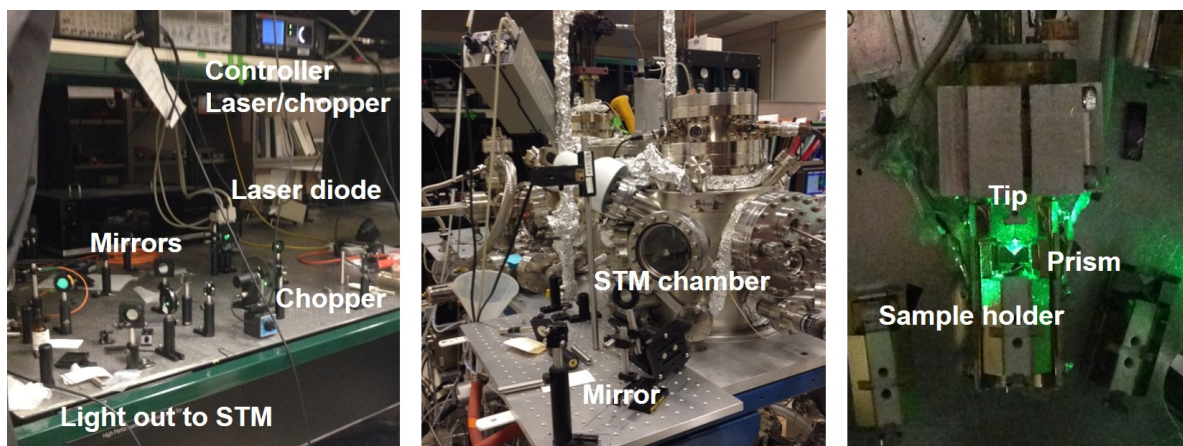


Figure 25: SMA-STM setup. Left: laser setup with mirrors and chopper. Middle: UHV STM chamber. Right: illuminated sample with prism.

A diode pumped solid state (DPSS) laser (Thorlabs) at 532 nm with an overall power of 10 mW is used for SMA-STM experiments. The laser light is chopped at a frequency of 2.2 kHz and guided by mirrors to the STM chamber. For coupling the laser light into the sample, a special geometry in the Kretschmann configuration [83] is employed allowing for back-illumination. A prism is attached at the bottom surface with a UHV compatible, transparent epoxy (Epotek 302-3M). For SMA-STM measurements, a lock-in amplifier (Stanford Research SR830) is used to detect the change in the tunneling current upon illumination with two channels (in- and out-of phase channel). The STM measurements in this thesis were performed with a tunneling current of 5 pA and a variable bias.

3.3 Rotating Disk Electrode Setup

A setup of Nordic Electrochemistry with the control software $EC4^{TM}$ was used for all RDE experiments. The setup consists of a potentiostat to control the electrode potentials and gas change system (Fig. 26). The gas change system has 6 inlets and 1 outlet which is connected to a flow controller followed by an optical control of the gas flow with a flow meter. The $EC4^{TM}$ program allows to control and select the gases and potentials independently. The program is the same as used for ECSTM experiments with addition of the rotation control parameters for

determination of kinetic parameters. Prior to the experiments, the glassware was cleaned in Caro's acid followed by several cleaning cycles in heated DI water. A RHE (as described in 3.1.6) was employed as RE. 0.1 M HClO₄ was used as standard electrolyte and degassed with Ar for 20 min prior to experiments. A platinum mesh served as CE and was connected via a frit to the electrochemical cell.

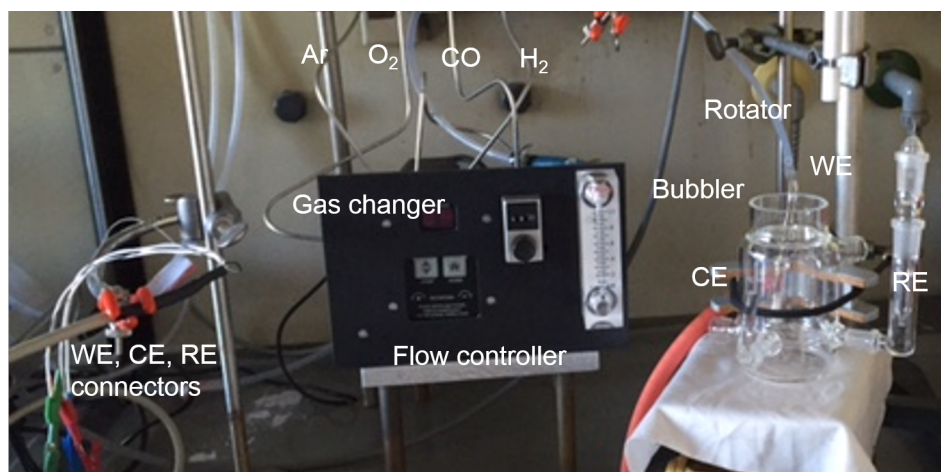


Figure 26: RDE setup with gas change system and flow controller.

HOR/HER were performed in a saturated hydrogen atmosphere in the electrolyte. Polarization curves were measured with different rotation speeds (400 rpm, 900 rpm, 1600 rpm and 2500 rpm) and a scan speed of 10 mV/s.

In order to determine the active area of supported particles on the surface, CO stripping experiments were performed. For the absorption of CO, the voltage is kept at 0.1 V for 5 min, while bubbling CO through the electrolyte at a rotation speed of 1600 rpm. Afterwards, Ar is bubbled through the electrolyte for 10 min in order to remove all remaining CO in the solution. A CO stripping CV is recorded afterwards, at a scan speed of 100 mV/s.

4 Self-Assembly on All-Carbon Substrates Towards Photovoltaics

Supramolecular chemistry can be understood as the chemistry of molecular assemblies and intermolecular bonds [23]. By definition, molecular self-assembly is the spontaneous organization of molecules into structurally well-defined and rather stable arrangements through a number of inter-molecular interactions [21, 22]. The formation of supramolecular well-ordered templates is driven by intermolecular and molecule-substrate interactions [47]. The self-assembly of artificial architectures is widely studied at solid-liquid and solid-vacuum interfaces [24, 25, 40, 43, 45, 47]. In the context of clusters and nanoparticles, two-dimensional frameworks fabricated with molecular precision are of particular interest because they can be used as host templates to trap guest molecules and promote the growth into the third dimension perpendicular to the surface [122]. Hydrogen bonded networks are one of the most studied interactions in supramolecular chemistry [123, 124, 125] due to the tunability of the interaction energies, depending on the hydrogen-bond donor and acceptor moieties [126]. Despite the fact, that single hydrogen bonds are rather weak, multiple hydrogen bonds can provide sufficient stability, while being sufficient weak to allow for the formation of well-ordered networks with precise bond geometries [127]. In particular, Au [41] and HOPG [128] are used as platform for the self-organization into 2D networks e.g. organic solar cells [129]. For technical applications, a suitable transparent - while atomically flat - platform is needed that allows for back illumination. Here, hydrogenated diamond provides an optimal test platform for sp^2 - sp^3 carbon-on-carbon optoelectronic technology [130].

To get more insight, the bicomponent supramolecular network formation is first studied using a diimide test molecule that can form triple hydrogen bonds with a melamine linker on HOPG and a graphene film in order to get informations about growth rate and layer formation (section 4.1). In a second part, this test molecule is then replaced by a dye molecule and the network formation is extended to transparent and flat surfaces (section 4.2).

4.1 Three-Dimensional Bicomponent Supramolecular Nanoporous Self-Assembly on a Hybrid All-Carbon Atomically Flat and Transparent Platform

The publication titled 'Three-dimensional bicomponent supramolecular nanoporous self-assembly on a hybrid all-carbon atomically flat and transparent platform' is presented in this section. The results published in this work pave the way towards ordered self-assembled nanostructures in three dimensions for applications in photovoltaics.

As previous results pointed out, the formation of supramolecular networks at ambient conditions is challenging since polymorphism and phase separation have to be avoided [25]. These phenomena prevent an ordered network formation on the surface, as well as hinder the growth in the third dimension [25]. In this study, a tetracarboxylic diimide moiety, namely 1,4,5,8-naphthalenetetracarboxylic diimide (NTCDI) together with a triamine cornerstone are employed to investigate the spatial composition and intermolecular interactions that lead to formation of bilayers. The spontaneous network formation of NTCDI and melamine is here imaged via STM on carbon-based substrates, namely HOPG, CVD-grown graphene on copper foil and graphene transferred on hydrogenated diamond (GHD) in order to get informations of growth rate and layer formation. The formed network is based on triple hydrogen bond recognition between the functional groups of the two molecules forming a long-range highly ordered pattern on all carbon supports. Depending on the polarity of the solvent, different lateral boundaries and 3D-vdW stacking can be found on HOPG. A single network growth rate is observed for this bilayer formation implying that the network expands as bilayer domain peripheries. Our results show that face-to-face stacking is preferred when using large aromatic molecules: Higher vdW interactions and reduced electrostatic interactions dominate.

All experimental measurements are performed together with Juan Li at the Physics Department E20 of TUM. Sarah Wiegold and Juan Li contributed equally to this work.

Three-Dimensional Bicomponent Supramolecular Nanoporous Self-Assembly on a Hybrid All-Carbon Atomically Flat and Transparent Platform

J. Li, S. Wieghold, M. A. Öner, P. Simon, M. V. Hauf, E. Margapoti, J. A. Garrido, F. Esch, C. A. Palma, J. V. Barth

Nano Letters, 2014, DOI: 10.1021/nl501452s

Permanent weblink:

<http://pubs.acs.org/doi/abs/10.1021/nl501452s>

Reprinted with permission from Nano Lett., 2014, 14(8), pp 4486-4492. Copyright © (2014) American Chemical Society.

Three-Dimensional Bicomponent Supramolecular Nanoporous Self-Assembly on a Hybrid All-Carbon Atomically Flat and Transparent Platform

Juan Li,^{†,¶,⊥} Sarah Wieghold,^{‡,¶,⊥} Murat Anil Öner,[†] Patrick Simon,^{§,†} Moritz V. Hauf,^{§,†} Emanuela Margapoti,^{§,†} Jose A. Garrido,^{§,†} Friedrich Esch,^{‡,¶} Carlos-Andres Palma,^{*,†,¶} and Johannes V. Barth^{*,†,¶}

[†]Physik-Department, Technische Universität München, James-Franck-Straße 1, 85748 Garching, Germany

[‡]Chemie-Department, Technische Universität München, Lichtenbergstraße 4, 85748 Garching, Germany

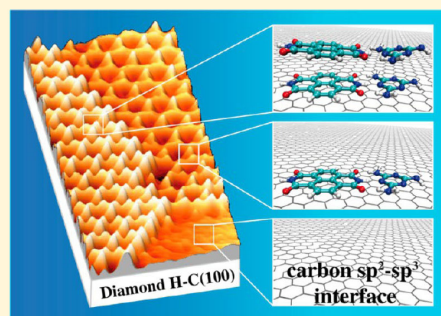
[§]Walter Schottky Institut, Technische Universität München, Am Coulombwall 4, 85748 Garching, Germany

[¶]Catalysis Research Center, Technische Universität München, Ernst-Otto-Fischer-Straße 1, 85748 Garching, Germany

Supporting Information

ABSTRACT: Molecular self-assembly is a versatile nanofabrication technique with atomic precision en route to molecule-based electronic components and devices. Here, we demonstrate a three-dimensional, bicomponent supramolecular network architecture on an all-carbon sp^2 – sp^3 transparent platform. The substrate consists of hydrogenated diamond decorated with a monolayer graphene sheet. The pertaining bilayer assembly of a melamine–naphthalenetetracarboxylic diimide supramolecular network exhibiting a nanoporous honeycomb structure is explored via scanning tunneling microscopy initially at the solution-highly oriented pyrolytic graphite interface. On both graphene-terminated copper and an atomically flat graphene/diamond hybrid substrate, an assembly protocol is demonstrated yielding similar supramolecular networks with long-range order. Our results suggest that hybrid platforms, (supramolecular) chemistry and thermodynamic growth protocols can be merged for in situ molecular device fabrication.

KEYWORDS: Self-assembly, supramolecular engineering, bilayer, solid–liquid interface, STM, graphene, diamond, supramolecular framework



Engineering of complex matter with molecules^{1,2} is regarded to as a major branch of chemistry for the future.^{3,4} It is indeed feasible that silicon technologies could be complemented or even superseded^{5,6} by more sophisticated atomically precise fabrication,⁷ which can be potentially steered⁸ from templated self-assembly.⁹ Following this technological shift, steps must be taken toward the practical integration and construction of molecular precise devices, from developing platforms fit for purpose to the establishment of specialized analytical self-assembly instrumentation. At the same time, chemistry and thermodynamics must be finely tuned to adapt to such experimental and technological protocols. Two-dimensionally (2D) extended, crystalline supramolecular^{10,11} or covalent^{7,12} multicomponent architectures represent ideal systems for testing the foundations of modular three-dimensional (3D) growth at well-defined interfaces.^{13–15} In fact, 3D metal–organic frameworks^{16,17} enjoy a widespread success because of their modularity, allowing control over macroscopic pore morphology and functionality. Fabrication protocols using technologically relevant platforms for such architectures are currently emerging.^{18–20} This bottom-up approach requires

either thermodynamic or kinetic control. The previous entails the formation of a precise number of stacked layers in a single solution or chemical mixture at equilibrium. Much like the forces directing 2D self-assembly, 2D-to-3D self-assembly must rely on covalent, metal–organic, hydrogen bonding, ionic or van der Waals (vdW) interactions. In the thermodynamic regime, it can be argued that the interlayer interactions should be enthalpically equal or lower than the intralayer interactions or the interactions between first layer and substrate. The kinetic approach relies on sequential exposure to different solutions, following the concept of layer-by-layer assembly.²¹ In this regime, the advantage is that interlayer interactions can be strong and independent of all other equilibrium processes. Hybrid thermodynamic–kinetic approaches may also be used, employing temperature or solvent annealing in single solutions or mixtures to fine-tune free energies of interaction.

Received: April 18, 2014

Revised: July 12, 2014

Published: August 1, 2014

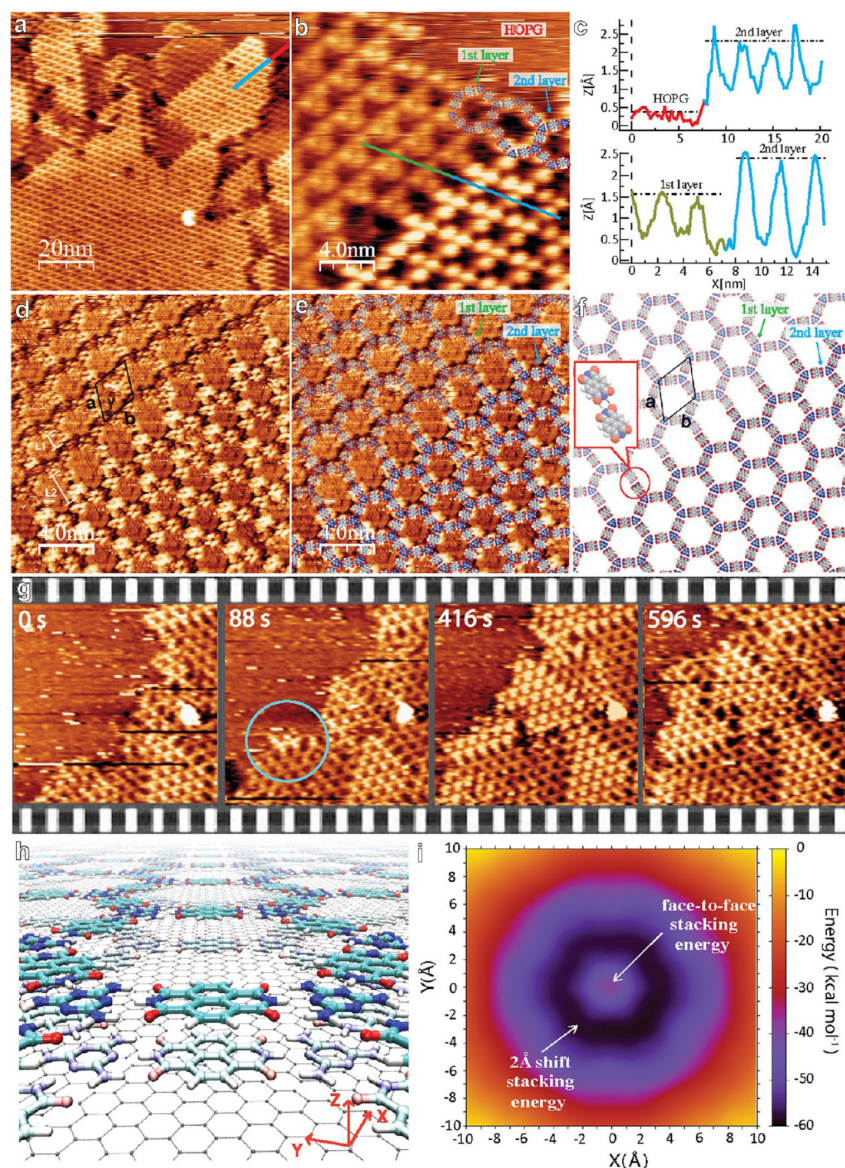


Figure 1. (a) Large-scale STM image of bilayer network of melamine–NTCDI on HOPG. (b) Close-up view of a domain boundary. The molecular models indicate the bicomponent supramolecular network motif as well as the NTCDI-pairing motif between first layers (transparent models). The second layer (solid models) overlaps one first layer domain. (c) Cross-sectional line profiles with different colors corresponding to the solid lines in (a) and (b). In the graphs, the height of substrate, first layer and second layer are depicted by red, green, and blue colors, respectively. (d) STM image with enhanced molecular resolution of the domain boundary. (e) STM image shown in (d) with the corresponding superimposed molecular models. (f) Bilayer molecular models reveal that the domain boundary formation is exclusively due to pairing of NTCDIs via two hydrogen bonds in the first layer. (g) Time lapse of STM images depicting the bilayer evolution. Bilayer growth from a monolayer edge is circled. (h) Perspective molecular rendering of face-to-face ($X,Y = 0,0$ in (i)) vdW stacking of a melamine–NTCDI bilayer on graphene. (i) Energy map of the X,Y translation of a melamine–NTCDI second layer relative to a fixed first layer using the MMFF force field. Tunneling parameters in all STM images at the solid–liquid interface: $I_t = 20$ pA, $V_t = 300$ mV. The concentration ratios of melamine and NTCDI are (a) $5 \mu\text{M}:8 \mu\text{M}$, (b) $5 \mu\text{M}:8 \mu\text{M}$, and (d) $2 \mu\text{M}:5 \mu\text{M}$ using TCB solutions with low DMSO content. Unit cell: $a = 2.8 \pm 0.1$ nm, $b = 2.8 \pm 0.1$ nm, $\gamma = 59 \pm 2^\circ$.

We have previously shown that vdW self-templating of bilayers using a pyromellitic tetracarboxylic diimide¹⁴ moiety on HOPG is a promising approach to achieve thermodynamic control over the growth in the third dimension. Here, we present scanning tunneling microscopy (STM) studies on the

3D self-templating of a bicomponent supramolecular network consisting of the 1,4,5,8-naphthalenetetracarboxylic diimide (NTCDI) organic semiconductor²² and the 1,3,5-triazine-2,4,6-triamine (melamine) cornerstone.²³ The 3D architecture represents a prototype modular multilayer supramolecular

framework due to the maintenance of reticularity and open pores. Importantly, these frameworks can be constructed on all-carbon transparent and atomically flat hybrid platforms, that is, commercial graphene (G) on copper foil and monolayer graphene transferred on a hydrogenated diamond H-C(100) surface. High-quality single-crystalline hydrogenated diamond is transparent, atomically flat, and conductive,²⁴ thus providing an ideal test bed of a novel platform for advanced self-assembly protocols. Our results present a significant step toward molecularly precise optoelectronic or photovoltaic device elements at hybrid interfaces with control in three dimensions by using self-assembled modular bicomponent supramolecular networks.

The assembly of the supramolecular bicomponent network²⁵ based on NTCDI bridging melamine is first performed on HOPG in equilibrium with different solutions, in order to investigate the propensity of 3D-vdW stacking similar to previously reported studies.^{13,14} A possible strategy to favor hydrophobic 3D-vdW stacking relies on increasing the polarity of the solvent used in self-assembly. When using solutions of up to 20% volume in methanol, however, only network architectures with no obvious 3D signature were observed, as previously reported²⁵ (Supporting Information Figure S1). In contrast, when using the pristine desiccated solvents for self-assembly (TCB and \ll 1% DMSO), a 3D network architecture is easily recognized (Figure 1a). Upon detailed inspection, bilayers are recognized thanks to domain boundaries between first and second layers (Figure 1b).

The existence of the second layer network is confirmed by the line profiles in Figure 1c. The HOPG substrate, first layer, and second layer of the network are depicted by red, green, and blue curves, respectively. It can be seen that the apparent STM height of the second layer with respect to HOPG is twice (~ 2 Å) the distance between the first and second layer (~ 1 Å). Notably, the high resolution in Figure 1b allows to identify empty pores in the line profiles (blue line Figure 1c). Such height differences are also observed in architectures without domain boundaries, where a seamless 3D-to-2D transition to single-layer islands occurs (Supporting Information Figure S2, close-up STM images are also shown in Supporting Information Figures S3 and S4).

STM images with enhanced molecular contrast of the bilayer domain boundary are depicted in Figure 1d, e and illustrate the details of molecular arrangements and the intra- and intermolecular interactions. As shown by the molecular models in Figure 1e, f, h, every triple hydrogen bond (two NH \cdots O and one NH \cdots N) between melamine and NTCDI is formed through combination of the diimide termination on both ends of the NTCDI molecule and melamine.²⁶ In the STM images, melamine molecules appear darker than NTCDI molecules due to their lower density of states;²⁶ thus, every tetramer consisting of one melamine and three NTCDI molecules in a ring structure appears as three-spot motif. Interestingly, the molecular models in Figure 1e, f reveal that the single-to-second layer domain boundaries observed in the large-area surveys are formed by NTCDI noncovalent dimerization (via two N-H \cdots O=C hydrogen bonds). The length of the NTCDI dimer (L_2) is 2.20 ± 0.05 nm, corresponding to twice the value of a single NTCDI molecule ($L_1 = 1.04 \pm 0.05$ nm, in Figure 1d). Note that these domain boundaries were also observed without an accompanying second-layer, but never in 20% methanol solutions. This points toward NTCDI-pairing being a phenomenon occurring

between two first-layers, which can be weakened with increased solution polarity. Meanwhile, a second layer can fully overlap one or two crystalline domains to the sides of the boundary. The crystalline domain formation can be monitored at the HOPG/network peripheries. Interestingly, the bilayer was found to expand directly from bilayer domain peripheries with a single growth rate and no preferred hexagonal symmetry direction on the pristine surface. Figure 1g shows a time lapse sequence of STM data, whereby the bilayer crystal growth can be estimated as 1.3 ± 0.3 nm² s⁻¹ per nm of island perimeter length, or 0.8 molecules nm⁻¹ s⁻¹. Because the domain boundaries are immobile and the bilayer does not overgrow single layers, we conclude that it preferentially expands as a bilayer. Consequently, wherever the surface shows NTCDI-pairing defects (cf. Figure 1a)—and hence a domain boundary—the bilayer growth terminates.

Concerning the vdW 2D-to-3D stacking configuration, it is clear that the second layer has the same pattern as the first layer, the experimental unit cell parameters of the second layer being $a = 2.8 \pm 0.1$ nm, $b = 2.8 \pm 0.1$ nm, which are identical with previously published values.^{25,26} The full (face-to-face) overlap of the second layer with the first can be unambiguously proven due to the strong mismatch of the experimental images with the molecular models showing alternate 2D vdW-stacking (Supporting Information Figure S5). We have previously reported that shifted, as opposed to face-to-face vdW, stacking occurs in order to avoid the electrostatic repulsion of carbonyl moieties between adlayers.¹⁴ Additionally, stacking of 2D layers has been reported in melamine and cyanuric acid cocrystals, where melamine and cyanuric acid stack face-to-face due to favored electrostatics at close interlayer distances (3.17 Å).^{27,28} Therefore, we suggest here that the interplay between higher vdW interactions (through the use of larger aromatic molecules) and reduced local electrostatic interactions (due to H-bonding), enables face-to-face vdW stacking of supramolecular networks, hence constituting prototype 3D supramolecular nanoporous frameworks. To give evidence of this, we investigated the energy dependence of vdW stacking between one melamine-NTCDI layer on top of another with the MMFF force field using a graphene substrate and periodic boundary conditions. After a local geometrical minimization of the top dimer fully eclipsing the bottom dimer (with a vdW stacking distance of 3.8 Å, Figure 1h), we translated the top dimer in X,Y to generate the energy map depicted in Figure 1i. The most favorable stacking energy during translation is found at a circle radius of 2–3 Å around the face-to-face stacking saddle point in Figure 1h. As expected, this shift is considerably smaller than the one found for the case of shifted vdW adlayers (shift ~ 15 Å), arising from electrostatic repulsion calculated with the same force field.¹⁴

Altogether, supramolecular 2D and 2D-to-3D growth with large crystalline domains develop best in the presence of a polar solvent such as methanol (Supporting Information Figure S1c), where only the strongest, triple H-bonds are favored. Decreasing solution polarity weakens molecule-solvent interactions and, hence, dispersion forces dominate, which maximize the contact surface between layers. As a result, aligned vertical growth is induced spontaneously. In addition, a decreasing solution polarity also provokes NTCDI pairing “defect” domain boundaries, constituted by double H-bonds only. These boundaries, however, are an important reference for studying 2D-to-3D growth by STM.

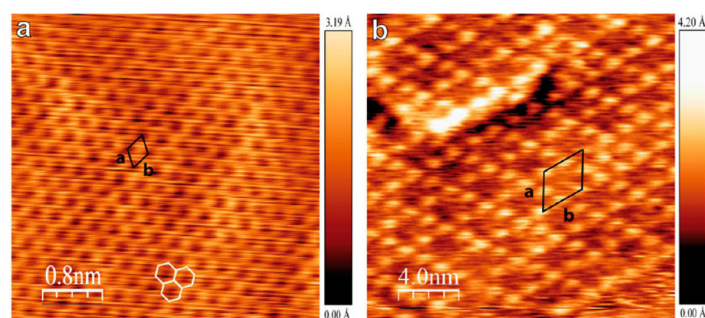


Figure 2. (a) High resolution STM image of CVD-grown graphene on copper foil with tunneling parameters of $I_t = 80$ pA, $V_t = 20$ mV. (b) Melamine-NTCDI network self-assembled at the solid-liquid interface on graphene/Cu with tunneling parameters of $I_t = 30$ pA, $V_t = -50$ mV. The ratio of melamine and NTCDI is $5 \mu\text{M}:8 \mu\text{M}$.

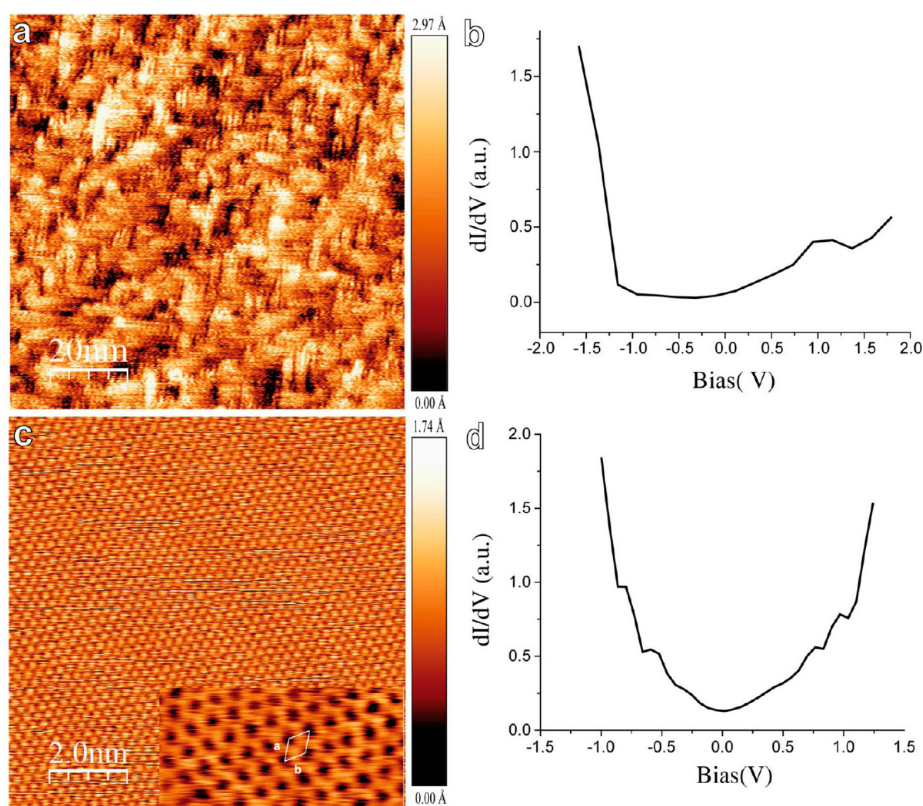


Figure 3. (a) High resolution STM image of a hydrogenated diamond surface obtained under ambient conditions with tunneling parameters of $I_t = 8$ pA, $V_t = 300$ mV. (b) Differential conductance dI/dV versus sample bias spectra for the hydrogenated diamond surface shown in (a). (c) STM image of transferred CVD-grown graphene on the hydrogenated diamond surface with tunneling parameters of $I_t = 80$ pA, $V_t = 20$ mV. Inset: Close-up of honeycomb structure of graphene with the unit cell of $a = 2.37 \pm 0.10$ Å and $b = 2.43 \pm 0.10$ Å. (d) Differential conductance dI/dV versus sample bias spectra for the G/H-C(100) template shown in (c). The z scales for (a) and (c) are 2.97 and 2.71 Å, respectively.

With a system capable of forming 3D reticular nanoporous networks, self-assembly on technologically relevant platforms can be tackled. This task is facilitated by considering the relation between HOPG and multilayer graphene, suggesting that assembly protocols on HOPG may be similarly applicable with graphene-passivated substrates. This argument has been recently supported by first case studies^{29–32} and is corroborated by the STM data reproduced in Figure 2. Figure 2a shows a

typical high resolution STM image of CVD-grown graphene on copper foil (G/Cu). In contrast to HOPG, where every second (β -site) carbon atom is visible in the STM under large tip-sample distances,³³ in graphene, α - and β -site atoms appear of equal intensity.³⁴ A few model hexagons are superimposed on the image to demonstrate the graphene honeycomb lattice. The corresponding unit cell is $a = 2.39 \pm 0.10$ Å and $b = 2.35 \pm 0.10$ Å, as previously reported in STM investigations.^{33,35,36}

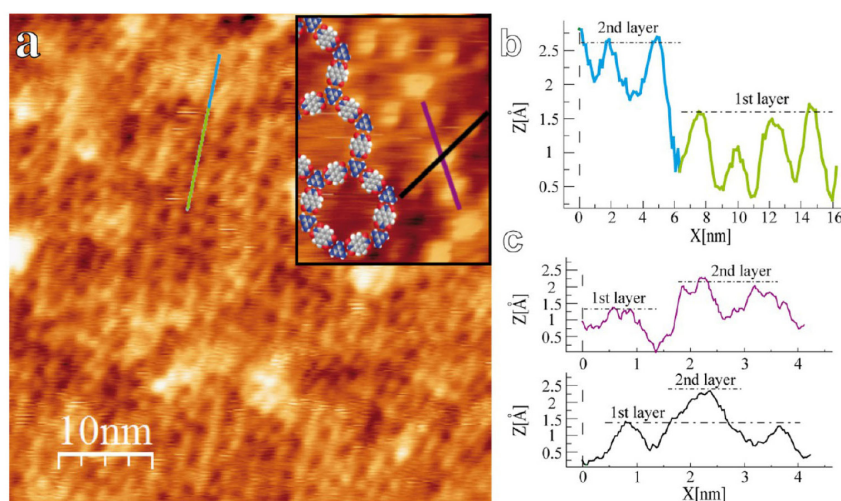


Figure 4. (a) STM image of bilayer melamine–NTCDI network assemblies at the solid–liquid interface on CVD-grown graphene/hydrogenated diamond surface. Inset: a close-up STM image of network with molecular model exhibited the same pattern with those on HOPG and CVD-grown graphene/Cu. (b) Cross-sectional line profile showing different height of bilayer corresponding to the colored solid lines in (a). (c) Cross-sectional line profiles corresponding to the colored solid lines in the inset of (a) show single molecules in the second layer. Tunneling parameters: $I_t = 20$ pA, $V_t = 200$ mV. The ratios of melamine and NTCDI for both are $8 \mu\text{M}:12 \mu\text{M}$.

Moreover, Figure 2b reveals that the melamine–NTCDI network forms a continuous 2D porous network on the G/Cu surface, with a unit cell of $a = 2.7 \pm 0.1$ nm and $b = 2.8 \pm 0.1$ nm. In addition, the melamine–NTCDI network was found to extend seamlessly across the surface defects inherited from the underlying copper substrate (shown in Figure 2b).

Inspired by these findings, the network formation can be explored on the graphene/H–C(100) diamond platform,³⁷ the latter being of technological importance,^{38,39} transparent (See Supporting Information Figure S6), conductive²⁴ and atomically flat. In particular, the fabrication of graphene-based devices provides an impetus to the planar sp^2 – sp^3 carbon-on-carbon technology.^{40,41} Figure 3a shows the STM topography of the H–C(100) surface where rows correspond to CH–CH dimer⁴² of the reconstructed surface,⁴³ with an average apparent roughness of ~ 0.5 Å on a length scale of 100 nm. The dimer rows run in orthogonal directions due to the existence of nanometer-sized surface domains.⁴² In a subsequent step, to obtain an all-carbon sp^2 – sp^3 transparent platform comprising a single graphene layer atop the diamond substrate, we transferred CVD graphene from copper foil to the hydrogenated diamond (for details see Supporting Information Figure S7). As shown in Figure 3c, CVD graphene transferred on H–C(100) diamond (G/H–C(100)) features a much lower roughness, making it ideal for long-range macroscopic patterning of molecularly precise supramolecular assemblies.

The electronic properties of the hybrid system are assessed by tunneling spectroscopy measurements and reveal marked changes following the graphene sheet transfer. The pertaining differential current–voltage curves for diamond and graphene are presented in Figure 3b and 3d, respectively. The spectrum depicted in Figure 3b is obtained from the diamond surface with hydrogen termination and shows a zero-current inflection point at around -1.2 V in good agreement with previous studies from Lud et al.,⁴⁴ which is tentatively assigned to the material's doping. By contrast, the G/H–C(100) conductance signature shows a clearly different behavior with a rather

symmetric onset of transport characteristics and steep voltage-dependent increases in both the negative and positive bias regime. Despite these peculiar electronic features, regular melamine–NTCDI networks are readily expressed on the all-carbon hybrid platform, as shown by the exemplary STM data in Figure 4a (for a large-scale image, cf. Supporting Information Figure S9). However, when the melamine–NTCDI network self-assembles onto the desired G/H–C(100) template, strong inhomogeneities in the contrast topography of each NTCDI molecule appear (cf. Figure 4a inset); line profiles in Figure 4c reveal differences of 1 Å. We tentatively assign the bright spots to single NTCDI molecules that are vdW-stacked on NTCDI molecules of the underlying network layer. Such aggregation tendency appears to oppose the 3D studies on HOPG, where the bilayer is reported to grow as a single entity. However, also on HOPG, when the surface is fully covered, few molecules with higher apparent heights can be individually observed to adsorb on top of a network (Supporting Information Figure S2). In fact, such aggregation tendency makes extended networks on G/H–C(100) difficult to image with high resolution (Supporting Information Figure S8). Despite this drawback, porous structures in the first and second layers can be clearly inferred from inspecting the data shown Figure 4a. The line profile in Figure 4b reveals apparent height differences between the bottom and top network of a magnitude corresponding to that observed on HOPG: the height of the first layer is around 1.5 Å with respect to the pore holes; the height of the second layer, depicted in blue color, amounts to 2.6 Å. Particularly, in the zoom-in image (Supporting Information Figure S9), even tetramers on top of the second layer, that is, a third network layer with an apparent height of 3.5 Å, can be observed.

It is important to note that extended third-layer crystalline networks were never identified. We tentatively attribute this to the low solution concentrations used, which are a requirement for avoiding phase separation.²⁵ Thus, it is suggested that dedicated self-assembly instrumentation with macroscopic

pressure, temperature, flow and stoichiometry control for multilayer formations could provide the necessary exquisite physicochemical control for vdW noncovalent synthesis or self-assembly of 3D macromolecular architectures.

In summary, we have fabricated a prototype 3D supramolecular framework on an all-carbon transparent hybrid sp^2 - sp^3 platform at the solid-liquid interface and ambient conditions. The platform consists on CVD graphene transferred to a technologically relevant high-quality hydrogenated CVD diamond substrate. Comparative studies of the nanoporous network on HOPG allowed to extract growth rates of the bilayers and showed how solvent controls the tendency of the bilayers to form boundaries, reflecting NTCDI-NTCDI interactions. Moreover, molecular mechanics studies gave insight into the preferential face-to-face vdW stacking of melamine-NTCDI dimers. Our work demonstrates how precise π -stacking of a polyaromatic molecule is possible in a bicomponent supramolecular network. These findings are especially important for the fabrication and optimization of organic semiconductor devices toward self-assembly assisted 3D molecular printing. In this context, our studies already introduce a promising electrode and modular architecture for molecularly precise optoelectronic or photovoltaic device elements.

■ ASSOCIATED CONTENT

Supporting Information

Experimental procedure, additional STM images, bilayer stacking models, diamond picture and transfer process. This material is available free of charge via the Internet at <http://pubs.acs.org>.

■ AUTHOR INFORMATION

Corresponding Authors

*C.-A. Palma. E-mail: c.a.palma@tum.de.

*J. V. Barth. E-mail: jvb@tum.de.

Author Contributions

[†]These authors contributed equally to this work.

Notes

The authors declare no competing financial interest.

■ ACKNOWLEDGMENTS

The Nanosystems Initiative Munich (NIM), European Research Council (ERC-through MolArt AdG 247299) and China Scholarship Council (CSC) are gratefully acknowledged for support. We thank Ueli Heiz for providing experimental infrastructure at the Institute of Physical Chemistry at TUM.

■ REFERENCES

- Barth, J. V.; Costantini, G.; Kern, K. *Nature* **2005**, *437*, 671–679.
- Ciesielski, A.; Palma, C. A.; Bonini, M.; Samori, P. *Adv. Mater.* **2010**, *22*, 3506–3520.
- Lehn, J. M. *Angew. Chem., Int. Ed.* **2013**, *52*, 2836–2850.
- O’Keeffe, M. *J. Chem. Soc. Rev.* **2009**, *38*, 1215–1217.
- Markoff, J., Designing the Next Wave of Computer Chips. *New York Times* Jan. 9, **2014**.
- Palma, C. A.; Samori, P. *Nat. Chem.* **2011**, *3*, 431–436.
- Cai, J. M.; Ruffieux, P.; Jaafar, R.; Bieri, M.; Braun, T.; Blankenburg, S.; Muoth, M.; Seitsonen, A. P.; Saleh, M.; Feng, X. L.; Mullen, K.; Fasel, R. *Nature* **2010**, *466*, 470–473.
- Palma, C.-A.; Diller, K.; Berger, R.; Welle, A.; Björk, J.; Cabellos, J. L.; Mowbray, D. J.; Papageorgiou, A. C.; Ivleva, N. P.; Matich, S.; Margapoti, E.; Niessner, R.; Menges, B.; Reichert, J.; Feng, X.; Räder, H. J.; Klappenberger, F.; Rubio, A.; Müllen, K.; Barth, J. V. *J. Am. Chem. Soc.* **2014**, *136*, 4651–4658.
- Gates, B. D.; Xu, Q.; Stewart, M.; Ryan, D.; Willson, C. G.; Whitesides, G. M. *Chem. Rev.* **2005**, *105*, 1171–1196.
- Theobald, J. A.; Oxtoby, N. S.; Phillips, M. A.; Champness, N. R.; Beton, P. H. *Nature* **2003**, *424*, 1029–1031.
- Kühne, D.; Klappenberger, F.; Decker, R.; Schlickum, U.; Brune, H.; Klyatskaya, S.; Ruben, M.; Barth, J. V. *J. Am. Chem. Soc.* **2009**, *131*, 3881–3883.
- Liu, X. H.; Guan, C. Z.; Ding, S. Y.; Wang, W.; Yan, H. J.; Wang, D.; Wan, L. J. *J. Am. Chem. Soc.* **2013**, *135*, 10470–10474.
- Blunt, M. O.; Russell, J. C.; Gimenez-Lopez, M. D. C.; Taleb, N.; Lin, X.; Schröder, M.; Champness, N. R.; Beton, P. H. *Nat. Chem.* **2011**, *3*, 74–78.
- Ciesielski, A.; Cadeddu, A.; Palma, C.-A.; Gorczyński, A.; Patroniak, V.; Cecchini, M.; Samori, P. *Nanoscale* **2011**, *3*, 4125–4129.
- Écija, D.; Auwärter, W.; Vijayaraghavan, S.; Seufert, K.; Bischoff, F.; Tashiro, K.; Barth, J. V. *Angew. Chem., Int. Ed.* **2011**, *50*, 3872–3877.
- Yaghi, O. M.; O’Keeffe, M.; Ockwig, N. W.; Chae, H. K.; Eddaoudi, M.; Kim, J. *Nature* **2003**, *423*, 705–714.
- Long, J. R.; Yaghi, O. M. *J. Chem. Soc. Rev.* **2009**, *38*, 1213–1214.
- Colson, J. W.; Woll, A. R.; Mukherjee, A.; Levendorf, M. P.; Spitzer, E. L.; Shields, V. B.; Spencer, M. G.; Park, J.; Dichtel, W. R. *Science* **2011**, *332*, 228–231.
- Zacher, D.; Shekhah, O.; Wöll, C.; Fischer, R. A. *Chem. Soc. Rev.* **2009**, *38*, 1418–1429.
- Bradshaw, D.; Garai, A.; Huo, J. *Chem. Soc. Rev.* **2012**, *41*, 2344–2381.
- Decher, G. *Science* **1997**, *277*, 1232–1237.
- Laquindanum, J. G.; Katz, H. E.; Dodabalapur, A.; Lovinger, A. *J. Am. Chem. Soc.* **1996**, *118*, 11331–11332.
- Roy, B.; Baire, P.; Nandi, A. K. *RSC Adv.* **2014**, *4*, 1708–1734.
- Garrido, J. A.; Härtl, A.; Dankerl, M.; Reitingner, A.; Eickhoff, M.; Helwig, A.; Müller, G.; Stutzmann, M. *J. Am. Chem. Soc.* **2008**, *130*, 4177–4181.
- Palma, C.-A.; Björk, J.; Bonini, M.; Dyer, M. S.; Llanes-pallas, A.; Bonifazi, D.; Persson, M.; Samori, P. *J. Am. Chem. Soc.* **2009**, *131*, 13062–13071.
- Teyssandier, J.; Battaglini, N.; Seydou, M.; Anquetin, G.; Diawara, B.; Sun, X.; Maurel, F.; Lang, P. *J. Phys. Chem. C* **2013**, *117*, 8737–8745.
- Prior, T. J.; Armstrong, J. A.; Benoit, D. M.; Marshall, K. L. *CrystEngComm* **2013**, *15*, 5838–5843.
- Ranganathan, A.; Pedireddi, V. R.; Rao, C. N. R. *J. Am. Chem. Soc.* **1999**, *121*, 1752–1753.
- Karmel, H. J.; Chien, T.; Demers-Carpentier, V.; Garramone, J. J.; Hersam, M. C. *J. Phys. Chem. Lett.* **2014**, *5*, 270–274.
- Wang, Q. H.; Hersam, M. C. *Nat. Chem.* **2009**, *1*, 206–211.
- Jarvinen, P.; Hamalainen, S. K.; Banerjee, K.; Hakkinen, P.; Ijas, M.; Harju, A.; Liljeroth, P. *Nano Lett.* **2013**, *13*, 3199–3204.
- Li, B.; Tahara, K.; Adisojojoso, J.; Vanderlinden, W.; Gendt, S. D.; Tobe, Y.; Feyter, S. D. *ACS Nano* **2013**, *7*, 10764–10772.
- Cisternas, E.; Stavale, F.; Flores, M.; Achete, C.; Vargas, P. *Phys. Rev. B* **2009**, *79*, 205431(1–5).
- Allen, M. J.; Tung, V. C.; Kaner, R. B. *Chem. Rev.* **2010**, *110*, 132–145.
- Park, S.-I.; Quate, C. F. *Appl. Phys. Lett.* **1986**, *48*, 112–114.
- Kibsgaard, J.; Lauritsen, J. V.; Laegsgaard, E.; Clausen, B. S.; Topsoe, H.; Besenbacher, F. *J. Am. Chem. Soc.* **2006**, *128*, 13950–13958.
- Childress, L.; Dutt, M. V. G.; Taylor, J. M.; Zibrov, A. S.; Jezcko, F.; Wrachtrup, J.; Hemmer, P. R.; Lukin, M. D. *Science* **2006**, *314*, 281–285.
- Härtl, A.; Schmich, E.; Garrido, J. A.; Hernando, J.; Catharino, S. C. R.; Walter, S.; Feulner, P.; Kromka, A.; Steinmüller, D.; Stutzmann, M. *Nat. Mater.* **2004**, *3*, 736–742.

- (39) Wu, Y.; Lin, Y. M.; Bol, A. A.; Jenkins, K. A.; Xia, F.; Farmer, D. B.; Zhu, Y.; Avouris, P. *Nature* **2011**, *472*, 74–78.
- (40) Yu, J.; Liu, G.; Sumant, A. V.; Goyal, V.; Balandin, A. A. *Nano Lett.* **2012**, *12*, 1603–1608.
- (41) Ma, Y.; Dai, Y.; Guo, M.; Huang, B. *Phys. Review. B* **2012**, *85*, 235448(1–5).
- (42) Bobrov, K.; Mayne, A.; Comtet, G.; Dujardin, G.; Hellner, L.; Hoffman, A. *Phys. Rev. B* **2003**, *68*, 195416(1–8).
- (43) Nimmrich, M.; Kittelmann, M.; Rahe, P.; Mayne, A. J.; Dujardin, G.; von Schmidsfeld, A.; Reichling, M.; Harneit, W.; Kühnle, A. *Phys. Rev. B* **2010**, *81*, 201403(1–4).
- (44) Lud, S. Q.; Niedermeier, M.; Koch, P. S.; Bruno, P.; Gruen, D. M.; Stutzmann, M.; Garrido, J. A. *Appl. Phys. Lett.* **2010**, *96*, 092109(1–3).

4.2 Photoresponse of Supramolecular Self-Assembled Networks on Graphene - Diamond Interfaces

The publication titled 'Photoresponse of supramolecular self-assembled networks on graphene - diamond interfaces' is presented in this section. The assembly process of active dye components approaching atomically-precise spatial disposition is studied. The results present a significant advance towards molecularly precise (multilayer organic) optoelectronic devices with modular control in three dimensions.

Solar cells based on organic dyes or pigments are studied since the late 1950s [131] due to their potentially low costs in the fabrication process including methods as spin-coating [132], printing [133] or self-assembly [134]. However, the structure of the interface which is formed between surface and active dye as well as the orientation of the dye within the thin film is barely known. STM is a powerful tool to image structures down to the atomic level and thus to control the reproducible formation of the device at the atomic scale.

Here, a supramolecular network consisting of a terylene diimide derivative dye (TDI) and melamine is employed to form a self-assembled bicomponent hydrogen bonded network on carbon supports, namely HOPG and graphene transferred on hydrogenated diamond (GHD). TDI belongs to the group of rylene dyes which are based on naphthalene units linked in the *peri* position and show outstanding chemical, thermal and photochemical stability [9]. In addition, rylenes have extended π -systems which allow to control and tune the optical properties. TDI exhibit the same binding moieties as NTCDI, as previously described in section 4.1, forming triple hydrogen bonded bicomponent supramolecular networks. In the presented paper, the self-assembly process of TDI and melamine is studied in TCB by STM at the solid-liquid interface on HOPG and GHD. The network exhibits an extended long-range ordered honeycomb structure. Since GHD is transparent, it offers the possibility to study the optical properties of self-assembled networks in back illumination geometries: the spectroscopic characterization can be performed by UV-vis transmission spectroscopy or upon back illumination in a STM. For these photoresponse experiments, the 2D layer is contacted with a Ga (or EGaIn) droplet as top electrode to measure current-voltage (I-V) characteristics. Our results show, that a bottom-up approach can be used to characterize the first macroscopic photoresponse of a bicomponent network.

The UV-vis and photoresponse experiments were performed by Sarah Wieghold together with Juan Li at the Physics Department E20 of TUM. Both authors contributed equally to this work.

Photoresponse of Supramolecular Self-Assembled Networks on Graphene-Diamond Interfaces

S. Wieghold, J. Li, P. Simon, M. Krause, Y. Avlasevich, C. Li, J. A. Garrido, U. Heiz, P. Samori, K. Müllen, F. Esch, J. V. Barth, C. A. Palma

Nature Communications, 2016, DOI: 10.1038/ncomms10700

Permanent weblink:

<http://www.nature.com/ncomms/2016/160225/ncomms10700/full/ncomms10700>

Copyright © (2016), Rights Managed by Nature Publishing Group.



ARTICLE

Received 20 Oct 2015 | Accepted 14 Jan 2016 | Published 25 Feb 2016

DOI: 10.1038/ncomms10700

OPEN

Photoresponse of supramolecular self-assembled networks on graphene-diamond interfaces

Sarah Wieghold^{1,2,*}, Juan Li^{2,3,*}, Patrick Simon^{3,4}, Maximilian Krause^{1,2}, Yuri Avlasevich⁵, Chen Li⁵, Jose A. Garrido^{3,4}, Ueli Heiz^{1,2}, Paolo Samori⁶, Klaus Müllen⁵, Friedrich Esch^{1,2}, Johannes V. Barth^{2,3} & Carlos-Andres Palma^{2,3}

Nature employs self-assembly to fabricate the most complex molecularly precise machinery known to man. Heteromolecular, two-dimensional self-assembled networks provide a route to spatially organize different building blocks relative to each other, enabling synthetic molecularly precise fabrication. Here we demonstrate optoelectronic function in a near-to-monolayer molecular architecture approaching atomically defined spatial disposition of all components. The active layer consists of a self-assembled terrylene-based dye, forming a bicomponent supramolecular network with melamine. The assembly at the graphene-diamond interface shows an absorption maximum at 740 nm whereby the photoresponse can be measured with a gallium counter electrode. We find photocurrents of 0.5 nA and open-circuit voltages of 270 mV employing 19 mW cm^{-2} irradiation intensities at 710 nm. With an *ex situ* calculated contact area of $9.9 \times 10^2 \mu\text{m}^2$, an incident photon to current efficiency of 0.6% at 710 nm is estimated, opening up intriguing possibilities in bottom-up optoelectronic device fabrication with molecular resolution.

¹Chemie-Department, Technische Universität München, Lichtenbergstraße 4, Garching 85748, Germany. ²Catalysis Research Center, Technische Universität München, Ernst-Otto-Fischer-Straße 1, Garching 85748, Germany. ³Physik-Department, Technische Universität München, James-Frank-Strasse 1, Garching 85748, Germany. ⁴Walter Schottky Institut, Technische Universität München, Am Coulombwall 4, Garching 85748, Germany. ⁵Max Planck Institute for Polymer Research, Ackermannweg 10, Mainz 55128, Germany. ⁶ISIS & icFRC, Université de Strasbourg & CNRS, 8 allée Gaspard Monge, Strasbourg 67000, France. *These authors contributed equally to this work. Correspondence and requests for materials should be addressed to K.M. (email: muellen@mpip-mainz.mpg.de) or to F.E. (email: friedrich.esch@ch.tum.de) or to J.V.B. (email: jvb@tum.de) or to C.-A.P. (email: c.a.palma@tum.de).

Elemental crystals, interfaces and (macro)molecules have become integral parts of modern semiconductor devices which are shaping twenty-first century technology. Thus far, the first generation of organic semiconductor devices, for example, light-emitting diodes¹ and photovoltaics², are based on (macro)molecules processed with a wide range of methods in an effort to make them compatible with the capabilities of the semiconductor industry. These methods consist mainly of thin film technologies, including spin-coating³, sublimation¹, printing⁴, crystallization⁵ and self-assembly^{6–8} fabrication procedures or combinations thereof⁹. However, the aforementioned strategies have been often centred around the fabrication and the tuning of the properties of the (macro)molecular active components in thin films¹⁰. Consequently, spatial orientation of both the active layer's components and their interfaces are not usually known with atomic precision. Thus, *a posteriori* characterization techniques are required and the final absolute atomic-scale spatial constitution of the device as a whole is rarely reproducible. Although an atomically precise layout of the constituting components is not always required for a device's function, it may be critical for its optimization¹¹. For instance, sensitizing interfaces with molecules was early recognized¹² as efficient means to photovoltaic charge generation. By optimizing the sensitizer surface area, this strategy became technologically viable^{13,14}. Similarly, by improving chemical precision over donor and acceptor polymers¹⁵, organic solar cell efficiencies grew rapidly¹⁶. Thus, it is clear that for a transition to a second generation of organic device engineering, their constituents must be fabricated not only with high interfacial and chemical control but also with exquisite spatio-temporal heteromolecular precision, where the absolute location of different molecular components is mastered and precisely known *a priori*. So far, device elements approaching such molecular precision employ single-molecule configurations^{17,18}, which are not yet ready to be implemented for large-area technological applications. One strategy for large-area, artificial molecularly precise device fabrication is to grow architectures from the bottom-up¹⁹, at interfaces with solutions²⁰ or under vacuum. Supramolecular hydrogen bonded^{21,22}, metal-organic^{23,24} or covalent^{25–27} multi-component surface-confined networks provide a route to precisely organize different building blocks relative to each other in two dimensions (2D). These 2D surface assemblies can be engineered^{28,29} with increasing level of prediction^{30,31} to afford device functionalities on top of specific substrates. In addition, 2D networks can act as templates for the growth of three-dimensional networks^{32,33}, paving the road towards vertical heteromolecular control via monolayer-by-monolayer growth. Such architectures may present precise interpenetrated morphologies³⁴ with ideal nanoporous and columnar order, which have long been considered optimal configurations for organic solar cells^{11,35}.

Here we demonstrate the photoresponse of a bicomponent supramolecular network (Fig. 1a) on transparent, graphene-passivated H-C(100) diamond (GHD) and employing a gallium droplet as a counter electrode (Fig. 1b). The network is built with a chromophore, consisting of a terylene diimide (TDI) derivative (**1**) and melamine (**2**). After initial molecular characterization by means of scanning tunnelling microscopy, we show generated photocurrents of (0.5 ± 0.2) nA and photovoltages of (270 ± 120) mV at 19 mW cm^{-2} irradiation intensities at 710 nm (uncertainties are s.d. in tenths of measurements for different sample preparations). We find incident photon to electron efficiencies (IPCE) at 710 nm of $(0.6 \pm 0.25)\%$ when estimating the contact area *ex situ*, yielding photocurrent densities of $(47 \pm 5) \mu\text{A cm}^{-2}$. Our work introduces bottom-up

supramolecular network engineering on 2D materials for molecularly precise function with atomically defined interfaces.

Results

Chemical design and synthesis. Heteromolecular recognition between tritopic melamine and complementary ditopic linkers via hydrogen bond formation was introduced as means to achieve hexagonal supramolecular architectures^{21,36}. By proper chemical design, the complementary linker can be engineered^{31,37} for self-assembly with increasing level of predictability at the solid-liquid interface, thereby decreasing the content of poorly ordered and glassy phases. For instance, we have previously shown that peripheral substitution of the linker favours the formation of networks over tightly packed patterns²². Further, the linker can be imbued with functional properties. Rylene dyes are poly(peri-naphthalene)s³⁸ that show a high photostability³⁹, which make them preferred constituents for application in optoelectronic devices. Extending the π -system of the dye allows for tuning the optical properties and thus, shifting the absorption maximum to higher wavelengths. At the same time, rylenes are known to be amongst the most efficient organic absorbers^{38,40}. Thus, rylenes are promising for the infrared regime with high transparency in the visible spectrum, for use in the next generation of facade and window building technology⁴¹. By introducing diimide terminations, the molecules acquire the supramolecular moiety necessary for triple hydrogen bond complementary recognition with the melamine cornerstone. Substituents at the bay position are used to improve the solubility³⁸ and favour porous network formation. Thus a novel TDI, bearing NH groups in the imide structure, is synthesized according to Fig. 2 (see Supplementary Methods for details). The presence of NH groups makes the solubility poor and purification of the rylene dyes rather difficult. Therefore, we use bulky 2,6-diisopropylphenyl groups in the starting one-pot reaction of perylene monoimide **3** and naphthalene monoimide **4** to create the soluble compound **5**. After bromination and phenoxylation steps, tetra(*t*-octylphenoxy) substituted **7**, showing outstanding solubility⁴², can be used in the following. Hydrolysis of the imide groups under basic conditions, results in bis-anhydride **8** which is reacted with ammonium acetate to afford the target **1**. In both cases the presence of four voluminous *t*-octylphenoxy groups made purification and processing possible. Comparing with soluble perylene diimide (PDI) analogues, TDIs have higher absorption coefficients, which render TDI a better light-harvesting efficiency⁴³. Moreover, the additional naphthalene unit in the TDI structure separates the tetraphenoxy groups and makes the TDI molecules less twisted⁴⁴. Thus, improved planarity and increased absorptivity^{38,40} render the engineered TDI supramolecular assemblies advantageous over shorter PDI assemblies^{21,45}.

Scanning tunnelling microscopy characterization. The successful formation of highly regular 2D supramolecular networks between **1** and **2** has been investigated *ex situ* (on a model substrate) and *in situ* (in the device configuration) by means of scanning tunnelling microscopy. Self-assembly experiments involved applying a mixture of **1** + **2** in 1,2,4-trichlorobenzene (TCB) with 1–5% of dimethylsulfoxide (DMSO), first on highly ordered pyrolytic graphite (HOPG, Fig. 3a,c) and then on transparent platforms made by graphene transferred to hydrogenated H-C(100) diamond (GHD). In the scanning tunnelling microscope (STM) images, molecular features can be resolved. Figure 3a shows how the observed hexagonal supramolecular features perfectly match the expected chemical structure in Fig. 3b. The molecular geometry was optimized with the

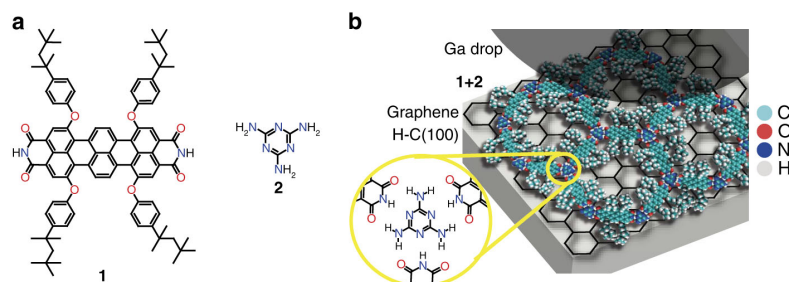


Figure 1 | Chemical structures of the molecules and setup. (a) Structure of TDI tetracarboxylic acid derivative (**1**) and melamine (**2**) (b). Schematic drawing of the photoresponse device setup including the ideal representation of the **1**+**2** mixture yielding a $[1_3 2_2]_n$ hexagonal supramolecular network via hydrogen bonds (yellow circle).

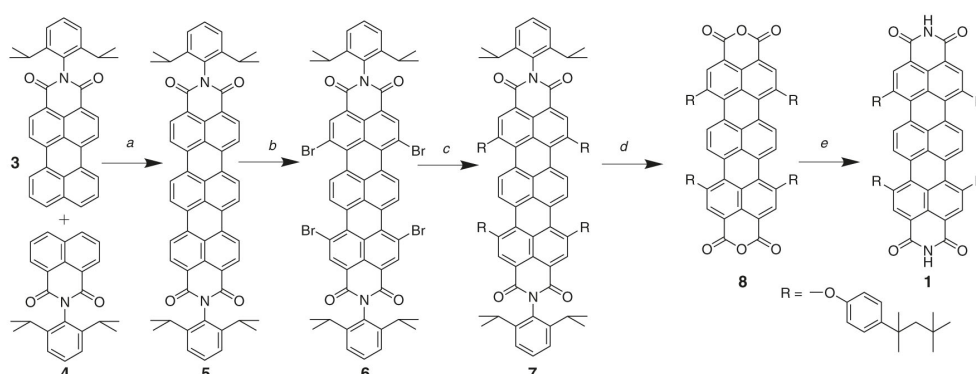


Figure 2 | Synthesis of novel TDI (1**).** (a) Base-induced fusion of naphthaleneimide and peryleneimide: diazabicyclo[4.3.0]non-5-ene, *t*-BuONa, diglyme, 130 °C, 3 h, 42%; (b) tetrabromination of TDI: Br₂, chloroform, reflux, 12 h, 75%; (c) phenoxylation of TDI: 4-(1,1,3,3-tetramethylbutyl)phenol, K₂CO₃, N-methylpyrrolidone, 80 °C, 8 h, 86%; (d) base-induced hydrolysis of bisimide into bis-anhydride: KOH, KF, 2-methyl-2-butanol, reflux, 53%; and (e) NH-imidization of terrylene bis-anhydride: ammonium acetate, propionic acid, reflux, 20%.

MMFF molecular force field. The 2D fast Fourier transform in Fig. 3c provides evidence for the regularity in the monolayer supported on HOPG. At GHD, only nanocrystalline hexagonal domains with sizes of tens of nanometres are monitored (Fig. 3d). Defects and impurities on GHD make the extended growth of crystalline bicomponent networks challenging, as discussed below. The experimental unit cell parameters for the network formation on GHD amount to $a = (3.9 \pm 0.2)$ nm and $b = (4.0 \pm 0.2)$ nm and $a, b = 62 \pm 1^\circ$, which are in perfect agreement with the values measured on HOPG.

UV-visible measurements. With an atomically flat and transparent platform such as GHD, capable of supporting the bimolecular 2D self-assembly, optical spectral properties of crystalline supramolecular layers can now be investigated. Thus, UV-vis absorption measurements were performed to distinguish between changes in the spectrum of **1** upon hydrogen bond recognition with **2**. The absorption spectra of (5 ± 1) μ l of the pristine **1** in a 12 μ M TCB solution and the pure TCB solvent on the diamond supported graphene surface are shown in Fig. 4a. Two distinct absorption peaks at 665 and 735 nm can be distinguished. This corresponds to a bathochromic shift of 46 and 66 nm with respect to UV-vis measurements in solution (Supplementary Fig. 1). Note that the TCB solvent used for the drop-casting shows no absorption in that wavelength range. The absorption peak-to-baseline signal of **1**, 0.012 at (735 ± 2) nm (see Supplementary

Fig. 1 for absolute absorption units), is indicative of approximately a monolayer of **1** when compared with the absorbance of monolayer perylene tetracarboxylic anhydride on graphene⁴⁶, ~ 0.007 at 702 nm. The molar attenuation coefficient of perylene tetracarboxylic anhydrides and PDIs⁴⁷ of $\sim 5 \times 10^4$ M⁻¹ cm⁻¹ is half the one of analogue TDI derivatives⁴⁸, close to 1×10^5 M⁻¹ cm⁻¹, at the respective absorbance maxima. When (5 ± 1) μ l solutions of **1** and **2** with a concentration ratio of 12 μ M:8 μ M are applied to the sample, a fivefold reduction of the signal of **1** is observed along with a bathochromic shift of the absorbance maximum to (740 ± 5) nm (Fig. 4b, uncertainties are s.d. between four different preparations). At least a 1.5-fold reduction in the absorbance is expected when comparing the molecular density of molecules of **1** (0.31 nm⁻¹) with that of molecules of **1** in the **1**+**2** network (0.21 nm⁻¹). Incidentally, a fourfold reduction of the absorbance maximum is also prominent in π -stacks of perylenes⁴⁹, in part due to specific surface reduction^{50,51}. Because the reduction of the absorbance is not an effect of variations in the drop-cast solution volume or concentration (see Supplementary Fig. 1), we suggest it is the combined effect of a looser packing (increased unit cell) of **1**+**2** and its aforementioned π -stacking³³.

Photoresponse characteristics. To preserve pristine molecular interfaces aiming at molecular precision, a gallium droplet has been used to soft-contact the supramolecular network. Current-

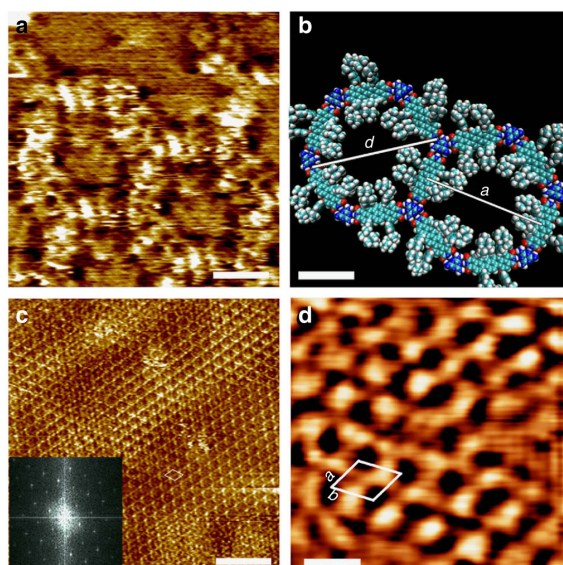


Figure 3 | STM images showing the assembly of 1+2 on graphite and graphene-passivated H-C(100) diamond substrates. (a) STM constant current image of 1+2 (16 μM : 10 μM) and underlying HOPG interface. Scale bar, 2 nm **(b)**. Molecular model minimized by the MMFF force field, the hexagonal size corresponding to the theoretical unit cell is $a = b = 4.2$ nm and the pore diameter is $d = 4.6$ nm. Scale bar, 2 nm **(c)**. STM large-area constant height image (12 μM :8 μM). (inset) 2D fast Fourier transform showing the high crystallinity of the assembly on HOPG. Unit cell $a = (4.1 \pm 0.2)$ nm, $b = (4.3 \pm 0.2)$ nm and $a, b = 65 \pm 2^\circ$. Scale bar 20 nm **(d)**. Gaussian-filtered STM constant current image of 1+2 on GHD. Unit cell $a = (3.9 \pm 0.2)$ nm and $b = (4.0 \pm 0.2)$ nm and $a, b = 62 \pm 2^\circ$. Area 13.8 nm². Tunneling parameters: average tunneling current (I_t) = 20 pA, sample voltage (V_s) = 300 mV. Scale bar, 5.5 nm.

voltage (IV) measurements have been used to characterize the device element's photoresponse. The top contact was fabricated by letting a liquid gallium droplet cover a blunt tungsten tip and slowly cool at room temperature (Fig. 5a). Gallium alloys have been widely used as a replacement for mercury for creating macroscopic device contacts with molecular layers^{52,53}. Our strategy consists of approaching the gallium-coated tip to the substrate and stabilizing it to a current setpoint of 2 nA at 100 mV, with the help of a modified STM. Contact and wetting of the GHD substrate by the gallium was inferred by fluorescence spectroscopy (see Methods and Supplementary Fig. 2) and by measuring the current during approach of the electrode to the surface (Supplementary Fig. 3). In addition, stepwise increase of the setpoint current shows stable semiconductor characteristics up to 100 nA (Supplementary Fig. 4). The large-area IV measurements were performed on the 1+2 on GHD and bare GHD substrates. The IV spectra of GHD (Fig. 5c, black dotted line) and 1+2 on GHD (Fig. 5c, blue dotted line) were recorded with a forward sweep of 200 mV s⁻¹. For obtaining the photoresponse characteristics, the current was recorded under illumination by a red light-emitting diode (LED) ($\lambda = 710$ nm) with a measured power of 19 mW cm⁻². When bare GHD was employed, no photoresponse was observed (Fig. 5c, black line). Conversely, the illuminated IV curve of the 12 μM :8 μM 1+2 on GHD monolayer photoresponse exhibits characteristic features (Fig. 5c, red line). Under illumination, a finite current flows at

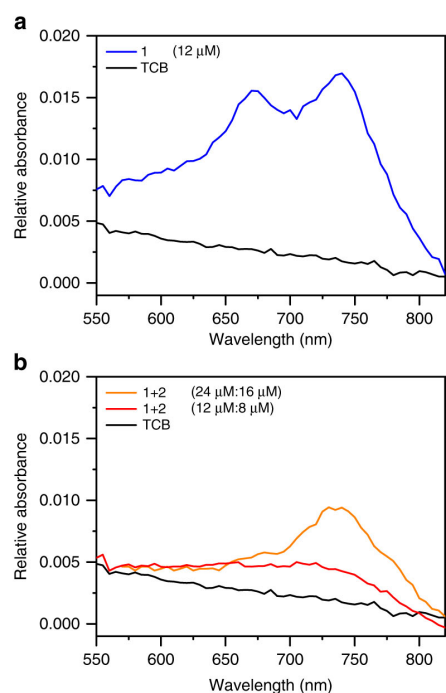


Figure 4 | UV-vis spectroscopy on graphene-passivated H-C(100) diamond. (a) 1 (12 μM) and pure TCB baseline spectra. **(b)**. 1+2 (12 μM :8 μM) and pure TCB baseline absorbance spectra. 1+2 (24 μM :16 μM) is also shown as additional evidence of strong absorbance reduction upon complexation with 2.

zero bias voltage, the short-circuit current I_{SC} . An average short-circuit current of $I_{SC} = (0.5 \pm 0.2)$ nA and open-circuit voltage of $V_{oc} = (270 \pm 120)$ mV were measured by illuminating the system with monochromatic light of 710 nm. Typical maximum and minimum values, from the average photoresponse characteristic, are also shown as shaded areas in Fig. 5c. In addition, IV curves were recorded by illuminating the 1+2 network on graphene with monochromatic light of 520 nm of 13 mW cm⁻² (Fig. 5d), where 1 does not absorb light. Indeed, no photocurrent was generated under 520 nm light irradiation conditions where TDI does not absorb. Figure 5e,f depict the back illumination geometries employed. Figure 5g shows the stability of the photovoltage generated by the junctions as a function of light on-off cycles (employing functionalized gallium tips, see Methods). The data corresponds to $\sim 25\%$ of various measured junctions. In the remaining junctions, a different regime is observed, where a clear increase in the current with 710 nm irradiation occurs but neither open-circuit voltage nor short-circuit current are detected (Fig. 5h). Because current-distance spectroscopy reveals a clear exponential dependence of the current with the distance, these junctions do not physically contact the substrate. Hence, this non-contact regime is attributed to a photoexcitation effect, where additional tunnelling channels are opened upon light exposure. All in all the results show that the supramolecular network based on 1+2 molecules specifically generates a photoresponse at the designated wavelength. It is instructive to approximate the tunnelling contact area of the gallium droplet ($\sim 250 \mu\text{m}$ diameter) to estimate photoconversion efficiencies. By *ex situ* contact junctions with

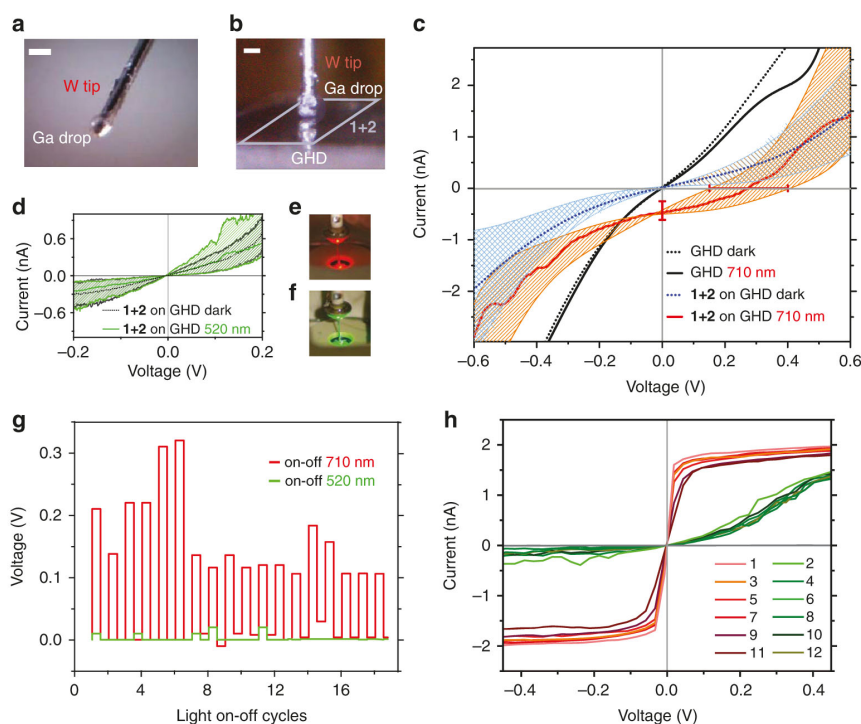


Figure 5 | Photoresponse of a supramolecular network optoelectronic device element. (a) Tungsten STM tip with a gallium droplet. (b) Gallium electrode in contact with the sample before the tunnelling spectroscopy measurements. (c) Current-voltage characteristics (contact regime see main text) of pristine GHD (black lines) and of **1+2** on GHD before (blue lines) and after (red lines) irradiation at $\lambda = 710$ nm (d) Current-voltage characteristics before (black lines) and after (green lines) $\lambda = 520$ nm photon irradiation. Approach parameters: $I_t = 2$ nA and $V_t = 100$ mV. Striped areas indicate the maximum and minimum currents observed in more than ten curves in a single junction, while error bars indicate the standard deviation for five junctions in three samples and are reported in the main text as $I_{SC} = (0.5 \pm 0.2)$ nA, $V_{oc} = (270 \pm 120)$ mV (e) Back illumination geometry with $\lambda = 710$ nm (f) Back illumination geometry with $\lambda = 520$ nm. (g) Open-circuit voltage for consecutive on-off irradiation cycles at 710 nm (red lines), followed by on-off cycles at $\lambda = 520$ nm (green lines) of **1+2**. Every set of six consecutive cycles was recorded with different junction (sample, tip) preparations. The constant dark voltage background for each set was subtracted (~ 0.05 V). For stability, these studies were performed with functionalized eutectic gallium-indium electrodes, see Methods. (h) Scanning tunnelling spectroscopy (non-contact regime, see main text) for consecutive irradiation cycles 1–12 at $\lambda = 710$ nm (red lines), followed by $\lambda = 520$ nm (green lines), showing drastic changes assigned to electron tunneling through photoexcited states. Setpoint parameters: $I_t = 1$ nA, $V_t = 300$ mV. For all panels, data shown was neither filtered nor averaged. Scale bars, 250 μ m.

insulating fluorescence dyes (see Methods and Supplementary Fig. 2), an area of $(9.9 \pm 0.6) \times 10^2 \mu\text{m}^2$ can be estimated for the *in situ* experiment. This area is roughly 2% of the projected area under the gallium electrode ($49 \times 10^3 \mu\text{m}^2$, using a radius of 125 μ m). With such estimation, current densities of $10^{-4} \text{ A cm}^{-2}$ at 0.5 V can be derived from the IV spectra. These current densities are comparable to those reported by contacting -S-C₁₆H₃₃ self-assembled monolayers-metal interfaces of similar contact areas⁵³, indicating a soft-contact. Further, with the derived photocurrent density of $J_{SC} = (47 \pm 5) \mu\text{A cm}^{-2}$ a monochromatic IPCE of $(0.6 \pm 0.25)\%$ can be estimated at 710 nm, 19 mW cm^{-2} irradiation intensities.

Discussion

We have fabricated surface-confined bicomponent assemblies on GHD based on a functional dye³⁸ absorbing at 740 nm. The active layer ideally consists of a self-assembled TDI-based supramolecular nanoporous network exhibiting nanocrystalline hexagonal order. Shorter diimide-based molecules like naphthalenes have been found to stack in the third dimension

through van der Waals face-to-face stacking³³. Thus, the employed system presents an avenue towards molecularly precise three-dimensional devices. During the measurements, atomically flat and transparent all-carbon GHD served as the photoanode, while a gallium junction was used as top cathode electrode, respectively. For sake of maintaining molecular integrity at the interface, as observed by STM in Fig. 3, a soft gallium electrode is used as a contact. The photoresponse exhibited a three order of magnitude increase in the short-circuit current, (0.5 ± 0.2) nA, with respect to the dark current (Supplementary Fig. 5) and an open-circuit voltage of (270 ± 120) mV. It is worth mentioning that average short-circuit current and open-circuit voltage for the single component **1** were measured as (0.09 ± 0.01) nA and (160 ± 60) mV, respectively. The reported open-circuit voltage values are close to the energy level difference between the highest occupied molecular orbital (HOMO) of **1** and the work function of graphene. The electrode work function is 4.5 eV (ref. 54) for graphene and 4.3 eV (ref. 55) for gallium. The calculated first excitation of **1** occurs at 1.6 eV (775 nm) and the HOMO of **1** is 4.8 eV below the vacuum level (Supplementary Fig. 6). The

correlation with the energy level difference might be coincidental, as the origins of the open-circuit voltage in excitonic solar cells are under intense discussion⁵⁶. In our setup, a full molecular monolayer is guaranteed by employing concentrations and volumes, equivalent to 3.8×10^{13} molecules of **1** per substrate (and similar amount for **2**). Considering a substrate area of $5 \times 5 \text{ mm}^2$ and three TDI molecules per **1** + **2** unit cell area of 13.8 nm^2 , a monolayer is formed with 5.4×10^{12} TDI molecules. The higher amount of molecules applied to the substrate was employed to compensate for ring stain effects when drying drop-casting solutions (see Supplementary Fig. 1). A peak UV-vis absorbance of 0.012 at $(735 \pm 2) \text{ nm}$ for **1** provides additional evidence of a molecular monolayer. Upon **1** + **2** supramolecular network formation, absorbance is reduced, as expected because the assembly of a porous architecture entails a lower molecular surface density. In addition, formation of π -aggregate layers^{49,50}, reduces the resulting absorbance cross section, as well as hydrogen bonding⁵⁷ where charge transfer is likely to occur⁵⁸.

Our estimate on the tunnelling contact area allows us to elaborate on the technological implications of photoresponsive surface assemblies. Previously reported optimized photovoltaic devices of thin films of precursor molecule **7** blended with an organic acceptor⁵⁹, featured IPCEs³⁵ of 0.3% at 700 nm. These thin films were prepared by spin-coating solutions of 13 mg ml^{-1} . The comparable estimate of an IPCE of $(0.6 \pm 0.25)\%$ at 710 nm for our system prepared by drop-casting a $5 \mu\text{l}$ of a solution 1,000 times more diluted (0.015 mg ml^{-1} or approximately $12 \mu\text{M}$) suggests that the photovoltaic response of few monolayers of self-assembled molecular architectures could outperform the response of bulk spin-coated materials. This is in part due to high internal quantum yields for monolayer absorbers or high collection efficiencies at interfaces, as reported for C_{60} -porphyrin mixed self-assembled dyads⁶⁰, natural photosystem-I^{18,61} and naturally occurring 2D crystals^{62,63}. In our configuration, two molecular interfaces are formed, one between **1** + **2** on GHD and one between **1** + **2** and gallium oxide on gallium. The oxide⁶⁴ tunnelling barrier between gallium and the supramolecular assembly forms a blocking-layer that prevents the efficient collection of photogenerated electrons at the gallium electrode. We suggest that the resulting photoresponsive device element is hole-only, that is, photogenerated holes are readily collected at the graphene photoanode, while electrons have to tunnel to the gallium electrode. Hence, it is expected that the tuning of the work function and of the appropriate tunnelling junction material (for example, allowing hole-only and electron-only transport in the pertinent contacts)⁶⁵ will radically improve the efficiency of monolayer-thin organic devices.

In summary, bottom-up modular self-assembled networks and 2D materials grant access to device fabrication with molecular precision. We have shown the first macroscopic (μm scale) photoresponse characterization of a bicomponent supramolecular interfacial assembly. By *ex situ* estimations of the tunnelling area, our non-optimized device element configuration yields an IPCE (at 710 nm) as high as 0.6% in air, opening novel avenues towards tandem photovoltaics from monolayer-thin sensitizers. More importantly, we highlighted how, more than a decade since the introduction of interfacial bottom-up modular self-assembly^{21,23,24} and *in situ* on-surface synthesis²⁵ for atomically precise fabrication, serious efforts are still required for molecularly precise device fabrication, with high throughput, large-area, dedicated analytical methods simply lacking. Our work motivates rapid progress in molecular engineered manufacturing and monolayer-by-monolayer molecular printing methods, which potentially grant access to exponential optimization of device performance.

Methods

CVD-grown graphene transfer and network formation. The experiments were performed under ambient conditions on CVD-grown graphene ($10 \times 10 \text{ mm}$ on a copper foil, Graphene Platform, Japan) on hydrogenated diamond (Element Six, thickness: $500 \mu\text{m}$) surface. A high purity diamond C-(100) plate was cleaned with pure *N*-methyl-2-pyrrolidone (NMP) and isopropanol sonication treatment. Oxidation of the substrate was conducted with oxygen microwave plasma (TePla 100-E): 600 s at 200 W load coil power and 50 Pa oxygen pressure at a constant oxygen flow rate equivalent to $90 \text{ cm}^3 \text{ min}^{-1}$ (SCCM). To ensure a high quality conductive termination, hydrogenation of the diamond surface was performed in a quartz tube reactor (Seki Technotron Corp.) of a microwave-coupled ASTEX plasma system with three steps: 750 W and 50 mbar hydrogen pressure at a constant hydrogen flow rate of 100 SCCM at 700°C for 15 min; 230 W, 10 mbar hydrogen pressure, 100 SCCM at 300°C for 10 min; 0 W, 10 mbar hydrogen pressure, 100 SCCM at 35°C for 30 min. The hydrogenated diamond was characterized via STM (Supplementary Fig. 7). After these treatments, the graphene layer was transferred^{66,67} on diamond H-C(100). Melamine (Fluka, 52549, 99%) was used as received. Dimethyl sulfoxide (DMSO, Sigma-Aldrich, 99.9%) and anhydrous 1,2,4-trichlorobenzene (TCB, Sigma-Aldrich, 99.9%) were used as solvents without further purification. Uncertainty values were derived from the standard deviation of the balance's linearity (Sartorius CPA2245). The mother solutions in 10% DMSO and 90% in TCB were sonicated and heated to 80°C and a dilution was prepared in TCB with a concentration ratio of **1** + **2** of $12 \mu\text{M}:8 \mu\text{M}$. The network was obtained by drop-casting ($5 \pm 1 \mu\text{l}$) of **1** + **2** on GHD.

Scanning tunnelling microscopy measurements. STM measurements (Agilent Technologies 5,100) were performed in constant current and constant height mode. The scanning tips were prepared by mechanically cutting a Pt/Ir wire (80:20%, Goodfellow, UK). STM data were analysed with the free WSxM software (Nanotec Electronica S.L., Spain) and the Gwyddion software⁶⁸. All images, except Fig. 3c with Gaussian filtering, are shown with line-wise flattening to remove tilting effect of the substrate plane. The network structures were modelled by the Merck modular force field (MMFF)⁶⁹. Supplementary Fig. 8 reports the STM data of the molecule of **1** in HOPG.

UV-visible absorption spectroscopy. UV-vis measurements were performed with a UV/VIS/NIR Spectrometer, Lambda 900 (Perkin Elmer). The spectra were recorded at the full spectra range (2,000–200 nm) with 5 nm data interval, 0.32 and 0.68 s integration time for UV-vis and NIR, respectively. For absorption measurements, $(5 \pm 1) \mu\text{l}$ of **1** + **2** ($12 \mu\text{M}:8 \mu\text{M}$) in 1,2,4-Trichlorobenzene (TCB, Sigma-Aldrich, 99.9%) were drop-casted on GHD and dried in air. The spectrum was averaged 10 times and is plotted versus the wavelength for each sample.

Photoresponse measurements. *IV* measurements were performed with a home-built STM described in detail elsewhere⁷⁰. A blunt tungsten tip was dipped into a heated gallium droplet and directly mounted into the tip holder of the scanner. The gallium electrode was approached to the surface with approach parameters of 2 nA and 100 mV. The spectroscopy data were recorded with a forward sweep rate of 200 mV s^{-1} using a Femto pre-amplifier. For recording the on-off cycle photovoltages in Fig. 5g, EGaln electrodes coated with alkyl thiols were employed for increased stability. The tungsten blunt tips were dipped in EGaln (495425, Sigma-Aldrich) until a smooth coating was obtained and subsequently immersed in a pure solution of 1-dodecanethiol (471364, Sigma-Aldrich) for 15 min. These *IV* measurements were independently performed in an Agilent Technologies 5,100 using a logarithmic current amplifier to avoid current saturation. Before each single tunnelling spectroscopy measurement, the feedback vertical position of the electrode was regulated again to a tunnelling current of 1 nA and a voltage of 300 mV and turned off. The data were recorded with a forward sweep rate of 20 mV s^{-1} . For the illumination, a 710 nm (30 mW, 18°, Roithner Lasertechnik, Austria) and 520 nm (9,600 mCd, 123 mW, 30°, Nichia, Japan) LED were used. The photovoltaic detection limit of our setup is 90 mV, calculated as three times the standard deviation of the dark voltage. The acquired data in Fig. 5c,d,g corresponds to stable contact junctions (no observable oscillations in the junction *z* axis piezo electric control nor identifiable non-contact tunnelling junction formation, see main text) among tenths of different area surveys on four different samples.

Fluorescence measurement of the Ga droplet contact area. A Ga droplet was prepared as employed for the photocurrent measurements. The droplet was brought into tunnelling contact with a thin film of fluorescent dye on HOPG surface with the same approach and current parameters used in the STM measurement. By employing a nm-thick film of an insulating dye Rhodamin B (Radiant Dyes, Wermelskirchen), a contact junction forms, implying physical contact with the monolayer. The physical contact of the gallium droplet with a thick film of Rhodamin B leads to a higher deformation of the droplet, increasing the contact area in comparison to the photoresponse contacts. Therefore, this method accurately estimates an upper bound to the actual device element contact area and therefore, a minimum current density and efficiency. To form the nm-thick film, HOPG was spin-coated (480 r.p.m.) three times with $10 \mu\text{l}$ of a saturated solution of

Rhodamin B in acetone, and dried between each application. The tip was retracted from the surface, fixed to a microscope slide and imaged under fluorescence conditions with a fluorescence microscope (Leica DMI 3000B, Wetzlar). The image of the tip is shown in Supplementary Fig. 2 with enhanced contrast to make the contour of the tip visible (darker area). From the raw data (greyscale TIFF-image), the number of pixels with brightness higher than a certain threshold was extracted. From the length scale per pixel (known from calibration), the total area corresponding to the pixels was calculated. The threshold was set to a clear gap between brighter and darker pixels in the histogram and the corresponding area in the image was identified.

References

- Tang, C. W. & VanSlyke, S. A. Organic electroluminescent diodes. *Appl. Phys. Lett.* **51**, 913–915 (1987).
- Tang, C. W. 2-Layer organic photovoltaic cell. *Appl. Phys. Lett.* **48**, 183–185 (1986).
- Burroughes, J. H. *et al.* Light-emitting diodes based on conjugated polymers. *Nature* **347**, 539–541 (1990).
- Hebner, T. R., Wu, C. C., Marcy, D., Lu, M. H. & Sturm, J. C. Ink-jet printing of doped polymers for organic light emitting devices. *Appl. Phys. Lett.* **72**, 519–521 (1998).
- deBoer, R. W. L., Gershenson, M. E., Morpurgo, A. F. & Podzorov, V. Organic single-crystal field-effect transistors. *Phys. Status Solidi A* **201**, 1302–1331 (2004).
- Halik, M. & Hirsch, A. The potential of molecular self-assembled monolayers in organic electronic devices. *Adv. Mater.* **23**, 2689–2695 (2011).
- Yamamoto, Y. *et al.* Photoconductive coaxial nanotubes of molecularly connected electron donor and acceptor layers. *Science* **314**, 1761–1764 (2006).
- Wasielewski, M. R. Self-assembly strategies for integrating light harvesting and charge separation in artificial photosynthetic systems. *Acc. Chem. Res.* **42**, 1910–1921 (2009).
- Briseno, A. L. *et al.* Patterning organic single-crystal transistor arrays. *Nature* **444**, 913–917 (2006).
- Murphy, A. R. & Fréchet, J. M. J. Organic semiconducting oligomers for use in thin film transistors. *Chem. Rev.* **107**, 1066–1096 (2007).
- Heeger, A. J. 25th anniversary article: bulk heterojunction solar cells: understanding the mechanism of operation. *Adv. Mater.* **26**, 10–27 (2014).
- Vlachopoulos, N., Liska, P., Augustynski, J. & Grätzel, M. Very efficient visible-light energy harvesting and conversion by spectral sensitization of high surface-area polycrystalline titanium-dioxide films. *J. Am. Chem. Soc.* **110**, 1216–1220 (1988).
- O'Regan, B. & Grätzel, M. A low-cost, high-efficiency solar-cell based on dye-sensitized colloidal TiO₂ films. *Nature* **353**, 737–740 (1991).
- Hagfeldt, A., Boschloo, G., Sun, L. C., Kloo, L. & Pettersson, H. Dye-sensitized solar cells. *Chem. Rev.* **110**, 6595–6663 (2010).
- Scharber, M. C. *et al.* Design rules for donors in bulk-heterojunction solar cells - towards 10% energy-conversion efficiency. *Adv. Mater.* **18**, 789–794 (2006).
- Krebs, F. C., Espinosa, N., Hoesel, M., Sondergaard, R. R. & Jorgensen, M. 25th anniversary article: rise to power-OPV-based solar parks. *Adv. Mater.* **26**, 29–38 (2014).
- Park, H. *et al.* Nanomechanical oscillations in a single-C-60 transistor. *Nature* **407**, 57–60 (2000).
- Gerster, D. *et al.* Photocurrent of a single photosynthetic protein. *Nat. Nanotechnol.* **7**, 673–676 (2012).
- Palma, C.-A. & Samori, P. Blueprinting macromolecular electronics. *Nat. Chem.* **3**, 431–436 (2011).
- Rabe, J. P. & Buchholz, S. Commensurability and mobility in two-dimensional molecular patterns on graphite. *Science* **253**, 424–427 (1991).
- Theobald, J. A., Oxtoby, N. S., Phillips, M. A., Champness, N. R. & Beton, P. H. Controlling molecular deposition and layer structure with supramolecular surface assemblies. *Nature* **424**, 1029–1031 (2003).
- Palma, C.-A. *et al.* Tailoring bicomponent supramolecular nanoporous networks: phase segregation, polymorphism, and glasses at the solid-liquid interface. *J. Am. Chem. Soc.* **131**, 13062–13071 (2009).
- Stepanow, S. *et al.* Steering molecular organization and host-guest interactions using two-dimensional nanoporous coordination systems. *Nat. Mater.* **3**, 229–233 (2004).
- Barth, J. V. Molecular architectonic on metal surfaces. *Annu. Rev. Phys. Chem.* **58**, 375–407 (2007).
- Grill, L. *et al.* Nano-architectures by covalent assembly of molecular building blocks. *Nat. Nanotechnol.* **2**, 687–691 (2007).
- Zwaneveld, N. A. *et al.* Organized formation of 2D extended covalent organic frameworks at surfaces. *J. Am. Chem. Soc.* **130**, 6678–6679 (2008).
- Ciesielski, A. *et al.* Dynamic covalent chemistry of bisimines at the solid/liquid interface monitored by scanning tunnelling microscopy. *Nat. Chem.* **6**, 1017–1023 (2014).
- Barth, J. V., Costantini, G. & Kern, K. Engineering atomic and molecular nanostructures at surfaces. *Nature* **437**, 671–679 (2005).
- Ciesielski, A., Palma, C.-A., Bonini, M. & Samori, P. Towards supramolecular engineering of functional nanomaterials: pre-programming multi-component 2D self-assembly at solid-liquid interfaces. *Adv. Mater.* **22**, 3506–3520 (2010).
- Palma, C.-A., Cecchini, M. & Samori, P. Predicting self-assembly. *Chem. Soc. Rev.* **41**, 3713–3730 (2012).
- Whitelam, S. *et al.* Common physical framework explains phase behavior and dynamics of atomic, molecular, and polymeric network formers. *Phys. Rev. X* **4**, 011044–1 011044-12 (2014).
- Blunt, M. O. *et al.* Guest-induced growth of a surface-based supramolecular bilayer. *Nat. Chem.* **3**, 74–78 (2011).
- Li, J. *et al.* Three-dimensional bicomponent supramolecular nanoporous self-assembly on a hybrid all-carbon atomically flat and transparent platform. *Nano Lett.* **14**, 4486–4492 (2014).
- Halls, J. J. M. *et al.* Efficient photodiodes from interpenetrating polymer networks. *Nature* **376**, 498–500 (1995).
- Gunes, S., Neugebauer, H. & Sariciftci, N. S. Conjugated polymer-based organic solar cells. *Chem. Rev.* **107**, 1324–1338 (2007).
- Zerkowski, J. A., Seto, C. T. & Whitesides, G. M. Solid-state structures of rosette and crinkled tape motifs derived from the cyanuric acid melamine lattice. *J. Am. Chem. Soc.* **114**, 5473–5475 (1992).
- Palma, C.-A., Samori, P. & Cecchini, M. Atomistic simulations of 2D bicomponent self-assembly: from molecular recognition to self-healing. *J. Am. Chem. Soc.* **132**, 17880–17885 (2010).
- Weil, T., Vosch, T., Hofkens, J., Peneva, K. & Müllen, K. The rylene colorant family—tailored nanoemitters for photonics research and applications. *Angew. Chem. Int. Ed. Engl.* **49**, 9068–9093 (2010).
- Wöll, D. *et al.* Polymers and single molecule fluorescence spectroscopy, what can we learn? *Chem. Soc. Rev.* **38**, 313–328 (2009).
- Chen, L., Li, C. & Müllen, K. Beyond perylene diimides: synthesis, assembly and function of higher rylene chromophores. *J. Mater. Chem. C* **2**, 1938–1956 (2014).
- Li, G., Zhu, R. & Yang, Y. Polymer solar cells. *Nat. Photon.* **6**, 153–161 (2012).
- Nolde, F. *et al.* Synthesis and modification of terrylenediimides as high-performance fluorescent dyes. *Chem. Eur. J.* **11**, 3959–3967 (2005).
- Avlasevich, Y., Li, C. & Müllen, K. Synthesis and applications of core-enlarged perylene dyes. *J. Mater. Chem.* **20**, 3814–3826 (2010).
- Würthner, F. Bay-Substituted Perylene & Bisimides Twisted fluorophores for supramolecular chemistry. *Pure Appl. Chem.* **78**, 2341–2349 (2006).
- Madueno, R., Raisanen, M. T., Silien, C. & Buck, M. Functionalizing hydrogen-bonded surface networks with self-assembled monolayers. *Nature* **454**, 618–621 (2008).
- Huang, S. *et al.* Molecular selectivity of graphene-enhanced Raman scattering. *Nano Lett.* **15**, 2892–2901 (2015).
- Würthner, F. *et al.* Preparation and characterization of regioisomerically pure 1,7-disubstituted perylene bisimide dyes. *J. Org. Chem.* **69**, 7933–7939 (2004).
- Pschirer, N. G., Kohl, C., Nolde, T., Qu, J. Q. & Müllen, K. Pentarylene- and hexarylenebis(dicarboximide)s: near-infrared-absorbing polyaromatic dyes. *Angew. Chem. Int. Ed. Engl.* **45**, 1401–1404 (2006).
- Chen, Z. J. *et al.* Photoluminescence and conductivity of self-assembled π - π stacks of perylene bisimide dyes. *Chem. Eur. J.* **13**, 436–449 (2007).
- Spano, F. C. The spectral signatures of frenkel polarons in h- and j-aggregates. *Acc. Chem. Res.* **43**, 429–439 (2010).
- Weigand, R., Rotermund, F. & Penzkofer, A. Aggregation dependent absorption reduction of indocyanine green. *J. Phys. Chem. A* **101**, 7729–7734 (1997).
- Nijhuis, C. A., Reus, W. F., Siegel, A. C. & Whitesides, G. M. A molecular half-wave rectifier. *J. Am. Chem. Soc.* **133**, 15397–15411 (2011).
- Nijhuis, C. A., Reus, W. F., Barber, J. R. & Whitesides, G. M. Comparison of SAM-based junctions with Ga₂O₃/Egall top electrodes to other large-area tunnelling junctions. *J. Phys. Chem. C* **116**, 14139–14150 (2012).
- Giovanetti, G. *et al.* Doping graphene with metal contacts. *Phys. Rev. Lett.* **101**, 026803-1 026803-4 (2008).
- Srisonphan, S., Jung, Y. S. & Kim, H. K. Metal-oxide-semiconductor field-effect transistor with a vacuum channel. *Nat. Nanotechnol.* **7**, 504–508 (2012).
- Gregg, B. A. Excitonic solar cells. *J. Phys. Chem. B* **107**, 4688–4698 (2003).
- Llanes-Pallas, A. *et al.* Engineering of supramolecular H-bonded nanopolygons via self-assembly of programmed molecular modules. *J. Am. Chem. Soc.* **131**, 509–520 (2009).
- Reece, S. Y. & Nocera, D. G. Proton-coupled electron transfer in biology: results from synergistic studies in natural and model systems. *Annu. Rev. Biochem.* **78**, 663–699 (2009).
- Gorenflot, J. *et al.* Detailed study of N,N'-(diisopropylphenyl)-terrylene-3,4:11,12-bis(dicarboximide) as electron acceptor for solar cells application. *Synth. Met.* **161**, 2669–2676 (2012).
- Imahori, H. & Fukuzumi, S. Porphyrin- and fullerene-based molecular photovoltaic devices. *Adv. Funct. Mater.* **14**, 525–536 (2004).

61. Carmeli, I., Frolov, L., Carmeli, C. & Richter, S. Photovoltaic activity of photosystem I-based self-assembled monolayer. *J. Am. Chem. Soc.* **129**, 12352–12353 (2007).
62. Bernardi, M., Palumbo, M. & Grossman, J. C. Extraordinary sunlight absorption and one nanometer thick photovoltaics using two-dimensional monolayer materials. *Nano Lett.* **13**, 3664–3670 (2013).
63. Lee, C. H. *et al.* Atomically thin P-N junctions with van Der Waals heterointerfaces. *Nat. Nanotechnol.* **9**, 676–681 (2014).
64. Cechal, J. *et al.* Characterization of oxidized gallium droplets on silicon surface: an ellipsoidal droplet shape model for angle resolved X-ray photoelectron spectroscopy analysis. *Thin Solid Films* **517**, 1928–1934 (2009).
65. Shieh, J. T. *et al.* The effect of carrier mobility in organic solar cells. *J. Appl. Phys.* **107**, 084503–1 084503-9 (2010).
66. Yan, Z. *et al.* Toward the synthesis of wafer-scale single-crystal graphene on copper foils. *ACS Nano* **6**, 9110–9117 (2012).
67. Li, X. *et al.* Large-area synthesis of high-quality and uniform graphene films on copper foils. *Science* **324**, 1312–1314 (2009).
68. Nečas, D. & Klapetek, P. Gwyddion: an open-source software for SPM data analysis. *Cent. Eur. J. Phys.* **10**, 181–188 (2012).
69. Halgren, T. A. Merck molecular force field. I. Basis, form, scope, parameterization, and performance of MMFF94. *J. Comput. Chem.* **17**, 490–519 (1996).
70. Wilms, M., Kruff, M., Bermes, G. & Wandelt, K. A new and sophisticated electrochemical scanning tunneling microscope design for the investigation of potentiodynamic processes. *Rev. Sci. Instrum.* **70**, 3641–3650 (1999).

Acknowledgements

This work was supported by the European Commission through the European Research Council projects MolArt (GA-247299) and SUPRAFUNCTION (GA-257305) and the Graphene Flagship (GA-604391), as well as by the DFG Excellence Clusters Nanosystems Initiative Munich (NIM) and Munich Center for Advanced Photonics (MAP). We thank Katharina Henneberg for the fluorescence measurements and Daniel Mosegui for discussions. J.L. thanks the China Scholarship Council for financial support. S.W. thanks Lea Nienhaus for additional data. We gratefully acknowledge the collaboration with

Martino Saracino and Klaus Wandelt on the instrumentation development. P. Samori acknowledges the Agence Nationale de la Recherche through the LabEx project Chemistry of Complex Systems (ANR-10-LABX-0026_CSC) and the International Center for Frontier Research in Chemistry (icFRC).

Author contributions

S.W. and J.L. contributed equally to the work. S.W., J.L., M.K. and C.-A.P. performed the UV-vis and *IV* spectroscopy experiments. J.L. and C.-A.P. performed the STM experiments. Y.A., C.L. and K.M. synthesized the molecules. P. Samori, F.E., J.V.B. and C.-A.P. planned the experiments. P. Simon, J.A.G. and U.H. developed experimental infrastructure. S.W., F.E., J.V.B. and C.-A.P. wrote the manuscript. All authors discussed the manuscript. K.M. and C.-A.P. supervised the research.

Additional information

Supplementary Information accompanies this paper at <http://www.nature.com/naturecommunications>

Competing financial interests: The authors declare no competing financial interests.

Reprints and permission information is available online at <http://npg.nature.com/reprintsandpermissions/>

How to cite this article: Wieghold, S. *et al.* Photoresponse of supramolecular self-assembled networks on graphene-diamond interfaces. *Nat. Commun.* **7**:10700 doi: 10.1038/ncomms10700 (2016).



This work is licensed under a Creative Commons Attribution 4.0 International License. The images or other third party material in this article are included in the article's Creative Commons license, unless indicated otherwise in the credit line; if the material is not included under the Creative Commons license, users will need to obtain permission from the license holder to reproduce the material. To view a copy of this license, visit <http://creativecommons.org/licenses/by/4.0/>

4.3 Conclusion

In this chapter, the self-assembly process of two moieties, namely NTCDI and TDI in combination with a linker molecule (melamine) was studied at the solid-liquid interface. It was shown, that a highly ordered supramolecular network can spontaneously form at the interface between a solvent and a carbon-based substrate.

This bottom-up of an ordered porous host structure highlights the preferential face-to-face vdW stacking of NTCDI-melamine dimers and its influence on the ordering in the third dimension. By changing the polarity of the solvent, the transition can be influenced and directed. This prototype 3D network was successfully fabricated on carbon-based supports, HOPG and CVD graphene, allowing to choose at will an optimal platform for sp^2 - sp^3 carbon-on-carbon optoelectronic technology.

In addition, photovoltaic response of a bicomponent supramolecular network consisting of TDI and melamine on a transparent graphene platform, GHD, was demonstrated for the first time. This technologically relevant characterization of the monolayer network was shown by using a gallium droplet as a counter electrode. The results pave the way towards atomically precise (opto)electronic technology including molecularly engineered manufacturing and printing methods.

5 Conclusion and Outlook

The recent spotlight on supported nanostructures on various support materials has attracted attention in the context of developing conversion and storage systems for renewable energy vectors. At the present stage, nanostructures have shown their great potential in combination with novel preparation methods to overcome the limitations regarding the ordering of the active layer as well as building stable configurations on the surface.

In this thesis, several approaches have been explored to generate stable functional nanostructures at the solid-liquid interface:

1. Bottom-up self-assembly of hydrogen-bonded, porous mono- and bilayer networks for cluster and nanoparticle **trapping**
2. Implementation of all-carbon, transparent supports, together with photoabsorbing building blocks to generate organic monolayer networks with **photovoltaic response**
3. Deposition of Pt clusters on engineered, transparent Au films for indirect **plasmonic activation**
4. Immobilization of wet-chemically synthesized Pt nanoparticles on self-assembled thiol monolayers on Au for **electrocatalysis with tunable decoupling from the substrate**

Where possible, these nanostructures have been studied in a twofold way, on the atomic scale by scanning tunneling microscopy techniques (ECSTM or SMA-STM) as well as on the macroscopic scale by various methods - under illumination with extended electrodes (2), by measuring the kinetics of photocatalytic (3) or by integral electrochemical characterization techniques (RDE, 4).

In detail, the following projects have been accomplished:

1. The preparation of self-assembled supramolecular bicomponent networks on all carbon-based supports was shown for NTCDI while employing melamine as a linker molecule. This bottom-up approach opened the possibility to grow ordered and long-range structures towards robust, modular and predictable 2D optoelectronic materials. The transition of 2D to 3D materials was demonstrated by changing the polarity of the solvent. Thereby, important parameters as e.g. growth rate, layer formation and intermolecular interactions were determined.
2. In addition, TDI was introduced as novel absorber material and the formation was studied with graphene attaining molecular precise disposition of all elements at the interface.

- The presented results showed the first characterization of a supramolecular network and its macroscopic photoresponse under monochromatic illumination. This results will open the possibility to scale up the device configuration and measure its photoresponse under standard conditions. Further, it can help to build stacked monolayer photovoltaic elements by intercalating dye molecules between 2D electrode materials as e.g. layers of graphene.
3. Unselected platinum clusters were employed to decorate a plasmonically active thin gold film. A structured thin gold film was fabricated exhibiting a long-range and extended island structure allowing for plasmon excitation in the Kretschmann configuration. It was shown, that the excitation of surface plasmons reduce the tunneling current while acting as a rectified DC component in the tunneling junction. In addition, the indirect coupling of gold plasmons into platinum clusters lowered the tunneling barrier and thus, an enhanced tunneling signal was seen on the clusters. This enhanced catalytic behavior was demonstrated by the oxidative decomposition of MB at ambient conditions. The presented results open a new possibility to couple surface plasmons indirectly into small clusters by employing a plasmonically active support. The presented results can help to clarify the generation of carriers which are responsible for the electrical properties of a device. Further, the electric field can be tuned at the junction resulting in a Stark effect which allows to gain informations of band gap changes as well as transition moments.
 4. The last part focused on supported nanoparticles on a gold and SAM pre-covered gold support. Platinum NPs were wet-chemically synthesized by the polyol-approach allowing for a narrow size distribution of the particles without the use of protective ligands. Electrochemically measurements revealed a ripening process of the particles by a decrease in the electrochemical active area. Further, surface studies proved that the particles undergo a flattening process on the bare gold surface towards a monolayer monoatomic in height. A SAM was employed to decouple the properties of the particles and act as a blocking layer preventing the particles to flatten. It was demonstrated that the particles penetrate through the densely packed film creating a similar monolayer as on the bare gold substrate. This mechanism could be attributed to the strong platinum-gold interaction. The presented results gave an insight into the metallization of organic surfaces in which the self-assembled monolayer of alkanethiols represents an excellent model system to mimic an interface which is essential in molecular electronics. Since SAMs can be understood as the most elementary form of organic ultrathin film materials, it is important to understand the fundamental details of formation and stability.

Summarizing the presented results, engineering of novel nanostructures at the molecular and supramolecular level opened the way of new fabrication methods in materials design. Since the building blocks can exhibit a variety of functionalities at many length scales, they are prime candidates in nanodevice fabrications. Particularly in combination with the bottom-up approach, new strategies can be developed to arrange and self-assemble the building blocks with atomic precision at the solid-liquid interface. It could be shown how existing limitations in the fabrication process can be overcome, showing new strategies in the context of charge separation, transport properties or the enhancement of chemical reactions. With this insights, new systems can be developed which are low-cost while exhibiting high device efficiencies. In addition, a platform was created which allows to investigate systematically the micro- and macroscopic aspects of supported nanostructures in electrochemical experiments.

The results presented in this thesis show a route for future manufacturing methods in molecular engineering and layer-by-layer printing, quantum-domain plasmonic systems in nanoplasmonic devices and engineering of metal-SAM junctions.

References

- [1] Nazeeruddin, M. K.; Baranoff, E.; Grätzel, M. *Sol. Energy* **2011**, *85*, 1172–1178.
- [2] Lewis, N. S.; Nocera, D. G. *PNAS* **2006**, *103*, 15729–15735.
- [3] BP Statistical Review of World Energy June 2015, retrieved from <http://www.bp.com/statisticalreview.html>, February 2016.
- [4] World Energy Outlook 2015, retrieved from <http://www.worldenergyoutlook.org>, April 2016.
- [5] Crabtree, G. W.; Lewis, N. S. *Phys. Today* **2007**, *60*, 37–42.
- [6] Dimroth, F. et al. *Progr. Photovolt. Res. Appl.* **2014**, *22*, 277–282.
- [7] Sharenko, A.; Proctor, C. M.; van der Poll, T. S.; Henson, Z. B.; Nguyen, T. Q.; Bazan, G. C. *Adv. Mater.* **2013**, *25*, 4403–4406.
- [8] Tang, C. W. *Appl. Phys. Lett.* **1986**, *48*, 183–185.
- [9] Weil, T.; Vosch, T.; Hofkens, J.; Peneva, K.; Müllen, K. *Angew. Chem. Int. Ed.* **2010**, *49*, 9068–9093.
- [10] May, M. M.; Lewerenz, H. J.; Lackner, D.; Dimroth, F.; Hannappel, T. *Nat. Commun.* **2015**, *6*, 8286.
- [11] Khaselev, O.; Turner, J. A. *Science* **1998**, *280*, 425–427.
- [12] Fahrenbruch, A. L.; Bube, R. H. *Fundamentals of solar cells* **1983**, Academic Press, New York.
- [13] Boal, A. K.; Ilhan, F.; DeRouchy, J. E.; Thurn-Albrecht, T.; Russell, T. P.; Rotello, V. M. *Nature* **2000**, *404*, 746–748.
- [14] Whitesides, G. M.; Kriebel, J. K.; Mayers, B. T. *Nanoscale Assembly, Chapter: Self-Assembly and Nanostructured Materials, 217-239* **2005**, Springer US.
- [15] Tang, C. W. *Adv. Mater.* **1986**, *48*, 183–185.
- [16] Nesselberger, M.; Roefzaad, M.; Hamou, R. F.; Biedermann, P. U.; Schweinberger, F. F.; Kunz, S.; Schloegl, K.; Wiberg, G. K. H.; Ashton, S.; Heiz, U.; Mayrhofer, K. J. J.; Arenz, M. *Nat. Mater.* **2013**, *12*, 919–924.

- [17] Berr, M. J.; Schweinberger, F. F.; Döblinger, M.; Sanwald, K. E.; Wolff, C.; Breimeier, J.; Crampton, A. S.; Ridge, C. J.; Tschurl, M.; Heiz, U.; Jäckel, F.; Feldmann, J. *Nano Lett.* **2012**, *12*, 5903–5906.
- [18] Meier, J. C.; Galeano, C.; Katsounaros, I.; Witte, J.; Bongard, H. J.; Topalov, A. A.; Baldizzone, C.; Mezzavilla, S.; Schüth, F.; Mayrhofer, K. J. J. *Beilstein J. Nanotechnol.* **2014**, *5*, 44–67.
- [19] Silien, C.; Lahaye, D.; Caffio, M.; Schaub, R.; Champness, N. R.; Buck, M. *Langmuir* **2011**, *27*, 2567–2574.
- [20] Vericat, C.; Vela, M. E.; Benitez, G.; Carro, P.; Salvarezza, R. C. *Chem. Soc. Rev.* **2010**, *39*, 1805–1834.
- [21] Whiteside, G. M.; Mathias, J. P.; Seto, C. T. *Science* **1991**, *254*, 1312–1319.
- [22] Ball, P. *Nature* **1994**, *367*, 323–324.
- [23] Lehn, J. M. *PNAS* **2002**, *99*, 4763–4768.
- [24] Madueno, R.; Räsänen, M.; Silien, C.; Buck, M. *Nature* **2008**, *454*, 618–621.
- [25] Palma, C. A.; Bjork, J.; Bonini, M.; Dyer, M. S.; Llanes-Pallas, A.; Bonifazi, D.; Persson, M.; Samori, P. *J. Am. Chem. Soc.* **2009**, *131*, 13062–13071.
- [26] Li, B.; Tahara, K.; Adisoejoso, J.; Vanderlinden, W.; Mali, K. S.; De Gendt, S.; Tobe, Y.; De Feyter, S. *ACS Nano* **2013**, *7*, 10764–10722.
- [27] Schrader, I.; Warneke, J.; Neumann, S.; Grotheer, S.; Swane, A. A.; Kirkensgaard, J. J. K.; Arenz, M.; Kunz, S. *J. Phys. Chem. C* **2015**, *119*, 17655–17661.
- [28] Wang, Y.; J., R.; Deng, K.; Gui, L.; Tang, Y. *Chem. Mater* **2000**, *12*, 1622–1627.
- [29] Durst, J.; Simon, C.; Hasche, F.; Gasteiger, H. A. *J. Electrochem. Soc.* **2014**, *162*, F190–F203.
- [30] Gasteiger, H. A.; Panels, J. E.; Yan, S. G. *J. Power Sources* **2004**, *127*, 162–171.
- [31] Maillard, F.; Eikerling, M.; Cherstiouk, O. V.; Schreier, S.; Savinova, E.; Stimming, U. *Farad. Discuss.* **2004**, *125*-, 357–377.
- [32] Shao, M.; Peles, A.; Shoemaker, K. *Nano Lett.* **2011**, *11*, 3714–3719.

- [33] Cherevko, S.; Keeley, G. P.; Geiger, S.; Zeradjanin, A. R.; Hodnik, N.; Kulyk, N.; Mayrhofer, J. J. *ChemElectroChem* **2015**, *2*, 1471–1478.
- [34] Geiger, S.; Cherevko, S.; Mayrhofer, K. J. J. *Electrochim. Acta* **2015**, *179*, 24–31.
- [35] Wolfschmidt, H.; Weingarth, D.; Stimming, U. *ChemPhysChem* **2010**, *11*, 1533–1541.
- [36] Love, J. C.; Estroff, L. A.; Kriebel, J. K.; Nuzzo, R. G.; Whitesides, G. M. *Chem. Rev.* **2005**, *105*, 1103–1169.
- [37] Esplandiu, M. J.; Hagenström, H.; Kolb, D. M. *Langmuir* **2001**, *17*, 828–838.
- [38] Hoeben, F. J. M.; Jonkheijm, P.; Meijer, E. W.; Schenning, A. P. H. J. *Chem. Rev.* **2005**, *105*, 1491–1546.
- [39] Griessl, S.; Lackinger, M.; Edelwirth, M.; Hietschold, M.; Heckl, W. M. *Single Mol.* **2002**, *3*, 25–31.
- [40] Zhang, X.; Chen, T.; Chen, Q.; Wang, L.; Wan, L. J. *Phys. Chem. Chem. Phys.* **2009**, *11*, 7708–7712.
- [41] Teyssandier, J.; Battaglini, N.; Seydou, M.; Anquetin, G.; Diawara, B.; Sun, X.; Maurel, F.; Lang, P. *J. Phys. Chem. C* **2013**, *117*, 8737–8745.
- [42] Chen, Z.; Klyatskaya, S.; Urgel, J. I.; Eciija, D.; Fuhr, O.; Auwärter, W.; Barth, J. V.; Ruben, M. *Beilstein J. Nanotechnol.* **2015**, *6*, 327–335.
- [43] Lehn, J. M. *Science* **2002**, *295*, 2400–2403.
- [44] Ulman, A. *An Introduction to ultrathin organic films* **1991**, Academic Press, Boston.
- [45] Ulman, A. *Chem. Rev.* **1996**, *96*, 1533–1554.
- [46] Kudernac, T.; Mandal, A. K.; Huskens, J. *Langmuir* **2015**, *31*, 157–163.
- [47] Theobald, J. A.; Oxtoby, N. S.; Phillips, M. A.; Champness, N. R.; Beton, P. H. *Nature* **2003**, *424*, 1029–1031.
- [48] Tang, C. W.; Van Slyke, S. A. *Appl. Phys. Lett.* **1987**, *51*, 913–915.
- [49] Melnikov, S. M.; Yeow, E. K. L.; Uji-i, H.; Cotlet, M.; Müllen, K.; De Schryver, F. C.; Enderlein, J.; Hofkens, J. *J. Phys. Chem. B* **2007**, *111*, 708–719.

- [50] Nijhuis, C. A.; Reus, W. F.; Barber, J. R.; Whitesides, G. M. *J. Phys. Chem. C* **2012**, *116*, 14139–14150.
- [51] Dickey, M. D.; Chiechi, R. C.; Larsen, R. J.; Weiss, E. A.; Weitz, D. A.; Whitesides, G. M. *Adv. Funct. Mater.* **2008**, *18*, 1097–1104.
- [52] Cademartiri, L.; Thuo, M. M.; Nijhuis, C. A.; Reus, W. F.; Tricard, S.; Barber, J. R.; Sodhi, R. N. S.; Brodersen, P.; Kim, C.; Chiechi, R. C.; Whitesides, G. M. *J. Phys. Chem. C* **2012**, *116*, 10848–10860.
- [53] Bonanni, B.; Bizzarri, A. R.; Cannistraro, S. *J. Phys. Chem. B* **2006**, *110*, 14574–14580.
- [54] Huang, T. J.; Brough, B.; Ho, C. M.; Liu, Y.; Flood, A. H.; Bonvallet, P. A.; Tseng, H. R.; Stoddart, J. F.; Baller, M.; Magonov, S. *Appl. Phys. Lett.* **2004**, *85*, 5391–5393.
- [55] Takeuchi, S.; DiLuzio, W. R.; Weibel, D. B.; Whitesides, G. M. *Nano Lett.* **2005**, *5*, 1819–1823.
- [56] Shimizu, T.; Teranishi, T.; Hasegawa, S.; Miyake, M. *J. Phys. Chem. B* **2003**, *107*, 2719–2724.
- [57] Gates, B. D.; Xu, Q.; Stewart, M.; Ryan, D.; Willson, C. G.; Whitesides, G. M. *Chem. Rev.* **2005**, *105*, 1171–1196.
- [58] Costelle, L.; Räisänen, M.; Joyce, J. T.; Silien, C.; Johansson, L. S.; Campbell, J. M.; Räisänen, J. *J. Phys. Chem. C* **2012**, *116*, 22602–22607.
- [59] Nuzzo, R. G.; Allara, D. L. *J. Am. Chem. Soc.* **1983**, *105*, 4481–4483.
- [60] Malem, F.; Mandler, D. *Anal. Chem.* **1993**, *65*, 37–41.
- [61] Zhu, Z.; Daniel, T. A.; Maitani, M.; Cabarcos, O. M.; Allara, D. L.; Winograd, N. *J. Am. Chem. Soc.* **2006**, *128*, 13710–13719.
- [62] Vericat, C.; Vela, M. E.; Salvarezza, R. C. *Phys. Chem. Chem. Phys.* **2005**, *7*, 3258–3268.
- [63] Matei, D. G.; Muzik, H.; Götzhäuser, A.; Turchanin, A. *Langmuir* **2012**, *28*, 13905–13911.
- [64] Ciszek, J. W.; Tour, J. M. *Chem. Mater.* **2005**, *17*, 5684–5690.
- [65] Tour, J. M.; Jones, L. I.; Pearson, D. L.; Lamba, J. S.; Burgin, T. P.; Whitesides, G. M. *J. Am. Chem. Soc.* **1995**, *117*, 9529–9534.

- [66] Shen, C.; Buck, M.; Wilton-Ely, J. D. E. T.; Weidner, T.; Zharnikiv, M. *Langmuir* **2008**, *24*, 6609–6615.
- [67] Buck, M.; Eisert, F.; Fischer, J.; Grunze, M.; Träger, F. *Appl. Phys. A: Mater. Sci. Process* **1991**, *53*, 552–556.
- [68] Perini, L.; Durante, C.; Favaro, M.; Perazzolo, V.; Agnoli, S.; Schneider, O.; Granozzi, G.; Gennaro, A. *ACS Appl. Mater. Interfaces* **2015**, *7*, 1170–1179.
- [69] Ahluwalia, R. K.; Arisetty, S.; Wang, X.; Wang, X.; Subbaraman, R.; Ball, S. C.; De-Crane, S.; Myers, D. J. *J. Electrochem. Soc.* **2013**, *160*, F447–F455.
- [70] Shao-Horn, Y.; Sheng, W. C.; Chen, S.; Ferreira, P. J.; Holby, E. F.; Morgan, D. *Top. Catal.* **2007**, *46*, 285–305.
- [71] Avasarala, B.; Moore, R.; Haldar, P. *Electrochim. Acta* **2010**, *55*, 4765–4771.
- [72] Jung, D. R.; Czanderna, A. W. *Crit. Rev. Solid State* **1994**, *19*, 1–54.
- [73] Silien, C.; Buck, M. *J. Phys. Chem. C* **2008**, *112*, 3881–3890.
- [74] Duffe, S.; Grönhagen, N.; Patryarcha, L.; Sieben, B.; Yin, C.; von Issendorff, B.; Moseler, M.; Hóvel, H. *Nat. Nanotechnol.* **2010**, *5*, 335–339.
- [75] Chen, J.; Reed, M. A.; Rawlett, A. M.; Tour, J. M. *Science* **1999**, *286*, 1550–1552.
- [76] Binnig, G.; Rohrer, H. *Helv. Phys. Acta* **1982**, *55*, 726–735.
- [77] Binnig, G.; Rohrer, H.; Gerber, C.; Weibel, E. *Phys. Rev. Lett.* **1982**, *49*, 57–61.
- [78] Binnig, G.; Rohrer, H.; Gerber, C.; Weibel, E. *Phys. Rev. Lett.* **1983**, *50*, 120–123.
- [79] Song, J. P.; Pryds, N. H.; Gleibol, K.; Morch, K. A.; Thölen, A. R.; Christensen, L. N. *Rev. Sci. Instrum.* **1993**, *64*, 900–903.
- [80] Gewirth, A. A.; Craston, D. H.; Bard, A. J. *J. Electroanal. Chem.* **1989**, *261*, 477–482.
- [81] Melmed, A. J. *J. Vac. Sci. Technol. B* **1991**, *9*, 601–608.
- [82] Grafström, S.; Kowalski, J.; Neumann, R. *Springer Berlin Heidelberg* **1997**, *499*, 295–310.
- [83] Kretschmann, E. *Opt. Commun.* **1972**, *5*, 331–336.
- [84] Berndt, R.; Gimzewski, J. K. *Phys. Rev. B* **1993**, *48*, 4746–4754.

- [85] Gimzewski, J. K.; Sass, J. K.; Schlitter, R. R.; Schott, J. *Europhys. Lett.* **1989**, *8*, 435–440.
- [86] Berndt, R.; Gimzewski, J. K.; Johannson, P. *Phys. Rev. Lett.* **1991**, *67*, 3796–3799.
- [87] Nilius, N.; Ernst, N.; Freund, H.-J. *Phys. Rev. Lett.* **2000**, *84*, 3994–3997.
- [88] Möller, R.; Albrecht, U.; Boneberg, J.; Koslowski, B.; Leiderer, P.; Dransfeld, K. *J. Vac. Sci. Technol. B* **1991**, *9*, 506–509.
- [89] Gersten, J.; Nitzan, A. *J. Chem. Phys.* **1980**, *73*, 3023–3037.
- [90] Savage, K. J.; Hawkeye, M. M.; Esteban, R.; Borisov, A. G.; Aizpurua, J.; Baumberg, J. J. *Nature* **2012**, *491*, 574–577.
- [91] Stampelcoskie, K. G.; Kamat, P. V. *J. Phys. Chem. Lett.* **2015**, *6*, 1870–1875.
- [92] Lenner, M.; Racz, P.; Dombi, P.; Farkas, G.; Kroo, N. *Phys. Rev. B* **2011**, *83*, 205428–1–205428–5.
- [93] Kroo, N.; Thost, J. P.; Völcker, M.; Krieger, W.; Walther, W. *Europhys. Lett.* **1991**, *15*, 289–293.
- [94] Nienhaus, L.; Wieghold, S.; Nguyen, D.; Lyding, J. W.; Scott, G. E.; Gruebele, M. *ACS Nano* **2015**, *9*, 10563–10570.
- [95] Nienhaus, L.; Goings, J. J.; Nguyen, D.; Wieghold, S.; Lyding, J. W.; Li, X.; Gruebele, M. *J. Am. Soc. Soc.* **2015**, *137*, 14743–14750.
- [96] Frankel, G. S. *J. Electrochem. Soc.* **1998**, *145*, 2186–2198.
- [97] Das, D.; Veziroglu, T. N. *Int. J. Hydrogen Energ.* **2001**, *26*, 13–28.
- [98] Drake, B.; Sonnenfeld, R.; Schneir, J.; Hansma, P. K.; Slough, G.; Coleman, R. V. *Rev. Sci. Instrum.* **1986**, *57*, 441–445.
- [99] Sonnenfeld, R.; Hansma, P. K. *Science* **1986**, *232*, 211–213.
- [100] Itaya, K.; Tomita, E. *Surf. Sci.* **1988**, *201*, L507–L512.
- [101] Lustenberger, P.; Rohrer, H.; Christoph, R.; Siegenthaler, H. *J. Electroanal. Chem.* **1988**, *243*, 225–235.
- [102] Magnussen, O. M.; Hotlos, J.; Beitel, G.; Kolb, D. M.; Behm, R. J. *J. Vac. Sci. Technol. B* **1991**, *9*, 969–975.

- [103] Wilms, M.; Kruft, M.; Bermes, G.; Wandelt, K. *Rev. Sci. Instrum.* **1999**, *70*, 3641–3650.
- [104] Suggs, D. W.; Bard, A. J. *J. Phys. Chem.* **1995**, *99*, 8349–8355.
- [105] Wiechers, J.; Twomey, T.; Kolb, D. M.; Behm, R. J. *J. Electroanal. Chem.* **1988**, *248*, 451–460.
- [106] Zhang, B.; Wang, E. *Electrochem. Acta* **1994**, *39*, 103–106.
- [107] Zhu, L.; Claude-Montigny, B.; Gattrell, M. *Appl. Surf. Sci.* **2005**, *252*, 1833–1845.
- [108] Gentz, K.; Wandelt, K. *Chimia* **2012**, *66*, 44–51.
- [109] Schmickler, W. *Chem. Rev.* **1996**, *96*, 3177–3200.
- [110] Yagati, A. K.; Min, J.; Choi, J. W. *Modern Electrochemical Methods in Nano, Surface and Corrosion Science* **2014**,
- [111] Meier, J.; Friedrich, K. A.; Stimming, U. *Faraday Discuss.* **2002**, *121*, 365–372.
- [112] Hamann, C.; Hamnett, A.; Vielstich, W. *Electrochemistry* **1998**, Wiley–VCH, Weinheim.
- [113] Sun, S.; Zhang, G.; Geng, D.; Chen, Y.; Li, R.; Cai, M.; Sun, X. *Angew. Chem. Int. Ed.* **2011**, *50*, 422–426.
- [114] Jia, F.; Yu, C.; Ai, Z.; Zhang, L. *Chem. Mater.* **2007**, *19*, 3648–3653.
- [115] Biegler, T.; Rand, D.; Woods, R. *J. Electroanal. Chem. Interfacial Electrochem.* **1971**, *29*, 269–277.
- [116] Daikhin, L. I.; Kornyshev, A. A.; Urbakh, M. *Electrochim. Acta* **1997**, *42*, 2853–2860.
- [117] Reiner, A.; Kuhn, H.; Wokaun, A.; Scherer, G. G. *Z. Phys. Chem.* **2007**, *221*, 1319–1341.
- [118] Levich, V. G. *Acta Physiochim. URSS.* **1942**, *17*, 257–307.
- [119] Butler, J. A. V. *Trans. Faraday Soc.* **1932**, *28*, 379–382.
- [120] Erdey-Guez, T.; Volmer, M. *Z. Phys. Chem. A-Chem. T.* **1930**, *150A*, 201–213.
- [121] Khan, Y.; Al-Falih, H.; Zhang, Y.; Ng, T. K.; Ooi, B. S. *Rev. Sci. Instrum.* **2012**, *83*, 063708.1 – 063708.8.
- [122] Blunt, M. O.; Russell, J. C.; Gimenez-Lopez, M. D.; Taleb, N.; Lin, X.; Schröder, M.; Champness, N. R.; Beton, P. H. *Nat. Chem.* **2011**, *3*, 74–78.

- [123] Desiraju, G. R. *Acc. Chem. Res.* **2002**, *35*, 565–573.
- [124] Wilson, A. J. *Nat. Chem.* **2011**, *3*, 193–194.
- [125] Greef, T. F. A.; Meijer, E. W. *Nature* **2008**, *453*, 171–173.
- [126] Ciesielski, A.; Cadeddu, A.; Palma, C. A.; Gorczynski, A.; Patroniak, V.; Cecchini, M.; Samori, P. *Nanoscale* **2011**, *3*, 4125–4129.
- [127] Perdigo, L. M. A.; Fontes, G. N.; Rogers, B. L.; Oxtoby, N. S.; Goretzki, G.; Champness, N. R.; Beton, P. H. *Phys. Rev. B* **2007**, *76*, 245402–1–245402–6.
- [128] Kudernac, T.; Lei, S.; Elemans, J. A. A. W.; De Feyter, S. *Chem. Soc. Rev.* **2009**, *38*, 402–421.
- [129] Günes, S.; Neugebauer, H.; Sacriciftci, N. S. *Chem. Rev.* **2007**, *107*, 1324–1338.
- [130] Yu, J.; Liu, G.; Sumant, A. V.; Goyal, V.; Balandin, A. A. *Nano Lett.* **2012**, *12*, 1603–1608.
- [131] Tollin, G.; Kearns, D. R.; Calvin, M. *J. Chem. Phys.* **1960**, *32*, 1013–1019.
- [132] Burroughes, J. H.; Bradley, D. D. C.; Brown, A. R.; Marks, R. N.; Mackay, K.; Friend, R. H.; Burns, P. L.; Holmes, A. B. *Nature* **1990**, *347*, 539–541.
- [133] Hebner, T. R.; Wu, C. C.; Marcy, D.; Lu, M. H.; Sturm, J. C. *Appl. Phys. Lett.* **1998**, *72*, 519–521.
- [134] Hali, M.; Hirsch, A. *Adv. Mat.* **2011**, *23*, 2689–2695.
- [135] Yu, K.; Groom, D. J.; Wang, X.; Yang, Z.; Gummalla, M.; Ball, S. C.; Myers, D. J.; Ferreira, P. J. *Chem. Mater.* **2014**, *26*, 5540–5548.
- [136] Dreesen, L.; Volcke, C.; Sartenaer, Y.; Peremans, A.; Thiry, P. A.; Humbert, C.; Grugier, J.; Marchand-Brynaert, J. *Surf. Sci.* **2006**, *600*, 4052–4057.
- [137] Cahill, D. G.; Hamers, R. J. *Phys. Rev. B* **1991**, *44*, 1387–1390.
- [138] Pedarnig, J. D.; Specht, M.; M., H. W.; Hänsch, T. W. *Appl. Phys. A* **1992**, *55*, 476–477.
- [139] Grafström, S.; Kowalski, J.; Neumann, R.; Probst, O.; Wörtge, M. *J. Vac. Sci. Technol. B* **1991**, *9*, 568–572.
- [140] Nienhaus, L.; Scott, G. E.; Haasch, R. T.; Wieghold, S.; Lyding, J. W.; Gruebele, M. *J. Phys. Chem. C* **2014**, *118*, 13196–13202.

List of Figures

1	Overview of the used systems in this work. A) supramolecular network formation on different carbon supports, B) self-assembled monolayer formation on gold and its use as support for platinum nanoparticles and C) transparent thin gold films as support for platinum clusters. Image: F. F. Schweinberger.	15
2	Roadmap of the thesis. The respective sections are listed on the left. The topic is shown in the right column.	17
3	Supramolecular bicomponent network formation of melamine and NTCDI on HOPG. Scale bars: left top 3 nm, right top 15 nm, left bottom 30 nm. Right bottom: molecular model, blue: melamine, grey: NTCDI.	20
4	Chemical structures of peryleneimide and its derivatives and corresponding absorption spectra. Reprinted with permission from T. Weil, T. Vosch, J. Hofkens, K. Peneva, K. Müllen, <i>Angew. Chem. Int. Ed.</i> 2010, 49, 9068-9093, Copyright © 2010 WILEY-VCH Verlag GmbH & Co. KGaA, Weinheim.	21
5	STM images of N-dodecyl thiocyanate on Au(111) (15 mM ethanol, 60 °C, 12h). a) $(\sqrt{3} \times \sqrt{3})R30$ structure, b) $c(4 \times 2)$ superlattice structure with the packing structures of a) and b) shown in c) and d) respectively, $I_t = 15$ pA, $U_t = 0.8$ V, scale bars 2 nm.	24
6	Representative STM images (100x100) nm of N-dodecyl thiocyanate (purified) under different preparation conditions. a) 15 mM, ethanol, RT, 12h, b) 15 mM ethanol, 60 °C, 12h, c) 15 mM ethanol, 60 °C, 72h, d) 5 mM ethanol, 60 °C, 12h, e) 15 mM ethanol, 75 °C, 60h, f) 5 mM ethanol, 60 °C, 72h, g) 1 mM ethanol, 60 °C, 12h, h) 15 mM isopropanol, 60 °C, 12h, i) 5 mM DMSO, 60 °C, 12h, $I_t = 15$ pA, $U_t = 0.8$ V.	25
7	Different degradation mechanisms for supported platinum nanoparticles on a carbon support. Reprinted with permission from J. C. Meier, C. Galeano, I. Katsounaros, J. Witte, H. J. Bongard, A. A. Topalov, C. Baldizzone, S. Mezzavilla, F. Schüth, K. J. J. Mayrhofer, <i>Beilstein J. Nanotechnol.</i> 2014, 5, 44-67, Copyright © 2014 Meier et al.; Beilstein-Institut.	27
8	Left: schematic of the STM principle. Right: energy level diagram for a positively biased sample compared to the tip allowing electrons to tunnel from the tip to the sample.	29
9	Schematic of the Kretschmann configuration used in SMA-STM studies.	31

10	Schematic overview of an ECSTM setup.	35
11	Scanning principle of an ECSTM. a) STM image taken before and after a CV. b) stepwise increase of the electrochemical potential while scanning at a fixed bias potential. The images are recorded at a WE potential of 0.0 V, 0.1 V, 0.2 V and 0.3 V. All potentials are measured vs. RHE.	36
12	Cyclic voltammetry potential waveform. Adapted from Ref. [112].	37
13	Setup of a RDE with potentiostat and electrodes.	39
14	Left: schematic of the original STM setup. Reprinted with permission from M. Wilms, M. Kruft, G. Bermes, K. Wandelt, Rev. Sci. Instrum. 1999, 70, 3641-3650. Copyright © 1999 American Institute of Physics. Right top: image of the STM-head, right bottom: image of the STM-base.	41
15	Left: tip adjusting device for STM tips. Right top: top view of the original electrochemical cell with cross section of the cell. Reprinted with permission from M. Wilms, M. Kruft, G. Bermes, K. Wandelt, Rev. Sci. Instrum. 1999, 70, 3641-3650. Copyright © 1999 American Institute of Physics.	42
16	Modified STM setup with an external FEMTO [®] amplifier (1) and external RHE connected via a Luggin capillary to the electrochemical cell (2).	43
17	SEM images of STM tips taken at an acceleration voltage of 15 kV. Left: etched tungsten tip, middle: etched Pt/Ir wire and right: mechanically cut Pt/Ir tip. . .	44
18	Left: setup for etching W tips, right: close-up of the W tip while etching in a lamella.	44
19	Left: Pt/Ir tip after the first stage of etching, right: final etched tip.	45
20	Etched tungsten tip coated with glue.	46
21	RHE electrode.	46
22	Optical setup for photochemical measurements.	47
23	Left: tungsten tip with a gallium droplet, middle: STM under 710 nm and right: 520 nm illumination.	48
24	Different methods employed to determine the contact area of a Ga droplet. Top left: SEM image of a HOPG surface coated with methyl methacrylate (MMA). Top right: MMA coated HOPG surface under a USB-microscope. In both cases, the tip was approached to the surface and an imprint of the tip in the MMA was tried. Bottom left: SEM image of a tungsten tip with a Ga droplet which has contacted the surface. Bottom right: deflection mirror showing the surface and tip from underneath.	48

25	SMA-STM setup. Left: laser setup with mirrors and chopper. Middle: UHV STM chamber. Right: illuminated sample with prism.	49
26	RDE setup with gas change system and flow controller.	50
27	Parameter file for coarse approach.	98
28	Left: scanner piezo voltage, right: sawtooth voltage applied to the base piezos. .	100
29	Left: FFT spectra of IVP-200 and right: IVP-300 recorded with the spectrum analyzer of the XPMPro software.	100
30	Parameter file for STS measurements.	101

List of Tables

1	Piezo calibration values.	98
2	DAC output for coarse approach connected to an oscilloscope. The respective voltages for X-offset are shown.	102
3	DAC output for coarse approach connected to an oscilloscope. The respective voltages for approach, retract, fast in and fast out are shown for all piezo motions.	102

Acknowledgments

First of all I would like to thank PD Dr. Friedrich Esch for giving me the opportunity to do my research and for several fruitful discussions. Further, I want to acknowledge Prof. Ueli Heiz for his support during my whole thesis project.

Especially, I would like to thank Juan Li and Dr. Carlos-Andres Palma for the nice working atmosphere and cooperation during my whole PhD. Thank you for the support and guidance especially at the beginning of the project.

I would like to thank Dr. Martino Saracino for helping me building the STM setup with all the challenges and technical setbacks. In addition, I would like to thank Fabian Knoller for always helping out with STM equipment.

Especially, I would like to thank Dr. Florian Schweinberger for his advices and help.

I want to thank the Chair of the Technische Elektrochemie of Prof. Dr. Hubert Gasteiger and in particular, Armin Siebel for helping me with several electrochemical problems and discussions.

I would like to thank the electronics and mechanics workshop for their support in building up novel setups.

Furthermore, I appreciate all Bachelor/Master students and Forschungspraktikanten, Max, Philipp, Josua, Tarik, Matthias, David, Daniel and Steffen for their help and cooperation in the lab.

I want to acknowledge the Nanosystems Initiative Munich (NIM) for supporting my research stays abroad at the University of Illinois at Urbana-Champaign, USA where I could build up successful cooperations. Especially, I want to thank Prof. Dr. Martin Gruebele who gave me the chance to work in his lab and for his support in data evaluation and critical reading of several drafts.

In particular, I would like to thank Dr. Lea Nienhaus for always supporting me and the nice atmosphere and housing situation abroad. Especially, long car rides and (legend)ary nights gave us the opportunity to plan unique research projects resulting in several publications.

Last, I want to thank my family and friends for their support during my studies and PhD thesis.

List of publications

1. S. Wieghold, L. Nienhaus, A. Siebel, M. Krause, P. Wand, M. Gruebele, U. Heiz, F. Esch, Mechanistic Details on the Flattening Mechanism of Supported Platinum Nanoparticles on Gold and Thiol-Terminated Self-Assembled Monolayers, **2016**, in preparation.
2. S. Wieghold, L. Nienhaus, F. L. Knoller, F. F. Schweinberger, J. W. Lyding, U. Heiz, M. Gruebele, F. Esch, Plasmonic Activation of 1 nm Platinum Clusters for Photocatalysis, **2016**, submitted.
3. S. Wieghold, J. Li, M. Krause, Y. Avlasevich, C. Li, P. Simon, J. A. Garrido, U. Heiz, P. Samori, K. Müllen, F. Esch, J. V. Barth, C. A. Palma, Photoresponse of Supramolecular Self-assembled Networks on Graphene-Diamond Interfaces, *Nat. Commun.*, **2016**, 7, 10700.
4. L. Nienhaus, J. J. Goings, D. Nguyen, S. Wieghold, J. W. Lyding, X. Li, M. Gruebele, Imaging Electronic Excitation of Quantum Dots: Experiment and Electronic Structure Theory, *J. Am. Chem. Soc.*, **2015**, 137, 14743-14750.
5. L. Nienhaus, S. Wieghold, D. Nguyen, J. W. Lyding, G. E. Scott, M. Gruebele, Optoelectronic Switching of a Carbon Nanotube Chiral Junction Images with Nanometer Spatial Resolution, *ACS Nano*, **2015**, 9, 10563-10570.
6. J. Li, S. Wieghold, M. A. Öner, P. Simon, M. V. Hauf, E. Margapoti, J. A. Garrido, F. Esch, C. A. Palma, J. V. Barth, Three-Dimensional Bicomponent Supramolecular Nanoporous Self-Assembly on a Hybrid All-Carbon Atomically Flat and Transparent Platform, *Nano Lett.*, **2014**, 14, 4486-4492.
7. L. Nienhaus, G. E. Scott, R. T. Haasch, S. Wieghold, J. W. Lyding, M. Gruebele, Transparent Metal Films for Detection of Single-Molecule Optical Absorption by Scanning Tunneling Microscopy, *J. Phys. Chem. C*, **2014**, 118, 13196-13202.

All listed publications resulted from my PhD work at the Chair of Physical Chemistry at TUM. Publications 1-3 and 6 are presented in this cumulative doctoral thesis and are either attached in the results section (publication 3 and 6) or in Appendix B (publication 1, 2).

Publications 4, 5 and 7 resulted from my cooperation with the Gruebele group at the University of Illinois at Urbana-Champaign, IL, USA. In these paper, a method was developed which allowed to study single molecule absorption by STM with atomic resolution. These publications enabled to study supported clusters for photocatalysis (publication 2).

Appendix A

RHK Parameters

The D/A output channel on the rear panel, which is used to drive the coarse approach, must be connected with a BNC cable to the input on the rear panel of the SPM100 (External controls/Inertial input to Output A (D/A1)). Further, a BNC cable must be used to connect Bias#1 and Output A (D/A2). The configuration of the piezos used in this setup is set according to RHK Manual (SPM 1000, Revision 8.5) to configuration H. Here, all scan signals (X, Y and Z) and offset signals (X and Y) are applied to the scanner piezo. The signals of the coarse approach are applied to the 3 base piezos. Additionally, the Z-offset signal is applied to the scanner piezo.

In general, two preamplifiers are implemented in the scan head. They belong to the IVP line of high performance current amplifiers designed for low noise STM experiments (RHK Technology Inc.). In this setup, an IVP-200 and IVP-300 current amplifier are used. The IVP-200 outputs -100 mV per 1 nA of input current. The maximum input current is 100 nA which will generate a -10 V output (gain 10^8). The IVP-300 outputs -1 V per 1 nA of input current. The maximum input current is 10 nA which will generate a -10 V output (gain 10^9). In addition, a programmable preamplifier is in line after the first amplification stage (IVP-PGA) with a unity gain of x1, x10 and x100 and a bandwidth ranging from 500 Hz to 150 kHz. The RHK control electronic is configured that a positive tunneling current results from a positive bias. Since both IVP first stage preamplifiers (200 and 300) are inverting amplifiers, the PGA has to be set as an inverting amplifier.

In the modified setup, two FEMTO[®] preamplifier are used, LCA-S and DLPCA-200. They are connected to the cubus and the tunneling output is directly connected with a BNC cable to the rear panel of the SPM100 to the input feedback select. The LCA-S is a low noise current amplifier with a gain up to 10^{13} V/A and a bandwidth of 400 kHz. It has an input noise down to 180 aA/sqrtHz. The DLPCA-200 has a variable transimpedance gain ranging from 10^3 to 10^{11} V/A with a bandwidth up to 500 kHz. Its switchable AC/DC coupling and 10 Hz low pass filter can be used to adapt the amplifier to varying scanning conditions. The input noise is down to 4.3 fA/sqrtHz with a rise time down to 700 ns.

Piezo Calibration

The piezo calibration parameters for the X, Y and Z directions are stored in a RHK file which is initialized when the SPM100 controller is switched on (Tab. 1). After initializing, the out-of-range LED on the front panel of the SPM100 must be on. The main menu is opened by clicking on the *NAV* (navigation) and *Acq* (real time Acquisition) button. Under the tab *Acq/settings/configure hardware settings/gain* the proper gain has to be inserted in the *pre-amp gain* (volt/current) tab depending on the used preamplifier. In the same window under *head/scanner* the calibration factors for the piezo voltages are displayed. To calibrate the piezos, a known surface is imaged and the respective calibration factors have to be calculated.

Table 1: Piezo calibration values.

Piezo	Calibration factor
X motion/piezo volt	11.5
Y motion/piezo volt	11.5
Z linear motion	1
X,Y offsets	11.5
Z analog	2

Approach parameters

For approaching the tip to the sample, the parameters can be set in the *NAV* window. Under *NAV/tip approach/motor setup* the approach parameters can be entered. The used parameters are shown in Fig. 27. The beetle type STM uses a stick and slip mechanism, also called kinetic

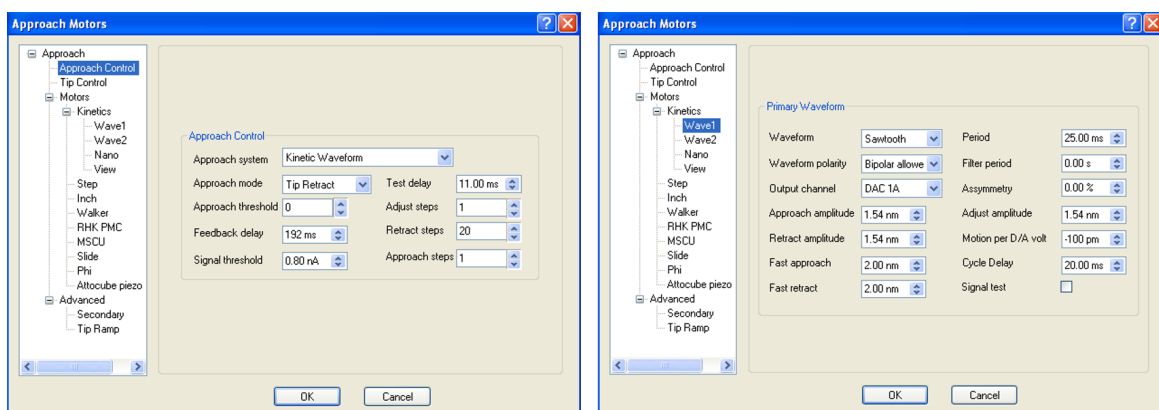


Figure 27: Parameter file for coarse approach.

approach system for the coarse approach. By slowly expanding and then quickly contracting the piezo, a translation along the axes can be produced. For this approach mode, the tip retract mode is chosen. The scanner piezo is retracted, the base piezos make a motion cycle followed by

a fully extension of the scanner piezo to allow the tip to approach the sample with the feedback loop active. The software monitors the Z signal to determine if the tip can be stabilized above the threshold value (current setpoint). If this value is not reached, the piezo retracts followed by the next motion cycle. Each cycle needs about 1 s depending on the feedback loops proportional and integral (PI) parameters (gain and time constant on the front panel of the SPM100). The approach threshold can be set to values between $\pm 100\%$. 100% means the approach stops and the scanner piezo is fully retracted, whereas a value of -100% indicates that the piezo is fully extended. The value of 0%, which is chosen in this setup, means that the tip approaches until it is just past the midpoint of the feedback range. The feedback delay is set to 192 ms (it is the amount of time the signal remained above the threshold and if so, the approach stopped assuming the tip is in range). The signal threshold should be chosen to be always below the setpoint knob or the approach will continue until the tip is fully retracted and then a crash occurred. The test delay is only relevant when signal test or feedback detect modes are chosen as approach modes. In the next tabs *adjust steps*, *retract steps* and *approach steps* the number of steps can be set which are made when the piezo is in range. Adjust steps is equal to the number of steps that will be made by clicking on the “+” and “-” button in the NAV window. For the kinetics of the primary waveform a normal sawtooth voltage is applied to drive the base piezo tubes. The approach amplitude in this setup is set to 1.54 nm. It is the distance to move each step while in automatic approach mode. The retract amplitude is only used when the retract button in the NAV window is used. *Fast approach/fast retract* sets the value which will be applied to the piezos when the *fast in* or *fast out* buttons are pressed in the NAV window. The amount of time in which one cycle should be completed is entered in under *period*. The *filter period* is 0 s which means that no filtering is applied and the waveform will be generated at the maximum possible rate of 250 kHz of the DT3016 board. A symmetric sawtooth is generated by using a value of 0 in the *asymmetry* box. The *adjust amplitude* sets the distance moved each time a button is pressed in the NAV window. The *motion per D/A volt* determines how much volts are applied to achieve the entered value. The *cycle delay* is only used when fast motions are taking place and determines the time between each coarse step. In Fig. 28 the voltage displayed on the oscilloscope can be seen if proper values for the coarse approach and PI controller are set.

Spectrum analyzer

In the *Acq* window, the *FFT* (spectrum analyzer) can be used to test the preamplifiers. Fig. 29 shows the FFT spectra. If the preamplifiers work properly, a low signal should be present in the



Figure 28: Left: scanner piezo voltage, right: sawtooth voltage applied to the base piezos.

range between 4 Hz to 200 Hz (IVP-200 < 5 fA/sqrtHz, IVP-300 < 11 fA/sqrtHz).

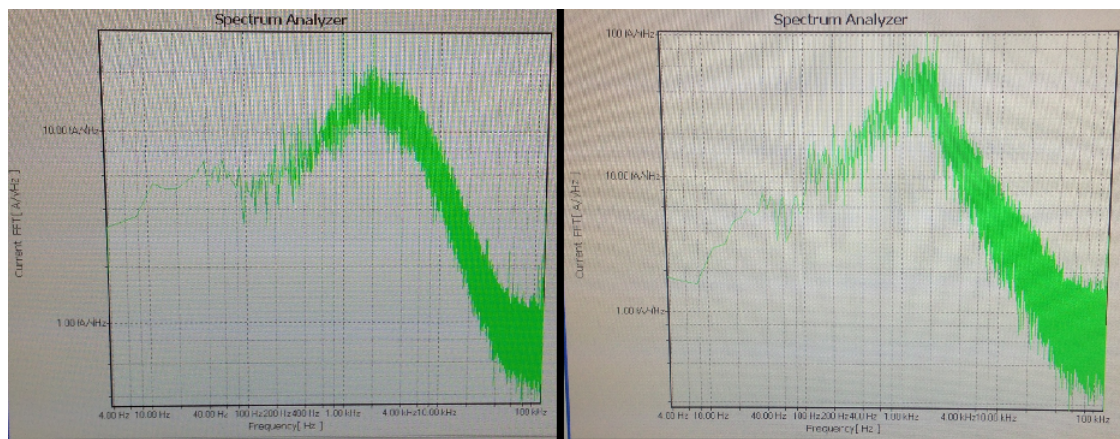


Figure 29: Left: FFT spectra of IVP-200 and right: IVP-300 recorded with the spectrum analyzer of the XPMPro software.

STS parameters

For STS measurements, the settings can be modified under the *Acq/settings/spectroscopy* tab (Fig. 30). Under the *control* tab, the parameters for measuring current - distance (I-z) and current - voltage (I-V) curves can be set. The feedback should be off during the voltage sweep. *Samples/point* is used to make an average of measurements for each voltage step. In addition, the *setup rate*, *spectrum delay*, *sweep rate* and *sample delay* can be set in this tab. The setup rate determines the rate to change the voltage from zero to the first value and from the final value back to zero. The spectrum delay is the delay to wait after the output reaches the initial value before reading the first point. The sweep rate is the rate the voltage is changed from the output value to the next voltage value. The pre-sample delay is the amount of time to wait after each voltage step is reached.

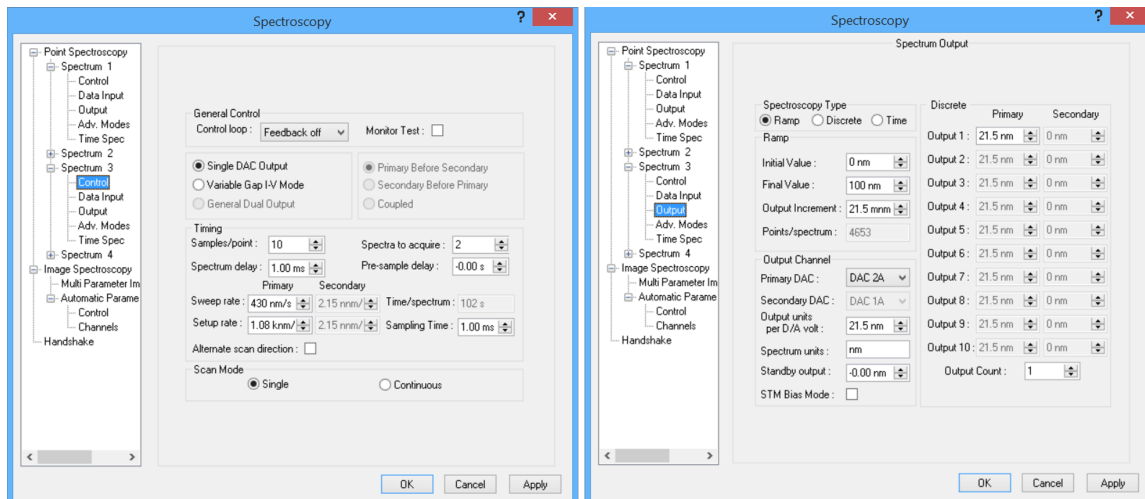


Figure 30: Parameter file for STS measurements.

Troubleshooting RHK

The HV boards generate output voltages of max. ± 215 V. Board #1: XY Scan Driver, Board #2: XY Offset Driver, Board #3: Z Driver. Each board is placed into slot 2 (Offset driver) with the three jumper set to S1: 2-3, S2: 1-2, S3: 1-2 in which the X and Y offset knobs are connected to the $\pm X$ and $\pm Y$ outputs. The $+X$ and $+Y$ outputs should produce a voltage ranging from -215 V to $+215$ V; the $-X$ and $-Y$ outputs from $+215$ V to -215 V. The Z driver has only two HV amplifiers and a signal can only be detected on the positive outputs of X and Y. The $-X/+X$, $-Y/+Y$ scan signals and Z scan signal are used for the approach as well as for fast movements. There are 2 possible configurations for the approach:

1. $-X/+X/-Y/+Y$ scan signals are used for the approach by applying a signal to the 4 ring electrodes of the scanner piezo (if jumper S1 on board #1 is set to 1-2).
2. If the jumper on board #1 is set to 2-3, the cylindrical electrode of the scanner piezo is used for the approach by applying only the Z scan signal to the electrode.

The offset signals of $-X/+X/-Y/+Y$ are applied to the base piezos for fast movements and approach (Tab. 3). All other signals should show a signal of $+215$ V when no movement takes place; -215 V will be applied to the piezos when a fast movement takes place (Tab. 4).

Table 2: DAC output for coarse approach connected to an oscilloscope. The respective voltages for X-offset are shown.

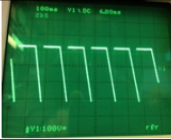
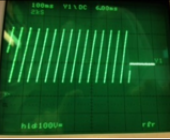
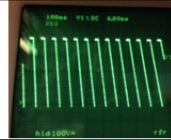


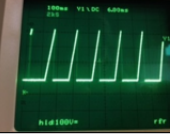
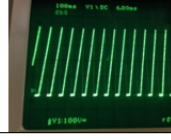
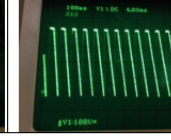
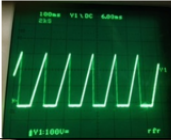
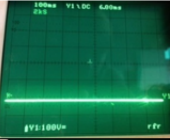
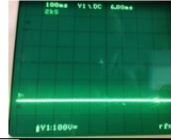
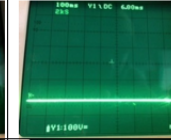


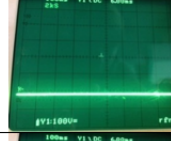









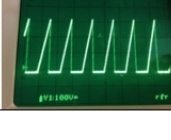


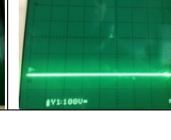
Channel/ x10 Preamp. disconnected	Approach	Retract	Fast In	Fast Out
-X offset				
+X offset				

Table 3: DAC output for coarse approach connected to an oscilloscope. The respective voltages for approach, retract, fast in and fast out are shown for all piezo motions.

Channel/ x10 Preamp. disconnected	Approach	Retract	Fast In	Fast Out
-X scan				
+X scan				
-Y scan				
+Y scan				
Z scan				

Appendix B

Unpublished Results

Mechanistic Details on the Flattening Mechanisms of Supported Platinum Nanoparticles on Gold and Thiol-Terminated Self-Assembled Monolayers

Platinum is the most important electrocatalyst material employed in fuel cells towards alternative energy generation sources achieving high power-conversion efficiencies [29]. However, there is an arising demand to stabilize these particles on the surface in order to prevent degradation mechanisms including platinum dissolution, Ostwald ripening, agglomeration, particle detachment or carbon corrosion [18, 135]. This degradation implies a reduction of the ECSA and thus, a loss of chemical activity. To gain more insights into the mechanistic details, SAMs are prime candidates to minimize the adhesion between the substrate and the metal NP [19] while tailoring the interfacial properties of the interface [58]. Especially, n-alkanethiols either functionalized with thiols [36, 136] or thiocyanates [64, 73] as headgroup bear the potential to form ordered structures on gold supports. Since the discovery of SAMs in 1983 [59], they are one of the most prominent approaches in bottom-up fabrication technologies [20]. SAMs represent an optimal test platform and can be described as well-defined and densely packed spacer layer.

The manuscript titled 'Mechanistic details on the flattening mechanisms of supported platinum nanoparticles on gold and thiol-terminated self-assembled monolayers' is presented in this section. A detailed molecular-level understanding on the stability of supported platinum NPs on a bare gold and thiol-precured gold substrate is demonstrated. Unprotected platinum NPs are synthesized by the polyol approach. First the size distribution is investigated by means of transmission electron microscope (TEM). The activity of the supported particles on a bare and SAM covered gold support is measured using cyclic voltammetry. It is observed that the ECSA decrease in each cycle and thus, the particles have to undergo a flattening process. In the case of platinum on gold, two rate constants could be determined. To distinguish this mechanism in more detail, the particles are imaged by STM at ambient conditions. Here, a flattening of the particles on the bare gold support is observed resulting in an overlayer which is monoatomic in height. The same effect is also observed on the thiol-covered gold support. Finally, Monte Carlo simulations are performed to validate the results.

Mechanistic Details on the Flattening Mechanism of Supported Platinum Nanoparticles on Gold and Thiol-Terminated Self-Assembled Monolayers

S. Wieghold^{§,#}, L. Nienhaus^{&,#}, A. Siebel^{¶,#}, M. Krause^{§,#}, P. Wand^{§,#}, M. Gruebele^{&,#,§}, U. Heiz^{§,#}, F. Esch^{§,#}

[§]Physical Chemistry, [¶]Chair of Electrochemistry and [#]Catalysis Research Center, Chemistry Department, Technische Universität München, Lichtenbergstr. 4 and Ernst-Otto-Fischer-Str. 1, 85748 Garching, Germany

[&]Beckman Institute for Advanced Science and Technology, [†]Department of Chemistry and [§]Department of Physics, University of Illinois, Urbane, Illinois 61801

KEYWORDS. platinum nanoparticles, polyol approach, flattening, gold, self-assembled monolayers, ligand-stabilized particles, scanning tunneling microscopy

ABSTRACT

The recent spotlight on supported nanoparticles has attracted attention in the field of fuel cell technology. Supported nanoparticles can be used as model catalysts to gain a fundamental understanding of the electrocatalytic properties at the interface. Here, especially the preparation of unprotected nanoparticles in alkaline ethylene glycol is a powerful approach allowing for the synthesis of stable particles with a narrow size distribution in the subnanometer regime. In this article, platinum nanoparticles are investigated on a bare and on a dodecanethiol covered Au(111) surface. Scanning tunneling microscopy is combined with electrochemical methods in order to study the degradation mechanism of the particles. A loss in the electrochemical active surface area (ECSA) of supported particles on Au(111) is found during potential cycling and could be attributed to a two-step degradation mechanism of the particles. A single rate is obtained for the change in ECSA for particles on a SAM covered gold support. To validate the underlying degradation processes, a kinetic Monte Carlo model was developed.

INTRODUCTION

Platinum is one of the most important materials in proton exchange membrane fuel cells (PEM-FCs) due its remarkable electrocatalytic activity.^{1, 2} For catalyzing the important hydrogen oxidation and evolution reactions (HOR/HER), only small amounts of platinum are required.^{1, 2} In operation a loss of active surface area is observed, it can be related to a change in the morphology of the nanoparticles³ undergoing different degradation mechanisms.^{4, 5, 6} Thus, during the last years, several attempts have been made to characterize and study the influence of particle size,^{7, 8} dissolution,^{9, 10} stability^{11, 12} and supporting layer^{13, 14} on their catalytic performance. Since the electrocatalytic processes take place at the surface of the particles, the activity depends strongly on their specific surface area. Hence, there is a great interest in studying the underlying processes at the nanoscale which occur at the metal-support interface. Unprotected nanoparticles (NP) are readily prepared via the polyol approach and bear the potential for the preparation of particles in the nanometer regime.^{15, 16} Here, the particles are stabilized by a weakly adsorbed ethylene glycol (EG) sub-layer rather than by strongly binding agents like thiols¹⁶ that would block the reactive sites. With this preparation approach, particles with a narrow size-distribution can be synthesized.¹⁷ This initial size-distribution is prevailing for the understanding of degradation mechanisms during operation in fuel cells since the performance can be linked to the structure and composition of the catalyst material.¹² Using these unprotected particles, detailed investigations e.g. support or coverage effects as well as particle-support interactions at the interface can be made in a systematic manner.^{15, 18} Besides the nanoparticles itself, a suitable support with a well-defined and extended surface is mandatory. Since the support plays a crucial role, an accurate reference support system is required which is electrochemically inactive over the potential range of interest.¹³ In the past, Au single-crystals which exhibit the aforementioned criteria, have been employed to study ultra-low coverages ($10^{-5} - 10^{-4}$ ML) of Pt¹⁹ and Pd²⁰ ad-atoms in the context of enhancing HOR/HER. It is observed, that the ad-atoms incorporate into the gold lattice. Thus, they represent additional active sites for the reactant, dissolved molecular hydrogen for HOR/HER. Further, it was reported that an increased step²¹ and defect²² density on Au surfaces increased the catalytic activity of supported Pt catalysts. In addition, gold supports bear the potential for surface modifications. Here, the modification of the simple Au support by organic layers has gained much interest. By using a self-assembled monolayer (SAM), the properties of the nanoparticles and the support can be decoupled enabling a detailed investigation of the interface. In this context, alkanethiols are mainly used on gold supports²³ forming a well-packed, densely and ordered overlayer.²⁴ They can be employed to minimize the

adhesion between the particle and the substrate, and thus are excellent model systems. While it is known that nanoparticles made of Cu, Ag and Au penetrate through an alkanethiol SAM, the involved mechanistic details e.g. single particle penetration, particle decay or rearrangement of the single atom particles after penetration are poorly understood.^{25, 26} Further, the differences of the penetration mechanism between wet-chemically synthesized²⁷ and UHV clusters²⁸ are still unknown. In this article, PtNP are synthesized by the polyol approach and analyzed by scanning transmission electron microscope (STEM). When supported on a bare gold single crystal, a change in the active particle surface area (ECSA) is observed by cyclic voltammetry (CV). Scanning tunneling microscopy (STM) is used to investigate the underlying processes in more detail. A two-step degradation mechanism of the PtNP on the bare gold support is observed. Further, to decouple the particle properties from the support, two strategies are presented: a SAM on a gold support and ligand-functionalized nanoparticles supported on a gold substrate. In contrast to the bare gold surface, detailed STM studies reveal particle penetration through the SAM followed by a reordering of single Pt atoms on the support. Ligand-functionalized particles show a stable behavior in STM measurements however, they are inactive towards electrochemical reactions. The presented experimental results are confirmed by Monte Carlo simulations.

EXPERIMENTAL SECTION

SAM preparation. 1-Dodecanethiol ($\geq 98\%$, Sigma-Aldrich) was used as received. For the thiol self-assembly, a freshly flame-annealed single crystal (Au(111), MaTeck GmbH) was immersed in a 0.1 mM isopropanol solution of 1-dodecanethiol for 12 h at room temperature. Afterwards, the sample was rinsed in ethanol and dried in an argon stream. For the aromatic SAM, the gold single crystal was immersed in a 1 mM solution of thiophenol ($\geq 99\%$, Sigma-Aldrich) in isopropanol for 12 h or respectively in a 2 μM solution of biphenylthiol (97%, Sigma-Aldrich) in DMF (99.8%, Sigma-Aldrich) for 3 days.

Nanoparticle synthesis. For the platinum nanoparticle synthesis the procedure repeated by Kunz *et al.*¹⁷ was used: 0.25 g chloroplatinic acid hexahydrate (99.9%, Sigma-Aldrich) were dissolved in 25 mL ethylene glycol (EG, $>99\%$, Alfa Aesar). Afterwards, 25 mL of a 0.5 M NaOH solution in EG was added and stirred under reflux at 150 °C until the solution was homogenized. After 5 min the formation of nanoparticles occurred which is indicated by a change in color of the solution from yellow to black. For a complete reduction of the Pt precursor, the solution was kept at 150 °C for 2h, followed by a cooling to ambient temperatures. 50 mL of 1 M HCl were added to this solution to precipitate the particles. This mixture was twice centrifuged, decanted

and washed with 1 M HCl in an ultrasonic bath prior to redispersion in 30 mL cyclohexanone or ethylene glycol. For the functionalization of the platinum nanoparticles, a 12 mmol solution of the thiol molecules in 50 mL toluene was added to the EG solution of the nanoparticles and stirred. After a complete phase transfer, the phases were separated and the platinum containing phase was washed three times with 20 mL water. To precipitate the particles in the organic phase, the toluene solution was concentrated to ca. 3 mL followed by adding 50 mL of ethanol. The precipitated mixture was centrifuged, washed three times with ethanol/water (ration 2:1) and dried.

Prior to deposition on the support, the quality of the particles was verified using IR spectroscopy (for the unprotected particles, SI1). For sample preparation, a diluted solution containing the nanoparticles was sonicated for 10 min and drop-casted (5 μ L) on the TEM grid (2 nm carbon support on 300 mesh copper grids – Surface Services) and the respective gold surface. Afterwards, the sample was dried in an argon stream.

STM measurements. STM measurements were performed in a home-built Besocke beetle type STM described in detail elsewhere.²⁹ The scanning tips were prepared by mechanically cutting a Pt/Ir wire (80:20, Goodfellow, UK). All images were taken in constant current mode and are shown without further processing except flattening to remove the tilting effect of the substrate plane. The respective tunneling current and bias are given in the text. Electrochemical measurements. Cyclic voltammetry measurements were performed in a three-electrode glass cell in the hanging meniscus rotating disk configuration (HMRD)³⁰ with an Au(111) single crystal (MaTeck GmbH) as working electrode. A reversible hydrogen electrode (RHE) was employed as reference electrode, a Pt mesh as counter electrode. The applied potentials were measured with two different potentiostats (PGStat20, Metrohm Autolab, Netherlands and a Potentiostat ECi-200, Nordic Electrochemistry, Denmark). The measurements were performed in degassed 0.1 M perchloric acid (70%, Merck Millipore, USA). After the electrolyte was saturated, cyclic voltammograms were at a scan rate of 100 mV/s. For the HOR/HER, the electrolyte was saturated with pure hydrogen and polarization curves were recorded between -0.3 V and 0.6 V vs. RHE at a scan rate of 10 mV/s and a rotation of 1600 rpm. The mass loading was calculated according to the STEM image (Fig. 1) with a 5.3% Pt coverage and an average diameter of 2.3 nm. The mass of 1 platinum nanoparticle was estimated and correlated to the surface coverage, yielding a final mass loading of the particles on the surface of 0.8 mg.

Monte Carlo Simulation. Kinetic simulations are performed by a modified version of our previous studies^{31, 32} based on the work by Xiao and Ming³³. A simple $s^2 = 100 \times 100$ grid is used to

mimic the flattening process of supported PtNP. Energies and temperatures are reported in units of room temperature (kT_0). Platinum clusters with a six atom edge length are randomly placed on the grid with a surface coverage of 5%. $s^2 \exp(-E_{a,diff}(T)/T)$ atoms are allowed to diffuse per time step Δt and interact on the surface with a diffusion activation energy of $E_{a,diff}(T)$. Single steps to neighboring sites are allowed however the particle must occupy the lowest unoccupied site. The energy of an atom is the sum of the interaction between neighboring atoms (E_{pp}) and the surface (E_{ps}): $E(T) = nE_{pp} + mE_{ps}$ with n ranging from 1 to 6 possible neighbors and m from 0 to 1. The Metropolis algorithm is applied to decide whether an atom diffuses during each time step. If the energy is reduced by diffusion $E(t + \Delta t) < E(t)$, the atom is moved. In the case that diffusion would cause a particle to occupy a higher energy site, Boltzmann sampling is used to determine whether the particle is moved or not.³⁴ Snapshots of the diffusion are taken at different diffusion times to observe the flattening behavior over time. To incorporate the SAM used in the experimental work, the diffusion barrier is increased from $E_{a,diff} = 0$ to $E_{a,diff} = 3$. According to our experimental results, we assume that the SAM causes a change in the diffusion barrier rather than in the process itself.

RESULTS AND DISCUSSION

Nanoparticle Characterization. The polyol approach allows to prepare stable and well defined particles without the need of stabilizing agents.¹⁶ Recent findings from Schrader *et al.*¹⁵ showed that unprotected particles are covered by CO as weakly bond adsorbates to stabilize the particles. This CO originates from the synthesis process and can be attributed to (decomposed) EG.¹⁵ Hence, prior to the experiments the quality of the unprotected PtNP is controlled by IR spectroscopy (SI1). A characteristic absorption band at ca. 1720 cm^{-1} is seen and can be attributed to the C=O vibrations of carboxyl groups from (decomposed) EG.¹⁵ The particles are analyzed using (high-angle annular dark field – scanning transmission electron microscope (HAADF-STEM)). A representative micrograph is shown in Fig. 1a yielding a sub-monolayer coverage of PtNP on the support with a total surface coverage of 5.37%. According to this micrograph, the particles are well dispersed on the surface without agglomeration in solution or ripening on the support. The statistical evaluation of the observed particle areas is fitted by a Gaussian showing a narrow size distribution of the particles with an average circular diameter of $2.3 \pm 0.3 \text{ nm}$ (Fig. 1b). This diameter can be converted into an electrochemical active surface area (ECSA) using the following equation 1:¹

$$ECSA_{TEM} = \frac{6}{\rho_{Pt} \cdot d} \quad (26)$$

Where ρ_{Pt} is the density (21.45 g/cm^3) and d the average Pt diameter (2.3 nm). From this, the ECSA is calculated as $ECSA_{TEM} = 110 \text{ m}^2/\text{g}_{metal}$.

Self-assembled monolayers on Au(111). Dodecanethiol (DDT) SAMs are used in addition to a bare gold support. SAMs bear the potential to modify the gold surface and engineer the interface properties as e.g. adhesion or wettability.³⁵ By using a densely packed layer of alkanethiols, a spacer layer perpendicular to the surface plane is formed. In electrochemical experiments, this layer decreases faradaic currents and hence, decouples the properties from the particles and the support. A representative STM image of DDT on gold is imaged under ambient conditions (compare SI2). Au vacancy islands can be seen as dark depressions which are characteristic features of the thiol adsorption process.^{24, 36} A close-up of the image reveals a $(\sqrt{3} \times \sqrt{3})R30$ packing structure of the SAM,²⁴ where the sulphur atoms are bound to the threefold hollow sites of the Au(111) crystal.³⁵ In addition, electrochemical measurements show a highly stable behavior up to high oxidation potentials (SI3.1). Besides DDT SAMs, aromatic substituted thiol molecules, biphenylthiol (BPT) and thiophenol (TP), are tested as potential support. However, the electrochemical stability (SI3.2-3) and quality of the SAMs (SI4) are inferior to those observed for alkanethiol SAMs.³⁷ Hence, for further investigations, DDT SAMs are used.

Cyclic voltammetry experiments. For electrochemical measurements, PtNP are coated on a bare as well as on a DDT covered Au(111) surface (by using the same amount of particles as used for the STEM experiments). CV measurements are performed in degassed 0.1 M HClO₄ electrolyte to investigate the stability of the PtNP (Fig. 2). A high scan rate of 100 mV/s is used to enhance the pseudo-capacitive surface processes. The CVs show three different regions: 1) a hydrogen under-potential deposition (H-UPD) (0.05 – 0.35 V), 2) a double-layer (0.35 – 0.8 V), and 3) an oxide region (>0.8 V). The stability cycles of PtNP on Au(111) are shown in Fig. 2a. A decrease in the H-UPD region as well as for the oxide peak formation is observed with increasing cycle number. The characteristic features of the CV are comparable to a polycrystalline Pt electrode (Fig. SI5).

A CV of PtNP on DDT on gold is presented in Fig. 2b. Here, a slight increase in current is observed in both regimes, the H-UPD and oxide formation. The sample containing PtNP on DDT is cycled to higher potentials (1.1 V instead of 1.0 V). At this point, the features of the H-UPD become visible at slightly higher oxidation potentials. The same effect of the H-UPD

region is also observed for even smaller particles ($\approx 1.0 \pm 0.2$ nm) on the bare as well as on the DDT covered surface (SI6).

In order to determine the roughness factor r_f and ECSA of both sample, the charges related to the hydrogen ad- and desorption are used. These charges reflect the number of electrochemically accessible surface sites. These protons are adsorbed and reduced in a one-electron process (eq. 2):



By integrating over the anodic scans of the H-UPD region and normalizing the data to the geometrical surface area (by taking into account the charge density of hydrogen at planar platinum surfaces $\rho = 210 \mu C/cm^2$),³⁸ r_f and ECSA can be calculated. For the calculation, the Pt mass-loading is estimated to 0.8 mg (according to the TEM image in Fig. 1a, also see experimental section). By plotting r_f vs. the cycle number, the time evolution of r_f for PtNP on gold (black squares) and on SAM (orange triangles) is shown in Fig. 2c. For PtNP on the bare gold support two regimes can be distinguished: i) fast decrease rate of r_f of roughly - 0.0002 1/cycle for cycle 1 - 40, and ii) a slower rate of - 0.00005 1/cycle for cycle 40 - 100. In comparison, for PtNP on DDT, a single rate of r_f can be estimated to 0.00001 1/cycle. In addition to the r_f , the ECSA_{H-UPD} of both samples (PtNP/Au and PtNP/SAM) is calculated according to the 1st cycle in the CVs to 30 m²/g_{metal} and 10 m²/g_{metal}, respectively. As compared to the ECSA determined via TEM, only 30% for the PtNP/Au and 10% for the PtNP/SAM sample is obtained from the 1st scan of the H-UPD region. In order to get more insights into the underlying mechanistic details at the interface which can be related to the loss in ECSA, STM measurements are performed.

Scanning tunneling microscopy measurements. PtNP are deposited in a first step on a bare gold surface and imaged under ambient conditions. A STM image of PtNP on Au(111) directly after deposition is shown in Fig. 3a. Individual particles with heights of 1.0 ± 0.2 nm are seen on the gold support. In addition, 2-dimensional (2D) patches which are randomly orientated on the surface are observed with heights up to $0.3 \text{ nm} \pm 0.1 \text{ nm}$. Two subsequent images are taken after 3 and 6 min and are presented in Fig. 3b and c, respectively. It can be seen, that the particle height decreases until it reaches a value of approximately $0.3 \text{ nm} \pm 0.1 \text{ nm}$. The respective line profiles of a), b) and c) are indicated in the images and are shown in Fig. 3d. It is observed that the intact particles undergo a flattening process resulting in a Pt over layer that is monoatomic in height. According to this time series, the flattening process starts immediately

when the particles are in direct contact with the gold surface.

Fig. 4 shows large-scale STM images of PtNP deposited on DDT/Au(111). Single particles are stable on top of DDT with heights of 0.4 ± 0.1 nm and 0.8 ± 0.1 nm. The corresponding line profile is shown in Fig. 4c. In addition, 2D patches which are randomly oriented on the surface are observed with a height of 0.25 ± 0.03 nm (line profile in Fig. 4d). These 2D patches seem to be mobile on the surface (SI7). According to these images, the surface roughness decreased over time from 2.5 \AA to 1.2 \AA and 0.6 \AA for 0, 20 and 40 min, respectively. Another interesting observation is presented in Fig. 4b. Here, intact particles are observed especially at step edges which are sunken into the DDT SAM. The corresponding line profile is shown in Fig. 4e.

In order to compare the stability and activity of PtNP on DDT with ligand-functionalized particles, DDT is used to functionalize the PtNP and is deposited on a bare gold support. A representative STM image is presented in Fig. 5a. Here it can be seen, that the particles are stable on the surface without ripening or degradation. A corresponding height distribution is presented in Fig. 5b. It is observed that the distribution is broader in comparison to the unprotected particles (Fig. 1a), yielding an average diameter of 0.9 ± 0.4 nm. Further, the reactivity of these supported ligand-capped PtNP is measured in CV experiments (SI8). The particles are stable on the surface to electrochemical potentials of 1.0 V suggesting a strong bond between the thiol ligands and the platinum. However, although the particles reveal a good stability, the accessibility is limited due to the ligands.

Monte Carlo simulation. Kinetic simulations are carried out to compare the flattening process of PtNP on the bare as well as on the DDT/gold surface. Here, a pre-existing gold film is used³² and small platinum clusters with a six atom edge length (corresponding to a diameter of approximately 2 nm) are randomly placed on the grid with a surface coverage of 5%. The snapshots are taken at several time steps of the diffusion process and are shown in Fig. 6. For the kinetic modeling including the DDT SAM, a higher diffusion barrier is taken to mimic the junction.

The simulation of PtNP on Au(111) is shown in the upper row of Fig. 6. Here, it can be seen that the flattening process starts immediately when the PtNP are in direct contact to the gold surface. After the first snapshot, the initial height of the particles is reduced to 50% while the area covering the surface is increased. In the third image, the final height of approx. 1/6 of the initial height is reached. In the subsequent snapshots, it is observed that the patches grow into larger ones while the height and surface coverage is kept at a constant value. A similar simulation was made for the PtNP on DDT/Au(111) by assuming a higher diffusion barrier (Fig. 6, bottom

row). Here, it is observed that the overall flattening rate is reduced however, the same final results are obtained. The SAM acts only as a barrier which has to be overcome by the particles.

DISCUSSION

It was shown that a loss in ECSA and r_f was obtained for PtNP on the bare gold surface with potential cycling (>100 cycles). For PtNP on DDT/Au(111), a loss in the initial ECSA was observed, whereas potential cycling (>100 cycles) showed an increase in r_f . From CV experiments, the underlying processes which are responsible for the decrease in the ECSA as well as the opposite trend in the time evolution of r_f on both surfaces, cannot unambiguously be determined. In order to get more insights in the prevailing processes at the interface, STM and Monte Carlo experiments were performed. STM time series of the processes at the respective substrate taken at the nanometer scale revealed further mechanistic details which can be linked to the loss in ECSA. These results are confirmed by kinetic simulations. The combined approach allows to get a more detailed picture of the morphology change of PtNP on Au and DDT/Au interfaces.

PtNP on Au(111). For PtNP on Au(111), the presented CV above can be summarized as follows: i) initial decrease of the ECSA, followed by ii) two different decay rates of r_f during potential cycling. Here, the first decay rate of r_f (cycle 1 - 40) is 4-times faster than the second rate (cycle 40 - 100). Subsequent STM images revealed a decrease in particle height, when deposited on Au(111). By subsequent scanning the same area, a further flattening of the particles is observed resulting in 2D patch formation of Pt on Au that are monoatomic in height.

The main question arises: what are the driving forces of the flattening process of the particles on Au? And how can the two different decay rates of r_f be explained. For comparing our results, we first focus on the fundamentals which occur during the 2D island growth of Pt overlayers on Au. Pt nanoisland formation on Au is mainly studied by electrodeposition from solutions containing H_2PtCl_6 .^{13, 22, 39, 40, 41} Ostermayr *et al.*²² reported a preferred Pt deposition (0.15 ML) nearly exclusively on step and defect sites on defect-rich Au(111). Wolfschmidt *et al.*⁴¹ observed, that defects on Au terraces can act as nucleation center for the Pt growth (0.1 ML). On Au(111) surfaces, such defects as e.g. holes are created due to the lifting of the (111) reconstruction.⁴¹ For higher concentrations of Pt (>1 ML), a layer-by-layer growth is postulated.^{39, 42} Uoaski *et al.*³⁹ proposed an adlayer packing structure of PtCl_6^- on Au(111) which is similar to the Pt(111) structure. The results imply, that there is a high affinity of Pt to Au with a stronger Pt-Au interaction than the Pt-Pt interaction. Thus, the flattening process can be attributed to this strong interaction of Pt and Au which results in 2D structures at the surface. However it does not

give any explanations of the loss in ECSA and the two regimes with different decay rates of r_f . If there would be only a flattening of the particles, the particle volume would stay constant. This would even result in more active sites since the bulk Pt atoms would become accessible during the flattening process. Hence, there must be an underlying process which cannot unambiguously be seen in CVs or STM (since an atomically resolved structure was not obtained).

Pedersen *et al.*⁴² proposed a mechanism, in which alloying occurred for the first 0.03 ML of Pt into the topmost layer of gold and displacing single Au atoms out of the layer. By further increasing the Pt concentration (0.2 ML), a mixed overlayer of Au and Pt is obtained. They concluded, that this mixed island growth is thermodynamically stable due to the energetic advantage of Pt being capped by Au. Hence Pt atoms are exchanged directly at the interface with Au atoms from the top layer. If Pt concentrations of >0.2 ML are used, a layer of Pt orders on top of this layer. These findings may explain the loss in ECSA and the first decay rate of r_f ; after the flattening of the particles, alloying occurs at the Au interface. Since the decay rate of r_f in the second regime (cycle 40 – 100) is 4-times smaller than the rate in the first regime (cycle 1 – 40), a much slower process must take place. For Pt clusters on a graphite surface, it was observed that for 10 - 30 atoms of Pt, a diffusion coefficient of $5.0 \times 10^{-11} \text{ m}^2/\text{s}^2$ can be estimated.⁴³ However, a much lower diffusion coefficient is expected for Pt on Au due to the higher interaction of Pt and Au (in comparison to Pt on carbon) and the mismatch of the respective lattice parameters (Pt 2.78 Å, Au 2.88 Å and HOPG 2.46 Å).^{42, 44} It was shown by Deltour *et al.*,⁴⁵ that if the mismatch is small, as in the case for Pt and Au, the Pt clusters are locked in a specific place by the substrate. One explanation which may correlate with our results is, that after the initial flattening of the particles, the single Pt atoms diffuse to the specific adsorption sites of the Au substrate, forming a monolayer. Hence, a slower decrease rate of r_f is observed in our CV experiments. Evidence for a monolayer of Pt on Au could be obtained by measuring the specific electroactivity for Pt for the HER/HOR. A two order of magnitude enhancement for small coverages of Pt on Au(111) in comparison to a bare platinum surface is found.⁴¹ This enhancement can be explained by the d-band coupling model of Nørskov where the surface reactivity is given by a shift of the surface d-states with respect to the Fermi level.^{42, 46, 47} This shift changes the electronic properties of the overlayer.⁴⁸ Thus we carefully checked the HOR/HER activities of our proposed monolayer of Pt on Au. Here, an enhancement for HOR as well as HER can be observed in comparison to a bare Pt crystal (Fig. 7).

With this evidence, we conclude that after a flattening of the particles, followed by a reorientation of the Pt atoms on the gold surface, our final stage is composed out of a 2D Pt nanoisland

structure that is monoatomic in height.

PtNP on DDT/Au(111). For PtNP on DDT/Au(111) the presented CV above can be summarized to i) an initial loss in ECSA, followed by ii) a slight increase in the time evolution of r_f during potential cycling (cycles 1 – 100) with a single rate. In this system, the included mechanistic details are much more complex than on the bare gold surface. Hence, we address our first attention to the underlying processes including the penetration of particles through the SAM. According to our STM results, some of the PtNP are stable on top of DDT however, 2D patches that are monoatomic in height are observed. The main question is: what is the mechanism for the decay of the particles on DDT forming these 2D patches? In general, two possible explanations can be given to answer this question. 2D patches can form either to i) an intact particle penetration, followed by a rearrangement of the particle atoms forming a monolayer or ii) a particle decay through the SAM layer. The first possible explanation can be supported by findings of Costelle *et al.*⁴⁹ suggesting an Au particle penetration through the SAM as a whole particle. For the latter possibility, an atom-by-atom decay was proposed for Ag and Cu clusters on SAMs.²⁸ Here, the formation of transient defects or nucleation sites in the SAM²⁶ locally enhance the penetration of the deposited clusters. Duffe *et al.*²⁵ reported a similar decay through the SAM for Ag particles on C₆₀ layers. They concluded, that the attractive forces of the metal can lower the barrier which is necessary to extract mono- or multimer from a cluster. By comparing our results to the above mentioned two particle penetration mechanisms, we have a strong evidence that in the case for PtNP on DDT, the first explanation is more plausible; the particles penetrate through the SAM as a whole particle followed by a reordering of the single Pt atoms on the surface. Our assumption is based on our STM results, especially the ones taken at gold step edges. Here, it can be seen, that the particles sink into the SAM while retaining their shape. In comparison to the bare gold surface, where it seems that gold step edges can act as nucleation centers for Pt nanoisland formation, these active sites are blocked by the SAM. Further, in our experiments 2D patch formation is only observed on larger gold terraces. From these findings we conclude, that the likeliest process of Pt 2D patch formation consist of an intact particle penetration on extended gold terraces. This process could be enabled by transient defects on the SAM.

According to our kinetic simulations, we confirmed that the general process of the particle flattening followed by a reorientation of the single atoms is the same for a bare Au and DDT/Au surface. Thus, we assume that the underlying process as we proposed for PtNP on Au also applies for our DDT/Au surface. However, for the DDT/Au interface, the SAM acts as a barrier

and slows down the flattening as well as the reorientation process of the single Pt atoms. If this would be the only process, a decreasing rate of r_f would be expected. Instead, a slight increase of r_f is observed in CV experiments. Here, according to STM measurements, some PtNP are stable on top of DDT. One possible explanation for the increase in r_f includes a cleaning of the particle surface by cycling. During cycling, Pt oxide forms in the anodic scan at an onset of 0.8 V, whereas in the cathodic scan, it is reduced to Pt, obtaining a clean surface. According to our results, the cleaning of the top particles must be the predominant process seen in the CV, superimposing the flattening and reorientation process of the particles.

Conclusive, the results for PtNP/Au(111) and PtNP/DDT can be summarized by the following equations (3) and (4), respectively:

$$\frac{\partial r_f}{\partial t} = \begin{cases} x_n = -0.0002 \quad \forall 1 \leq n \leq 40, & n \in N \\ y_n = -0.00005 \quad \forall 40 \leq n \leq 100, & n \in N \end{cases} \quad (28)$$

$$\frac{\partial r_f}{\partial t} = \begin{cases} z_n = 0.00001 \quad \forall 1 \leq n \leq 100, & n \in N \end{cases} \quad (29)$$

Whereas a two-step degradation mechanism is observed for PtNP on Au(111), a single step mechanism is obtained for PtNP on DDT. We have a strong evidence, that this single rate is composed out of three competing processes: flattening, reorientation of the penetrating particles and cleaning of the top PtNP. Since the processes are slowed down by the SAM, the two regimes, as it can be seen on the bare gold surface, cannot unambiguously be determined by CV experiments. Further, we believe that the electric field of the STM enhances the flattening process, however is not the driving force for this process.

CONCLUSION

Unprotected PtNP bear the potential to be used as model catalyst. In this article, new insights into the degradation mechanism of PtNP on gold and DDT covered gold surfaces are presented. A two-step flattening mechanism was observed in electrochemical experiments and confirmed by experiments and kinetic simulations. Additionally, PtNP supported on DDT-covered gold surfaces showed 2D patch formations on the gold support. A further approach allows to prepare ligand-capped PtNP. Although the measured electrochemical activity was far beyond those of PtNP, supported ligand-stabilized particles could open the way towards stable and reactive particles. By tuning the ligand coverage, the ratio of stability vs. activity can be maximized.

AUTHOR INFORMATION

Corresponding Author

*E-mail: friedrich.esch@tum.de

Present Addresses

L.N. Department of Chemistry, Massachusetts Institute of Technology, 77 Massachusetts Ave. Building 2-216, Cambridge, MA, 02139

Notes

The authors declare no competing financial interest.

Acknowledgement

This work was supported by the Nanosystems Initiative Munich (NIM) (S.W. and U.H.) and the DFG projects HE3454/18-1 and -2, HE3454/23-1 (U.H.), respectively ES349/1-1 and -2 (F.E.). Research at Illinois was supported by a grant from the National Science Foundation, NSF CHE 1307002 (L.N., S.W., J.W.L. and M.G.). Electron beam evaporation was performed at the Micro and Nanotechnology Laboratory, University of Illinois. The authors thank Florian F. Schweinberger for assistance with sample preparation and Dalaver H. Anjum from the ‘Advanced Nanofabrication Imaging and Characterization’ lab at King Abdullah University of Science and Technology (KAUST) for his help in acquiring the STEM micrograph/s in the SI.

Supporting Information. IR spectrum of PtNP, additional STM images and CVs of aliphatic and aromatic SAM on gold, CV experiments of platinum clusters on SAM and gold, CV of ligand-capped PtNP.

REFERENCES

1. Durst, J.; Simon, C.; Hasche, F.; Gasteiger, H. A., Hydrogen Oxidation and Evolution Reaction Kinetics on Carbon Supported Pt, Ir, Rh, and Pd Electrocatalysts in Acidic Media. *J. Electrochem. Soc.* **2014**, *162*, F190-F203.
2. Gasteiger, H. A.; Panels, J. E.; Yan, S. G., Dependence of PEM fuel cell performance on catalyst loading. *J. Power Sources* **2004**, *127*, 162-171.
3. Wilson, M. S.; Fernando, H. G.; Sickafus, K. E.; Gottesfeld, S., Surface Area Loss of Supported Platinum in Polymer Electrolyte Fuel Cells. *J. Electrochem. Soc.* **1993**, *140*, 2872-2877.
4. Yu, K.; Groom, D. J.; Wang, X.; Yang, Z.; Gummalla, M.; Ball, S. C.; Myers, D. J.; Ferreira, P. J., Degradation Mechanisms of Platinum Nanoparticle Catalysts in Proton Exchange Membrane Fuel Cells: The Role of Particle Size. *Chem. Mat.* **2014**, *26*, 5540-5548.
5. Shao-Horn, Y.; Sheng, W. C.; Chen, S.; Ferreira, P. J.; Holby, E. F.; Morgan, D., Instability of Supported Platinum Nanoparticles in Low-Temperature Fuel Cells. *Top. Catal.* **2007**, *46*, 285-305.
6. Campbell, C. T.; Parker, S. C.; Starr, D. E., The effect of size-dependent nanoparticle energetics on catalyst sintering. *Science* **2002**, *298*, 811-814.
7. Maillard, F.; Eikerling, M.; Cherstiouk, O. V.; Schreier, S.; Savinova, E.; Stimming, U., Size effects on reactivity of Pt nanoparticles in CO monolayer oxidation: The role of surface mobility. *Farad. Discuss.* **2004**, *125*, 357-377.
8. Shao, M.; Peles, A.; Shoemaker, K., Electrocatalysis on platinum nanoparticles: particle size effect on oxygen reduction reaction activity. *Nano Lett.* **2011**, *11*, 3714-3719.
9. Cherevko, S.; Keeley, G. P.; Geiger, S.; Zeradjanin, A. R.; Hodnik, N.; Kulyk, N.; Mayrhofer, K. J. J., Dissolution of Platinum in the Operational Range of Fuel Cells. *ChemElectroChem* **2015**, *2*, 1471-1478.
10. Geiger, S.; Cherevko, S.; Mayrhofer, K. J. J., Dissolution of Platinum in Presence of Chloride Traces. *Electrochim. Acta* **2015**, *179*, 24-31.
11. Tang, L.; Han, B.; Persson, K.; Friesen, C.; He, T.; Sieradzki, K.; Ceder, G., Electrochemical stability of nanometer-scale Pt particles in acidic environments. *J. Am. Chem. Soc.* **2010**, *132*, 596-600.

12. Meier, J. C.; Galeano, C.; Katsounaros, I.; Witte, J.; Bongard, H. J.; Topalov, A. A.; Baldizzone, C.; Mezzavilla, S.; Schuth, F.; Mayrhofer, K. J., Design criteria for stable Pt/C fuel cell catalysts. *Beilstein J. Nanotechnol.* **2014**, *5*, 44-67.
13. Wolfschmidt, H.; Weingarth, D.; Stimming, U., Enhanced reactivity for hydrogen reactions at Pt nanoislands on Au(111). *ChemPhysChem* **2010**, *11*, 1533-1541.
14. Perini, L.; Durante, C.; Favaro, M.; Perazzolo, V.; Agnoli, S.; Schneider, O.; Granozzi, G.; Gennaro, A., Metal-support interaction in platinum and palladium nanoparticles loaded on nitrogen-doped mesoporous carbon for oxygen reduction reaction. *ACS Appl. Mater. Interfaces* **2015**, *7*, 1170-1179.
15. Schrader, I.; Warneke, J.; Neumann, S.; Grotheer, S.; Swane, A. A.; Kirkensgaard, J. J. K.; Arenz, M.; Kunz, S., Surface Chemistry of "Unprotected" Nanoparticles: A Spectroscopic Investigation on Colloidal Particles. *J. Phys. Chem. C* **2015**, *119*, 17655-17661.
16. Wang, Y.; Ren, J.; Deng, K.; Gui, L.; Tang, Y., Preparation of Tractable Platinum, Rhodium, and Ruthenium Nanoclusters with Small Particle Size in Organic Media. *Chem. Mat.* **2000**, *12*, 1622-1627.
17. Kunz, S.; Schreiber, P.; Ludwig, M.; Maturi, M. M.; Ackermann, O.; Tschurl, M.; Heiz, U., Rational design, characterization and catalytic application of metal clusters functionalized with hydrophilic, chiral ligands: a proof of principle study. *Phys. Chem. Chem. Phys.* **2013**, *15*, 19253-19261.
18. Speder, J.; Altmann, L.; Bäumer, M.; Kirkensgaard, J. J. K.; Mortensen, K.; Arenz, M., The particle proximity effect: from model to high surface area fuel cell catalysts. *RSC Adv.* **2014**, *4*, 14971-14978.
19. Solla-Gullón, J.; Aldaz, A.; Clavilier, J., Ultra-low platinum coverage at gold electrodes and its effect on the hydrogen reaction in acidic solutions. *Electrochim. Acta* **2013**, *87*, 669-675.
20. Schaefer, P. J.; Kibler, L. A., Incorporation of Pd into Au(111): enhanced electrocatalytic activity for the hydrogen evolution reaction. *Phys. Chem. Chem. Phys.* **2010**, *12*, 15225-15230.
21. Kibler, L. A., Hydrogen electrocatalysis. *ChemPhysChem* **2006**, *7*, 985-991.
22. Ostermayr, C.; Stimming, U., Electrocatalytic activity of platinum submonolayers on defect-rich Au(111). *Surf. Sci.* **2015**, *631*, 229-234.

23. Love, J. C.; Estroff, L. A.; Kriebel, J. K.; Nuzzo, R. G.; Whitesides, G. M., Self-assembled monolayers of thiolates on metals as a form of nanotechnology. *Chem. Rev.* **2005**, *105*, 1103-1169.
24. Vericat, C.; Vela, M. E.; Benitez, G.; Carro, P.; Salvarezza, R. C., Self-assembled monolayers of thiols and dithiols on gold: new challenges for a well-known system. *Chem. Soc. Rev.* **2010**, *39*, 1805-1834.
25. Duffe, S.; Gronhagen, N.; Patryarcha, L.; Sieben, B.; Yin, C.; von Issendorff, B.; Moseler, M.; Hovel, H., Penetration of thin C60 films by metal nanoparticles. *Nat. Nanotechnol.* **2010**, *5*, 335-339.
26. Kühnle, A.; Vollmer, S.; Linderoth, T. R.; Witte, G.; Wöll, C.; Besenbacher, F., Adsorption of Dodecanethiol on Cu(110): Structural Ordering upon Thiolate Formation. *Langmuir* **2002**, *18*, 5558-5565.
27. Walker, A. V.; Tighe, T. B.; Cabarcos, O. M.; Reinard, M. D.; Haynie, B. C.; Uppili, S.; Winograd, N.; Allara, D. L., The dynamics of noble metal atom penetration through methoxy-terminated alkanethiolate monolayers. *J. Am. Chem. Soc.* **2004**, *126*, 3954-3963.
28. Costelle, L.; Räisänen, M. T.; Joyce, J. T.; Silien, C.; Johansson, L.-S.; Campbell, J. M.; Räisänen, J., Structural Evolution of Gas-Phase Coinage Metal Clusters in Thiolate Self-Assembled Monolayers on Au. *J. Phys. Chem. C* **2012**, *116*, 22602-22607.
29. Wilms, M.; Kruft, M.; Bermes, G.; Wandelt, K., A new and sophisticated electrochemical scanning tunneling microscope design for the investigation of potentiodynamic processes. *Rev. Sci. Instrum.* **1999**, *70*, 3641-3650.
30. Cahan, B. D.; Villullas, H. M., The hanging meniscus rotating disk (HMRD). *J. Electroanal. Chem. Interfacial Electrochem.* **1991**, *307*, 263-268.
31. Carmichael, E. S.; Gruebele, M., Controlling the Smoothness of Optically Transparent Gold Films by Temperature Tuning. *J. Phys. Chem. C* **2009**, *113*, 4495-4501.
32. Nienhaus, L.; Scott, G. E.; Haasch, R. T.; Wieghold, S.; Lyding, J. W.; Gruebele, M., Transparent Metal Films for Detection of Single-Molecule Optical Absorption by Scanning Tunneling Microscopy. *J. Phys. Chem. C* **2014**, *118*, 13196-13202.
33. Xiao, R.-F.; Ming, N.-B., Surface roughening and surface diffusion in kinetic thin-film deposition. *Phys. Rev. E* **1994**, *49*, 4720-4723.

34. Metropolis, N.; Rosenbluth, A. W.; Rosenbluth, M. N.; Teller, A. H.; Teller, E., Equation of State Calculations by Fast Computing Machines. *J. Chem. Phys.* **1953**, *21*, 1087-1092.
35. Bürgi, T., Properties of the gold-sulphur interface: from self-assembled monolayers to clusters. *Nanoscale* **2015**, *7*, 15553-15567.
36. Poirier, G. E., Characterization of Organosulfur Molecular Monolayers on Au(111) using Scanning Tunneling Microscopy. *Chem. Rev.* **1997**, *97*, 1117-1128.
37. Vericat, C.; Vela, M. E.; Salvarezza, R. C., Self-assembled monolayers of alkanethiols on Au(111): surface structures, defects and dynamics. *Phys. Chem. Chem. Phys.* **2005**, *7*, 3258-3268.
38. Biegler, T.; Rand, D. A. J.; Woods, R., Limiting oxygen coverage on platinized platinum; Relevance to determination of real platinum area by hydrogen adsorption. *J. Electroanal. Chem. Interfacial Electrochem.* **1971**, *29*, 269-277.
39. Uosaki, K.; Ye, S.; Naohara, H.; Oda, Y.; Haba, T.; Kondo, T., Electrochemical Epitaxial Growth of a Pt(111) Phase on an Au(111) Electrode. *J. Phys. Chem. B* **1997**, *101*, 7566-7572.
40. Liu, Y.; Gokcen, D.; Bertocci, U.; Moffat, T. P., Self-terminating growth of platinum films by electrochemical deposition. *Science* **2012**, *338*, 1327-1330.
41. Wolfschmidt, H.; Bussar, R.; Stimming, U., Charge transfer reactions at nanostructured Au(111) surfaces: influence of the substrate material on electrocatalytic activity. *J Phys Condens Matter* **2008**, *20*, 374127.
42. Pedersen, M. Ø.; Helveg, S.; Ruban, A.; Stensgaard, I.; Lægsgaard, E.; Nørskov, J. K.; Besenbacher, F., How a gold substrate can increase the reactivity of a Pt overlayer. *Surf. Sci.* **1999**, *426*, 395-409.
43. Chen, J.; Chan, K.-Y., Size-dependent mobility of platinum cluster on a graphite surface. *Mol. Simul.* **2005**, *31*, 527-533.
44. Tatar, R. C.; Rabii, S., Electronic properties of graphite: A unified theoretical study. *Phys. Rev. B* **1982**, *25*, 4126-4141.
45. Deltour, P.; Barrat, J.-L.; Jensen, P., Fast Diffusion of a Lennard-Jones Cluster on a Crystalline Surface. *Phys. Rev. Lett.* **1997**, *78*, 4597-4600.
46. Ruban, A.; Hammer, B.; Stoltze, P.; Skriver, H. L.; Nørskov, J. K., Surface electronic structure and reactivity of transition and noble metals *J. Mol. Catal. A* **1997**, *115*, 421-429.

-
47. Hammer, B.; Nørskov, J. K., Theoretical surface science and catalysis—calculations and concepts. *Adv. Catal.* **2000**, *45*, 71-129.
48. Mavrikakis, M.; Hammer, B.; Nørskov, J. K., Effect of Strain on the Reactivity of Metal Surfaces. *Phys. Rev. Lett.* **1998**, *81*, 2819-2822.
49. Costelle, L.; Järvi, T. T.; Räisänen, M. T.; Tuboltsev, V.; Räisänen, J., Binding of deposited gold clusters to thiol self-assembled monolayers on Au(111) surfaces. *Appl. Phys. Lett.* **2011**, *98*, 043107.

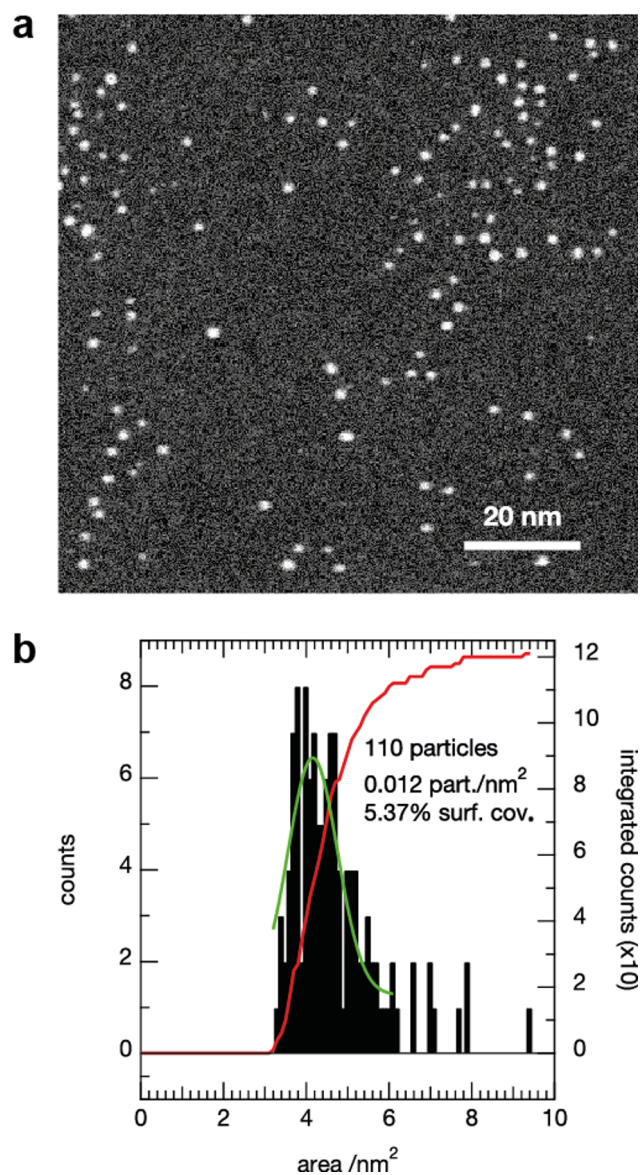


Figure 1 High-angle annular dark field representative scanning transmission electron microscope (HAADF-STEM) micrograph ($100 \times 100 \text{ nm}^2$) of platinum nanoparticles on a carbon support (a) and statistical evaluation of the observed particle area (b). The particle area is fitted by a Gaussian fit (green line) showing a maximum at a particle area of 4.1 nm^2 , corresponding to an average circular diameter of 2.3 nm.

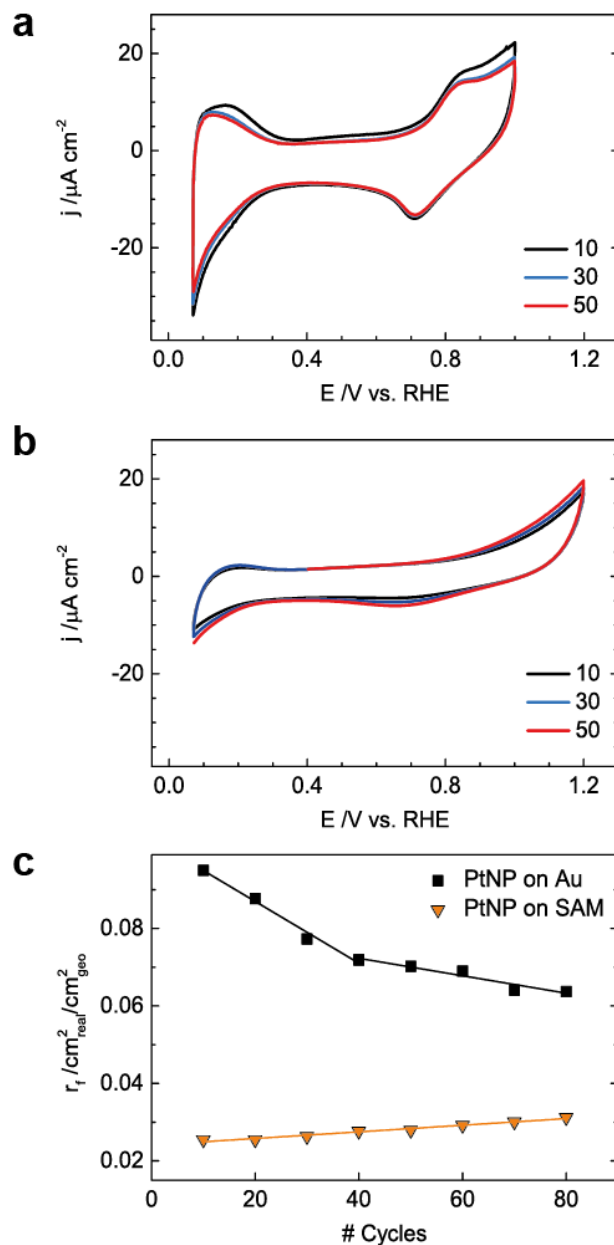


Figure 2 CV measurements and corresponding calculations of the roughness factor. a) CV of PtNP on Au(111), b) CV of PtNP on a dodecanethiol SAM on Au(111), c) calculated roughness factors of PtNP on Au(111) (black squares) and SAM/Au(111) (orange triangles). All CV measurements are performed in 0.1 M HClO₄ in degassed electrolyte (Ar) with a scan rate of 100 mV/s. The decrease of the active area was calculated by integrating over the hydrogen regime between 0.05 V and 0.3 V.

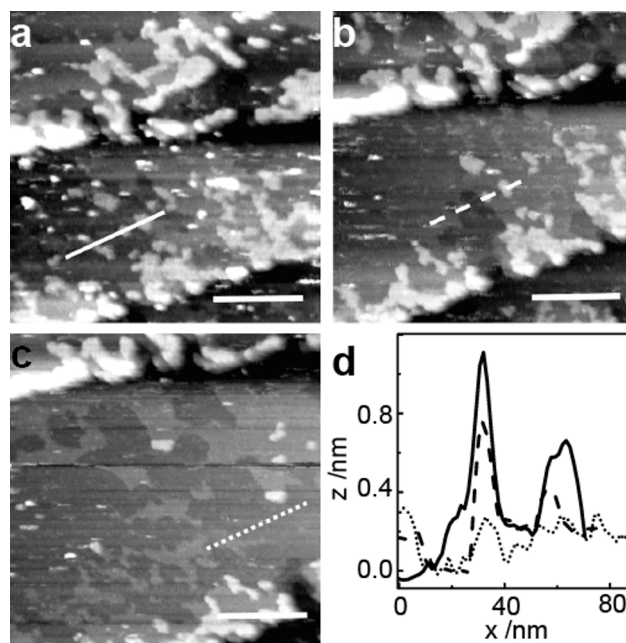


Figure 3 STM images of supported PtNP on a gold single crystal taken immediately (a) and after 3 min (b) and 6 min (c). Scale bars in all images: 30 nm, Scanning parameters: $I_t = 15$ pA, $U_t = 900$ mV. Corresponding line profiles are shown in (d). The profiles are taken at the marked line in the images. (black (a), dashed (b) and dotted (c)).

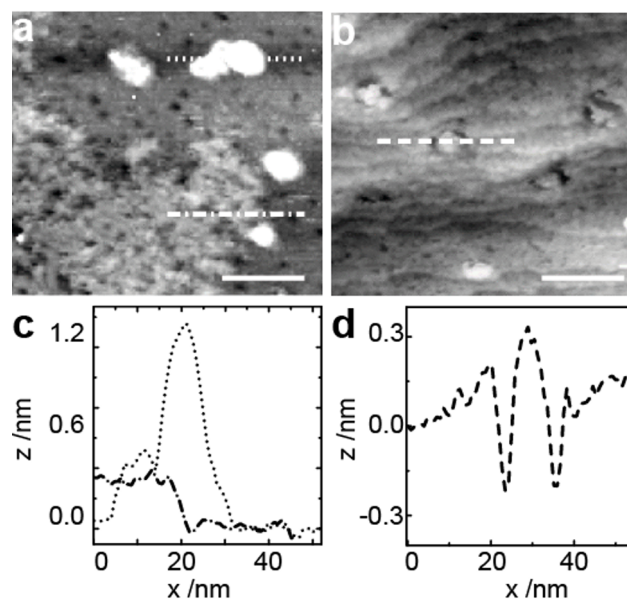


Figure 4 STM images of PtNP on a dodecanethiol self-assembled monolayer on Au(111). a) STM image taken at an extended area (a) and a gold step edge (b). The corresponding line profiles of a) are shown in c), d), respectively. The line profile of b) is shown in e). Scale bars in STM images: 20 nm. Scanning parameters: $I_t = 10$ pA, $U_t = 800$ mV.

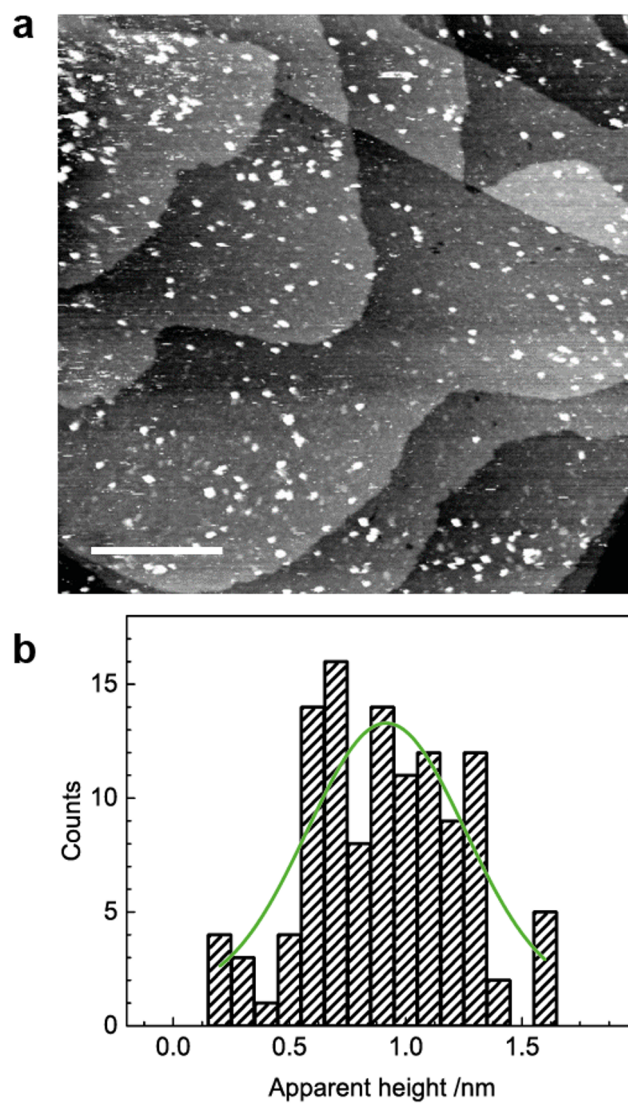


Figure 5 STM image of functionalized dodecanethiol PtNP on a gold surface (a). Scale bar: 100 nm. Scanning parameters: $I_t = 15$ pA, $U_t = 950$ mV. The corresponding apparent height distribution of the particles is shown in b).

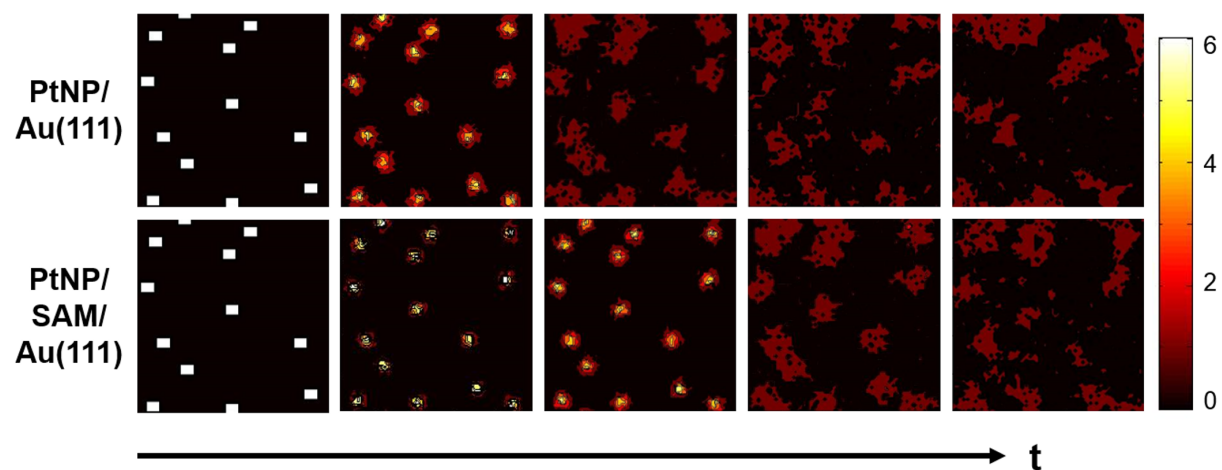


Figure 6 Monte Carlo simulations for PtNP on a bare (top row) as well as on a SAM covered surface (bottom row).

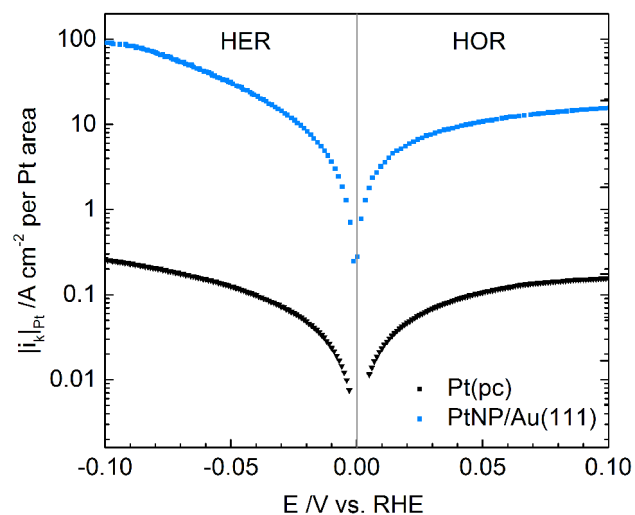


Figure 7 Tafel plot of the HER/HOR for Pt(pc) (black) and for PtNP on Au(111) (blue) in 0.1 M HClO₄ at 10 mV/s and 1600 rpm. The kinetic current densities are plotted per Pt area assuming steady state conditions for the PtNP (after approximately 100 potential cycles to 1.0 V in Ar and by using a r_f of 0.06 for the calculations).

Supporting Information

Mechanistic Details on the Flattening Mechanism of Supported Platinum Nanoparticles on Gold and Thiol-Terminated Self-Assembled Monolayers

S. Wieghold^{§,#}, L. Nienhaus^{&,+}, A. Siebel^{¶,#}, M. Krause^{§,#}, P. Wand^{§,#}, M. Gruebele^{&,+,#}, U. Heiz^{§,#}, F. Esch^{§,#}

[§]Physical Chemistry, [¶]Chair of Electrochemistry and [#]Catalysis Research Center, Chemistry Department, Technische Universität München, Lichtenbergstr. 4 and Ernst-Otto-Fischer-Str. 1, 85748 Garching, Germany

[&]Beckman Institute for Advanced Science and Technology, ⁺Department of Chemistry and

[§]Department of Physics, University of Illinois, Urbane, Illinois 61801

1. IR spectrum of unprotected platinum nanoparticle

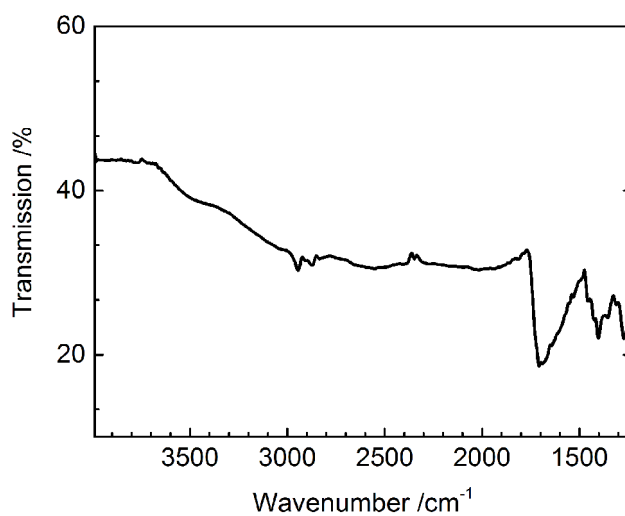


Figure S1 Transmission IR spectrum of unprotected PtNP dried on KBr from dispersion in cyclohexanone. The spectrum is background corrected.

2. STM image of 1-dodecanethiol SAM on gold

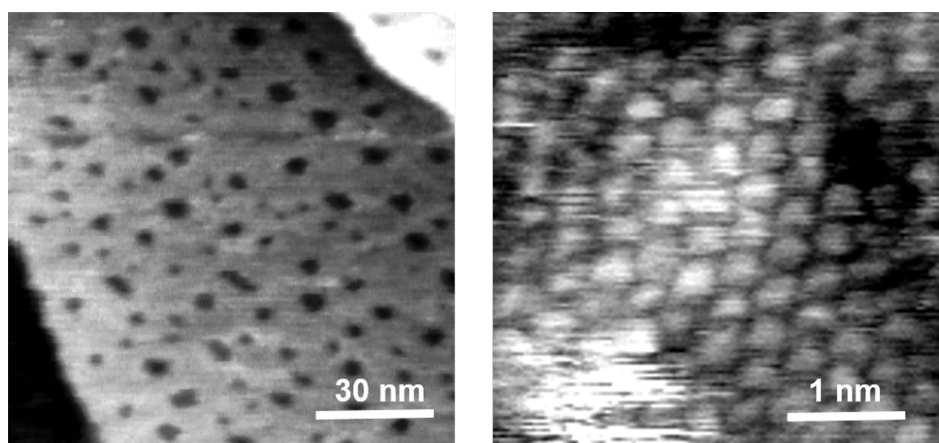


Figure S2 Representative STM images of a 1-dodecanethiol SAM on Au(111) at ambient conditions. Left: large scale image; right: close-up showing the $(\sqrt{3}\times\sqrt{3})R30$ packing structure of the SAM. Scanning conditions: $I_t = 10$ pA, $U_t = 800$ mV.

3. CV measurements of alkane and aromatic thiols on Au(111)

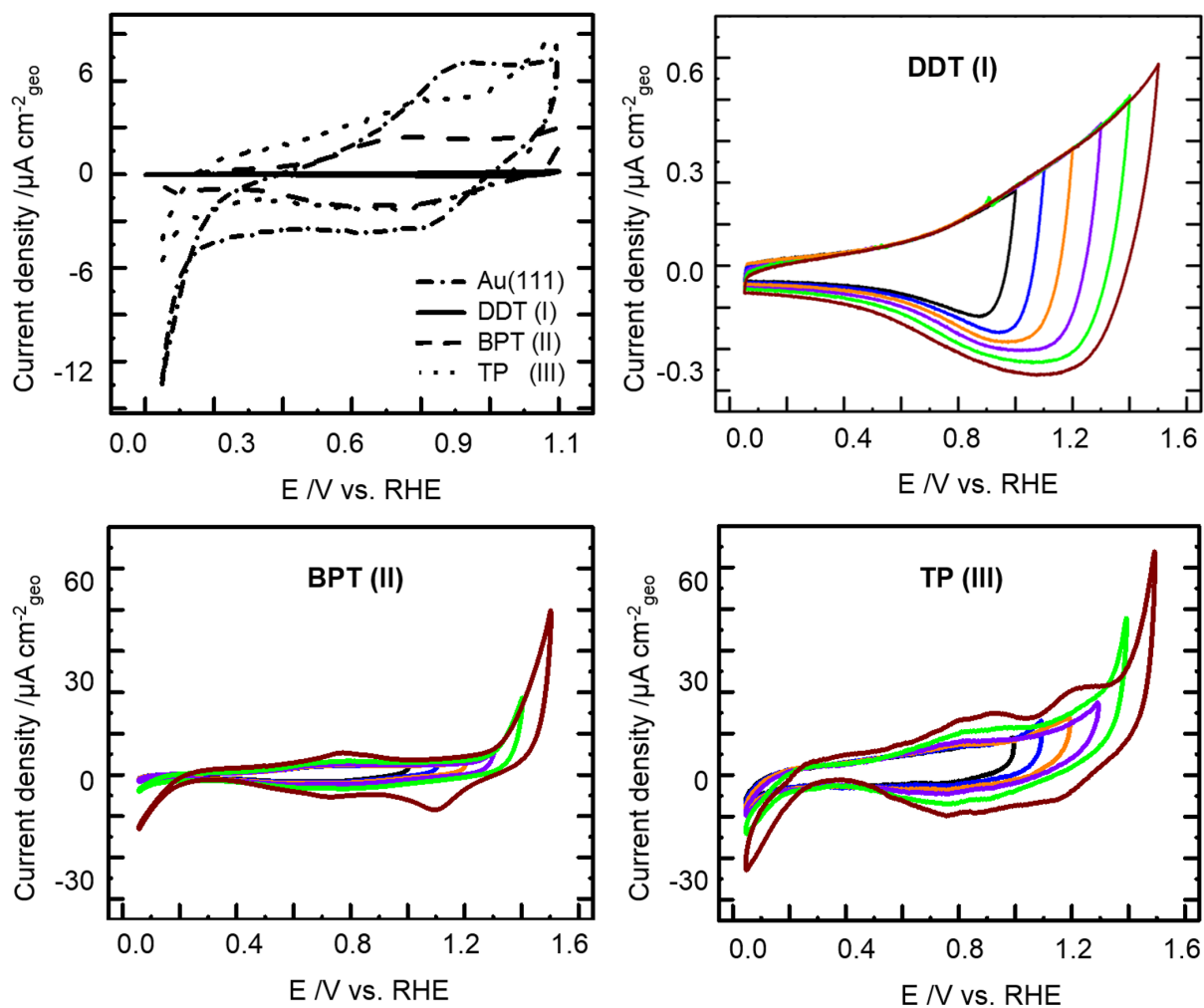


Figure S3 Representative CVs of a dodecanethiol (DDT, I), biphenylthiol (BPT, II) and thiophenol (TP, II) SAM on Au(111). The bare gold CV is shown in the left top CV. CVs are measured in degassed 0.1 M perchloric acid with a RHE as reference electrode and a scan speed of 50 mV/s (I) and 100 mV/s (II, III).

4. STM measurements of aromatic thiols on Au(111)

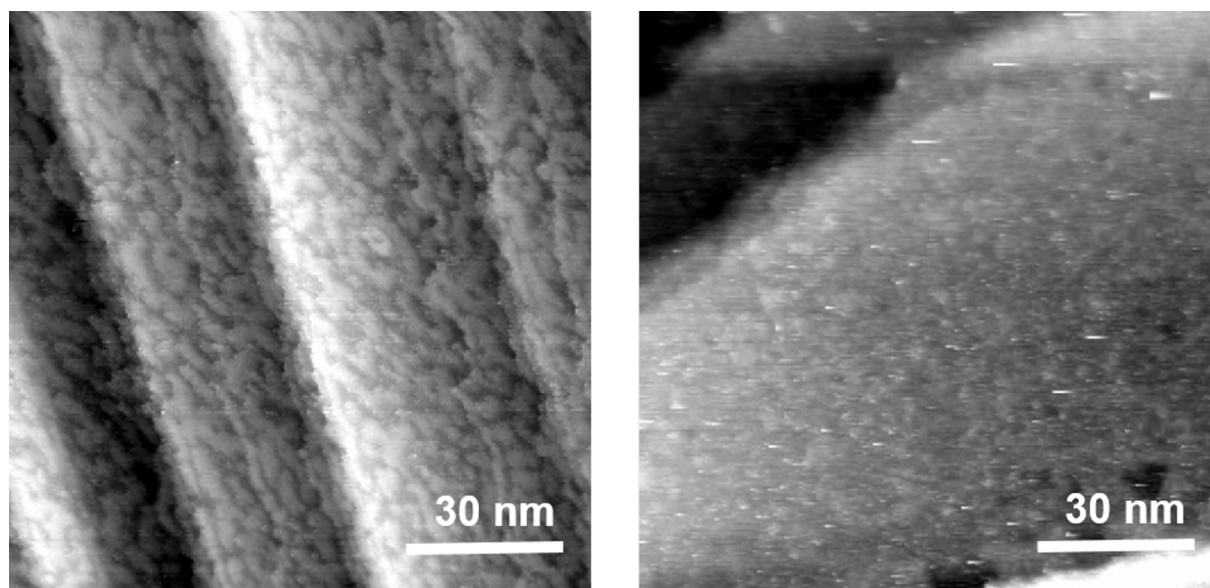


Figure S4 Representative STM images of BPT (left) and TP (left) and on Au(111). Scanning conditions for both images: $I_t = 12$ pA, $U_t = 700$ mV.

5. CV of a polycrystalline platinum disk

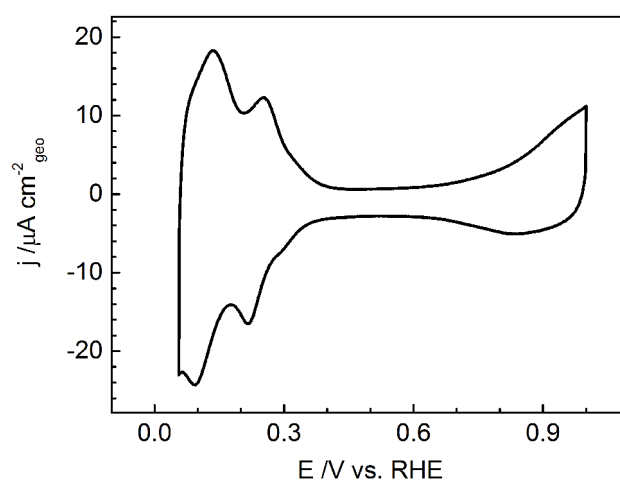


Figure S5 Representative CV of a platinum disk in degassed 0.1 M perchloric acid with a RHE as reference electrode and a scan speed of 100 mV/s.

6. Additional CV data of Pt clusters on Au(111) and SAM/Au(111)

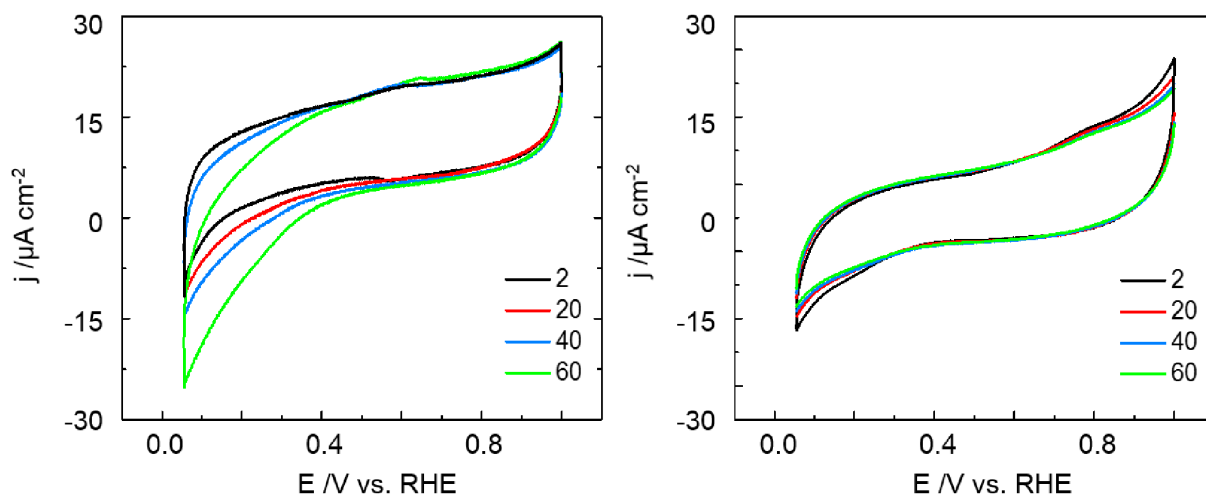


Figure S6 CV measurements of unselected platinum clusters ($\text{Pt}_{n>35}$) on a gold support (left) and DDT (right). The surface coverage of the Pt clusters is estimated to 7.25% according to the cluster current of 0.049 e/nm^2 .¹ The cluster preparation under UHV conditions is described in detail elsewhere.^{2, 3, 4} CVs are measured in degassed 0.1 M perchloric acid with a RHE as reference electrode and a scan speed of 100 mV/s.

7. Time series of PtNP on SAM/Au(111)

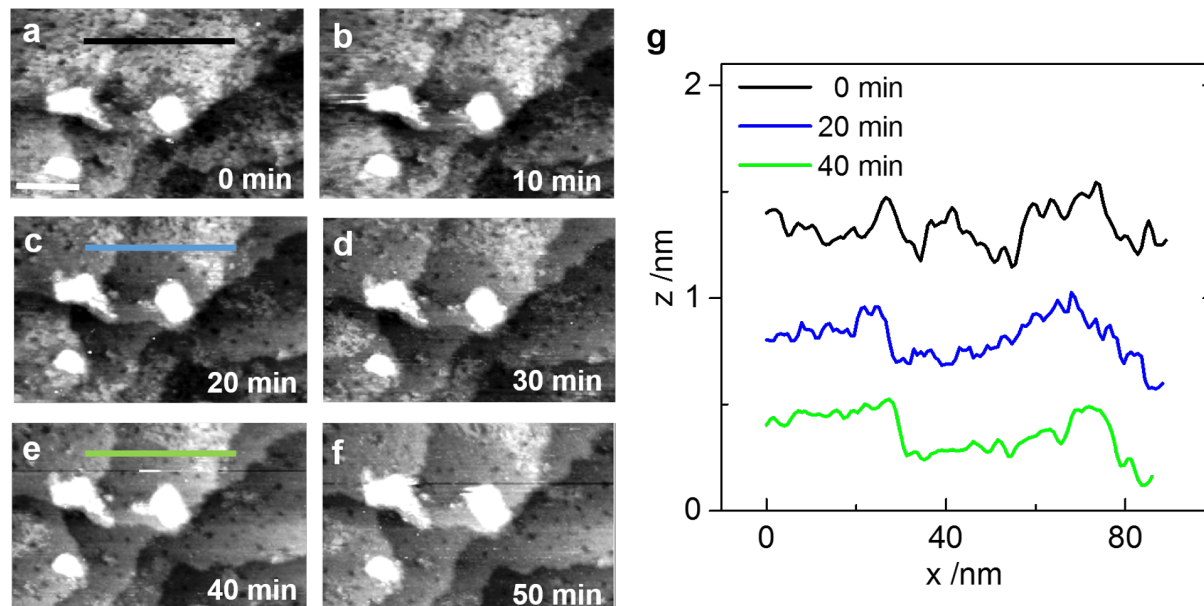


Figure S7 Representative STM images of PtNP on 1-dodecanethiol SAM on Au(111). The images are taken in time steps of 10 min at the same position. The corresponding line profiles of a) (black line), c) (blue line) and e) (green line) are shown on the right graph. Scanning parameters: $I_t = 10 \text{ pA}$, $U_t = 800 \text{ mV}$.

8. CV of ligand-capped PtNP on Au(111)

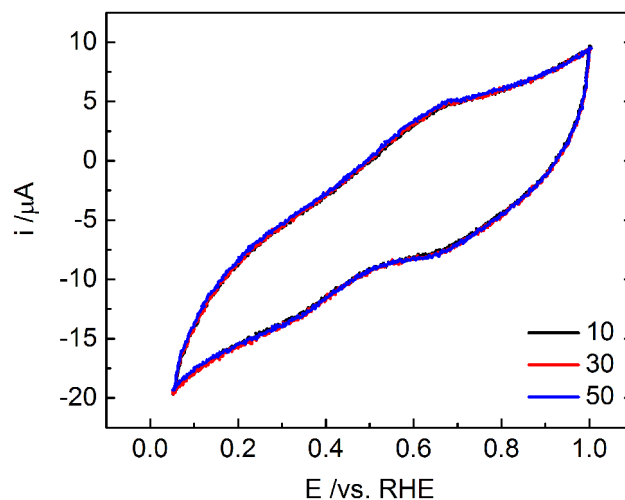


Figure S8 Representative CV of DDT functionalized PtNP on Au(111). The CV is measured in degassed 0.1 M perchloric acid with a RHE as reference electrode and a scan speed of 100 mV/s.

Additional SI References

1. Schweinberger, F. F., *Catalysis with supported size-selected Pt clusters*. Springer International Publishing: New York **2014**.
2. Heiz, U.; Landmann, U., *Nanocatalysis*. Springer-Verlag: Berlin Heidelberg **2007**.
3. Heiz, U.; Vanolli, F.; Trento, L.; Schneider, W. D., *Chemical reactivity of size-selected supported clusters: An experimental setup*. *Rev. Sci. Instrum.* **1997**, *68*, 1986-1994.
4. Schweinberger, F. F.; Berr, M. J.; Doblinger, M.; Wolff, C.; Sanwald, K. E.; Crampton, A. S.; Ridge, C. J.; Jackel, F.; Feldmann, J.; Tschurl, M.; Heiz, U., Cluster size effects in the photocatalytic hydrogen evolution reaction. *J. Am. Chem. Soc.* **2013**, *135*, 13262-13265.

Conclusion

In this chapter, the flattening process of platinum NP on a bare gold and thiol-covered support was investigated. It was demonstrated, that platinum NP could not be stabilized on top of a thiol monolayer. A two-step degradation mechanism was found for NP on a gold surface and confirmed by STM experiments. In addition, NP on SAMs showed a more stable behavior in CV measurements however, penetration and patch formation was observed. By functionalizing the particles with thiols, an enhanced stability on the gold surface was found whereas the electrochemical activity was reduced. Kinetic simulations supported the proposed hypothesis of a two-step degradation mechanisms and revealed that the SAM acts as an additional barrier for the particles.

The presented results showed the potential of functionalized particles on electrochemical inactive substrates towards HOR/HER. By specifically tailoring the ligand concentrations on the NP, the stability can be maintained while increasing the accessibility of the reactants.

Plasmonic Activation of 1 nm Platinum Clusters for Photocatalysis

SMA-STM combines the high spatial resolution of the STM with the high energy resolution inherent in optical spectroscopy [82]. The modulation of the light intensity and dedicated lock-in detection of the tunneling current allows to detect the influence of optical absorption on the tunneling current. This technique can be used to study light-induced effects e.g. photovoltaic effects in semiconductors [137], resonant excitation of surface plasmons (SP) [138] as well as information on the tip-sample system itself [82, 139]. By employing a plasmonically active surface such as Au or Ag [82, 88], SP can be excited via a prism in the Kretschmann configuration [83]. Especially thin gold films (< 15 nm) bear the potential to be used in SMA-STM studies since they are semi-transparent while exhibiting atomically flat island structures [140].

The manuscript titled 'Plasmonic activation of 1 nm platinum clusters for photocatalysis' is presented in this section. Unselected platinum clusters are deposited on a thin gold support. First, the morphology and absorption properties of the thin gold film are examined using UV-vis spectroscopy. AFM images reveal the structure of the thin gold film exhibiting small nanoislands as well as nanoholes which lead to the characteristic extinction spectrum of the film. Since the platinum clusters have a small cross section, no direct absorption is expected in the visible range. The support and clusters are imaged in SMA-STM under chopped laser light. The rectified plasmon signal can be observed on the Au support as well as on the clusters. The coupling of SP lead to a lowering of the potential barrier for tunneling electrons and thus, an enhanced absorption signal of the Pt clusters. To prove this enhanced photoexcitation, methylene blue (MB) is coated on the bare and platinum supported Au surfaces. The oxidative decomposition of MB is induced by illuminating the samples with a 520 nm LED followed by monitoring the decrease in the peak maximum using UV-vis spectroscopy.

The SMA-STM experiments were performed by Sarah Wieghold together with Lea Nienhaus at the Beckman Institute at the University of Illinois at Urbana-Champaign, IL, USA. Both authors contributed equally to this work.

Plasmonic Activation of 1 nm Platinum Clusters for Photocatalysis

*S. Wieghold^{§, #}, L. Nienhaus^{&, †, #}, F. L. Knoller[§], F. F. Schweinberger[§], J. W. Lyding^{Ⓜ, ^}, U. Heiz[§], M. Gruebele^{&, †, Ⓜ, *}, F. Esch^{§, *}*

[§]Physical Chemistry and Catalysis Research Center, Chemistry Department, Technische Universität München, Lichtenbergstr. 4 and Ernst-Otto-Fischer-Str. 1, 85748 Garching, Germany

[&]Beckman Institute for Advanced Science and Technology, [†]Department of Chemistry, [^]Department of Electrical and Computer Engineering, and [Ⓜ]Department of Physics, University of Illinois, Urbane, Illinois 61801

KEYWORDS. local surface plasmon resonance, gold films, platinum clusters, scanning tunneling microscopy, single molecule absorption, methylene blue decomposition, photocatalysis

ABSTRACT

Nanometer-sized metal clusters have the potential to function as prime candidates for photocatalysis based on their tunable unique optical and electronic properties, combined with large surface-to-volume ratio. Due to the very small optical cross sections of such nanoclusters, support-mediated plasmonic activation is most efficient. Our semi-transparent gold film, optimized to work in a back-illumination geometry, has a surface plasmon resonance excitable with 532 nm light. Pt_n clusters (size distribution peaked at n=46 atoms), deposited on this film, are imaged with optically-assisted scanning tunneling microscopy with nanometer resolution to resolve the resulting localized plasmonic excitation of the Pt clusters. Plasmonic excitation and electron transfer enhance the light-induced tunneling current on the clusters relative to their gold support. Finally, we make the connection with improved catalytic activity. We compare the performance of the pristine gold film with that of Pt clusters supported on the gold film, for the oxidative decomposition of a methylene blue film. The Pt cluster catalytic activity under illumination exceeds the gold surface baseline activity by more than an order of magnitude per active area.

INTRODUCTION

Plasmonic photocatalysis is a promising approach to enhance photocatalytic activity of non-absorbing catalysts with visible light. A visible absorber is combined with a catalytically active material to facilitate electron transfer and thus redox reactions. In the canonical approach, a catalytic large-gap semiconductor that does not absorb visible light, such as mesoporous TiO_2 , is combined with a photostable visible absorber, such as plasmonic gold nanoparticles.¹ Several non-canonical schemes for plasmonic photocatalysis have been developed. For example, platinum clusters have been deposited onto CdS rods to catalyze hydrogen evolution, Pt_{46} being most efficient. In that case, a metal nanoparticle acts as the catalyst, and the semiconductor as the photosensitizer, reversing the roles from the conventional approach.² The disadvantage is that semiconductor particles are not as stable under long-term light exposure as the metal ones. This problem can be avoided by making absorber and catalyst one and the same metal: e.g. silver nanocubes have been used as both plasmonic and catalytic substrate to drive the ethane epoxidation reaction.³ However, in that case plasmon resonance and catalytic ability cannot be tuned independently. Here we expand the flexibility of these alternative approaches by using a quantum junction between two different metals for plasmonic photocatalysis. Thus, the catalytic metal and the plasmonic metal can be tuned independently to achieve large surface-to-volume ratio of the catalyst, optimal absorption by the photosensitizer, and optimal electron and energy transfer between the two. In our experiments, the photocatalytic ability of small Pt clusters (size distribution peaked at $n=46$, diameter 1 ± 0.2 nm) is enabled by their interaction with a visible light-absorbing plasmonic gold film. Figure 1 illustrates the geometry (not to scale) by which plasmonic excitation is transferred from the semi-transparent gold film into a localized surface plasmon resonance (LSPR) of the Pt clusters. We illuminate the gold film from the back by 532 nm light, so that we can carry out STM studies during illumination. We perform two measurements to link this LSPR of Pt clusters on a gold surface with enhanced photocatalysis. First, we use single molecule optical absorption spectroscopy detected by scanning tunneling microscopy (SMA-STM)⁴ to image with nanometer spatial resolution the localized electron density change induced by the LSPR in the Pt clusters. Next, we demonstrate enhanced catalysis of oxidative methylene blue (MB) decomposition by the Pt clusters under visible illumination as a test reaction.⁵ Several very general properties of metal nanoparticles and of plasmonic metal surface make our approach feasible.⁶ First of all, it has been shown that small semiconductor^{7, 8} and metal nanoparticles^{9, 10} can support LSPR: the increased carrier density in nanoparticles in comparison to bigger particles offsets the smaller number of electrons in the plasmon, sustain-

ing a collective excitation. For metal nanoparticles, two size effects compete: decreasing size increases the catalytically active surface-to-volume ratio, but also shifts the LSPR towards the UV,^{11, 12} so direct visible excitation cannot occur. However, the work functions of the Au film (≈ 5.3 eV¹³) and of Pt nanocrystals (tunable from ≈ 5.9 eV¹⁴ in the bulk towards lower values for small particles¹⁵) are similar, facilitating charge transfer from Au to Pt, and thus increasing the electron density to support LSPR (Figure 1). A good compromise size can be found for many metal combinations. For example, d to s,p interband transitions in our Pt clusters, excited by plasmon leakage from the gold surface, lead to damped LSPR, but our ≈ 1 nm cluster diameter still allows the Au SPR to couple to the entire Pt nanocrystal.¹¹ Such coupling is enhanced when the two metals are in < 1 nm contact, where electron tunneling becomes possible and even a conductive regime is entered.^{16, 17}

RESULTS AND DISCUSSION

Absorption by bare gold surfaces. Figure S1a shows the extinction spectra of gold layers of different thicknesses. The 2 nm gold film shows a nearly constant background signal due to reflectivity. The extinction increases and the line shape develops a minimum around 500 nm with increasing gold thickness. These absorption spectrum characteristics can be explained by the morphology of the film. The plasmon frequency strongly depends on the nanostructure of the surface, as shown by several groups for metal films with nanoholes:¹⁸ size-specific surface plasmon polaritons lead to extinction maxima (< 400 nm in our case), while localized resonances in nanoholes lead to extinction minima (500 nm in our case).^{19, 20} The 10 nm gold film shown in Figure S1b and Figure 2a exhibits a pronounced morphology of large, flat and interconnected islands on the length scale of 100 – 200 nm with well-defined boundaries.

Morphology and absorption spectra are similar to that observed by Doron-Mor *et al.*,²¹ who note that their spectra as well as morphology change strongly after annealing to 200 °C due to an island coarsening that leads to increased absorption around 520 nm, the typical plasmon frequency of Au nanoparticles. We therefore carefully checked that morphology and absorption of our films did not change upon annealing to 120 °C, the temperature we applied for degassing our samples (see Figure S2).

No direct absorption by gold-supported Pt clusters. Next, we deposited $\text{Pt}_{n>35}$ clusters (size distribution peaked at $n=46$ atoms, ≈ 1 nm, see STEM micrograph Figure S3) on top of the 10 nm thin plasmonically active gold film to study the coupling behavior at the metal-metal junction under light illumination and UHV conditions. To rule out significant direct Pt

absorption, UV-VIS spectra of the cluster-assembled samples were recorded beforehand (Figure S4). No change in the wavelength dependence could be observed, as expected for the low Pt cluster coverages used and for the low Pt cluster cross section in the range of 400 – 800 nm, as characterized theoretically and experimentally by hyper-Rayleigh scattering (HRS) spectroscopy by Johnson *et al.*²² and down to 38 nm cluster diameter by Langhammer *et al.*¹¹ The local surface plasmon resonance (LSPR) will blue-shift to the UV region for our even smaller particle sizes, as shown by Zorić *et al.*,¹² so we exclude direct excitation upon the 520 - 532 nm illumination described in the following.

Strong plasmonic activation of Pt detected by SMA-STM. SMA-STM detects the modulation of the tunneling current caused by the change in local electron density (LDOS).²³ We excited the gold surface with an amplitude-modulated laser operating at 532 nm, where gold surface plasmons get excited, but small Pt clusters do not absorb directly. Identical quality topography images of Pt clusters on gold could be obtained with and without laser excitation (Figure 2a and 2b).

The different work functions of Pt and Au, important to assist charge injection into Pt clusters for LSPR formation, have a detectable effect on the STM images. The observed average cluster height is 0.87 ± 0.06 nm with the laser off (Figure 2c). This value decreases by 0.3 nm, well outside measurement uncertainty, when the modulated laser illumination is switched on, while the cluster shapes are perfectly retained (compare Figures 2a and 2b). The observation can be explained based on the Pt and Au work functions. We measure at increased distance upon illumination, so the attenuation length z_0 of the tunneling current $I \sim \exp(z/z_0)$ over Au vs. Pt plays an important role. The different work functions determine z_0 : over Pt with its higher work function, the tunneling current decays more rapidly than over Au and an apparently lower cluster height results upon illumination. The gold film topography, on the contrary, is imaged in exactly the same way with and without illumination. In particular, step edges (Figure S5) do not change height and we do not observe any distortions that might be induced by local plasmonic fields.

The SMA-STM signal, induced by the indirect plasmonic excitation of Pt clusters at positive sample bias, consists of a ca. 0.1 pA additional modulation of the tunneling current through clusters relative to the gold surface, in phase with the laser modulation. Figure 3a shows the topography scan, co-localized with the SMA-STM signal in Figure 3b (darker = higher current when light is on). The tunneling current modulation can be explained by DC rectification of the plasmon electric field – either directly excited in the gold SPR, or indirectly but strongly cou-

pled into the LSPR of the clusters. When characterizing the $I(V)$ dependence under illumination (Figure 3c), we observe indeed a strong signature of this plasmon rectification:^{24, 25} The characteristic symmetry of the metallic-like $I(V)$ curve of the bare Au film around 0 V bias (Figure 3d) is broken. The illuminated tunneling junction acts like a diode, with a low-conducting plateau at negative sample bias that extends to -500 mV, indicating the plasmon rectification voltage that counteracts small negative sample bias (where the current would flow from sample to tip). A similar plateau is observed on the supported Pt clusters, although slightly less extended than on the bare gold surface.

With the laser on, we observe that the tunneling current increases on the clusters (Figures 3b and 4a, black=positive current modulation). This is in contrast to observations of semiconducting PbS quantum dots deposited on similar Au films, where the tunneling current decreases upon illumination due to direct photoexcitation of band gap transitions.²⁶ The net increase of tunneling current observed on Pt clusters is similar in magnitude to the net decrease observed for direct photoexcitation of a semiconductor quantum dot.²⁶ The tunneling current increase has at least two plausible explanations: 1) a higher LDOS of the Pt clusters under illumination opening up further channels into which tip electrons can tunnel; 2) an LSPR-induced reduced tunneling barrier (theoretically predicted by Tagliacozzo *et al.*²⁷), which depends on the local work function of clusters and gold support.

We also studied the bias dependence of the SMA-STM signal on the gold support alone and with Pt clusters. The gold support presents a smooth current modulation of ca. 0.025 pA, independent of the bias. The SMA-STM signal shows a bias dependence with a peak at 1.0 V (Figure 4). An energy shift of 1 eV is consistent with resonantly enhanced excitation of Pt charge carriers from the d- to the s,p-band of Pt in presence of the tip electric field, supporting the activation of a LSPR within the clusters. A 1 eV energy boost for tunneling electrons originating from the gold surface plasmon would close the gap between the visible absorption maximum of the gold surface plasmon (500 nm), and the near-UV absorption maximum for the d-s,p transitions in small Pt clusters (350 nm).¹¹

Enhanced catalytic activity under illumination. Plasmon modes can be coupled into gold surfaces by a Kretschmann geometry excitation, asperities (gold surface trenches and step edges, as well as Pt nanoparticles), but also by a nearby STM tip. All three are present in our SMA-STM geometry (Figure 1). As observed by Berndt *et al.*,²⁸ plasmon modes are strongly influenced by the tip field. Therefore, we investigated whether the observed Pt cluster LSPR detected by SMA-STM is a tip-specific phenomenon, or whether plasmonic activation also occurs

in the absence of the tip, leading to a measurable catalytic effect.

In order to address this question, we measured the catalytic activity for the oxidative decomposition of methylene blue (MB), as shown in Figure 5. The bare and the cluster-covered Au films were covered with MB by immersing the supports for 2 h into an ethanolic MB solution and drying them thereafter. By comparison to a calibration line (extinction at 657 nm, Figure S6), final surface concentration equivalents of 3.3 μM and 6.1 μM resulted for the Au film with and without Pt clusters. Conversion into relative coverages yields approximately 2 ML and 4 ML, respectively.

As can be seen in Figure 5, films with or without Pt clusters show no oxidative activity in the absence of illumination over a period of 5 minutes. When illuminating the films with increasing photon doses of 520 nm LED light in air, and subsequently measuring the extinction spectra, we observe some catalytic activity already on the bare, nanostructured Au film. This catalytic activity is doubled at equal light intensity on the cluster-covered film, from ca. 1.1 $\mu\text{M}/\text{min}$ (gold only) and 2.0 $\mu\text{M}/\text{min}$ (gold with Pt clusters). Taking into account the cluster coverage (7% of surface area measured by STEM, Figure S3), and fitting first order rate kinetics to the data, we obtain $k_{\text{Au}} = 0.09 \text{ min}^{-1}$ for the gold film only, $k_{\text{Pt-Au}} = 0.19 \text{ min}^{-1}$ for 7% Pt cluster coverage on gold film, and $k_{\text{Pt}} = 1.38 \text{ min}^{-1}$ for Pt clusters at the same surface area as the gold film. Thus the Pt clusters are catalytically over an order of magnitude more active than the gold film alone. The MB decomposition in air has been proposed to be an oxidative process.²⁹ Why might such a process be catalytically enhanced by SPR on gold, or LSPR on Pt clusters? We can tentatively assign this effect to a facilitation of the O_2 dissociation. As shown in detail by Christopher *et al.*,^{3, 5} plasmon photoexcitation of Ag nanoparticles leads to a strong photo enhancement in the ethene epoxidation or in the MB decomposition. In the case of the ethene epoxidation, the O_2 dissociation has been shown to be rate-limiting and the mechanism could be related to the population of O_2 antibonding orbitals by plasmon excitation. This population leads to the formation of a transient negative-ion state that leads to dissociation via vibrational excitation. Thus, also here the photo enhancement of the MB decomposition by the $\text{Pt}_{n>35}$ cluster/plasmonic Au might be explained by enhanced oxygen dissociation.⁵ On the $\text{Pt}_{n>35}$ clusters, however, this excitation is indirect and the population of O_2 antibonding orbitals has to occur via the clusters.

CONCLUSION

In this work we have investigated the indirect excitation of Pt clusters, supported on plasmonic

Au films, for catalytic applications. We have directly observed enhanced electron density and tunneling through Pt clusters on the gold support illuminated with light of 532 nm, even though the clusters cannot strongly absorb visible light. The gold support however can, forming a surface plasmon. At positive sample biases, the gold SPR increases the overall tunneling current by an additional electron flow from tip to sample, and this contribution is enhanced by the excitation of LSPR on the clusters, as imaged with local resolution by SMA-STM. We propose a mechanism whereby electron migration from Au to Pt, due to the different work functions, is enhanced by surface plasmon excitation of the gold substrate, leading to a d-s,p excitation-based LSPR in the Pt clusters. We could also show that the illuminated gold films already possess some catalytic ability for oxidation of MB, but the activity is over an order of magnitude larger for Pt clusters on a per-area basis.

EXPERIMENTAL SECTION

Thin film preparation. Au films of up to 10 nm thickness were used as a semi-transparent substrate to allow for excitation with the 532 nm laser (Figure S1a). They are supported on a 5 nm Pt film on a c-plane sapphire support, and are fabricated by electron beam deposition.³⁰ Under the conditions used in this study, Pt and Au do not alloy and no Pt XPS signal is observed for the Au film of 10 nm thickness.³⁰ Unlike the continuous Au films used in previous SMA-STM studies,^{4, 26} the films showed discrete ≈ 200 nm islands allowing for plasmon confinement (Figure S1b).

Pt cluster deposition. Pt clusters were deposited on the 10 nm Au films, as well as on TEM grids (2 nm carbon support on 300 mesh copper grids – Surface Services, Germany). A high frequency laser ablation cluster source connected to a transfer chamber was used as reported previously.^{2, 31} Briefly, the beam of a Nd:YAG laser (100 Hz, 70 mJ at 532 nm – DPSS Spitlight, Innolas, Germany) is focused onto a rotating (1 Hz) Pt target, creating a plasma that is cooled by a helium gas pulse and subsequent adiabatic expansion through a nozzle into vacuum. After a quadrupole bender stage, the cluster cation beam is mass-separated by a QMS (ABB, Extrel Merlin, U.S.A. – mass limit 16000 amu) operated as a high-pass mass filter (RF-only mode). With this arrangement, only clusters of $n > 35$ atoms, whose size distribution has a maximum at $n=46$, could pass the filter.³¹ The cluster beam is focused onto the substrate, assuring soft-landing conditions (deposition energies lower than 1 eV per atom. Recording the discharge current on the support during deposition, and assuming unity charge per cluster, the average coverage of the deposited clusters is determined to 0.049 e/nm². STM overview images after transfer through air

reveal that the clusters are randomly distributed and show neither agglomeration at step edges nor visible ripening effects (Figure 2a). Statistical analysis of larger areas ($100 \times 100 \text{ nm}^2$) by STEM supports the observation of stable clusters and further reveals the cluster sizes to be in the expected size range (Figure S3).²

STM sample preparation. For better conductivity between the cluster-covered thin metal film and the sample holder clamps, thick silver contacts were applied to the two sides of the sample, using colloidal silver paint (TedPella Inc., U.S.A.). The paint is allowed to cure for 1 hour in air, before a 3 mm fused silica right angle prism (Thorlabs) is attached to the sample backside using a UHV compatible epoxy glue (302-3M, Epotek). After further curing for 24 hours, the sample is degassed at $120 \text{ }^\circ\text{C}$ in UHV for 12 hours prior to imaging. Mechanically cut platinum-iridium (80:20) tips were used for STM imaging. All tips underwent a high temperature resistive degassing for 12 hours prior to imaging.

SMA-STM setup. The STM measurements were performed in a home-built UHV STM setup similar to the one reported previously.³² All STM images were taken at a tunneling current of 5 pA and a variable sample bias. The SMA-STM experiments apply the backside illumination technique in Kretschmann configuration (Figure 1).^{4, 26} A 3 mm fused silica prism couples the laser light into the sapphire substrate, allowing for total internal reflection at the sample front, which causes an evanescent wave that decays over the tip-sample junction and that excites the surface plasmons within the gold film. The 532 nm diode pumped solid state (DPSS) laser (10 mW) is focused down to a spot size of about $80 \text{ }\mu\text{m}^2$, resulting in an excitation power of $\approx 1.2 \text{ W/mm}^2$ at the sample, with p-polarization. p-Polarization allows for the perpendicular and longitudinal components of the electric field vector in the surface plasmon polariton at the gold surface to be probed. To allow for detection by a lock-in amplifier, the laser is amplitude-modulated at 2.2 kHz by a mechanical chopper wheel. The SMA-STM measurements are performed with vertical tip feedback that is slower than the modulation frequency. The modulated tunneling current is thus little influenced by mechanical feedback oscillations, although the mean tunneling distance changes when the chopped illumination is switched on due to an increasing overall tunneling current. We simultaneously collect the average tunneling current (topography) and the in-phase modulated current detected by the lock-in amplifier (Stanford Research SR830) at a phase shift of $86 \pm 5^\circ$ with respect to the laser modulation.^{4, 26, 30}

Photocatalytic reactivity measurements. For the photocatalytic measurements, the oxidative decomposition of methylene blue (MB, Sigma-Aldrich) was tracked by UV-VIS measurements that were carried out in a Specord40 spectral photometer (Analytik Jena, Germany). The

spectra were recorded with a step size of 0.5 nm averaging 0.2 s per point. MB is dissolved in ethanol with a concentration of 0.65 mM.⁵ The UV-VIS extinction signal were calibrated with a dilution series starting from this parent solution (Figure S6). The thin films were covered by immersion into the MB solution for 2 h, followed by rinsing in ethanol; the samples were then dried in an argon stream and fixed in a sample holder with an illumination diameter of 2 mm. Between each extinction measurement, the samples were illuminated by a green LED of wavelength 520 ± 10 nm and intensity $13 \mu\text{W}/\text{mm}^2$ (9600 mCd, 30°, Nichia, Japan) for 60 s. The decomposition was measured by recording the extinction maximum of MB at 657 nm.

AUTHOR INFORMATION

Corresponding Author

*E-mail: friedrich.esch@tum.de

*E-mail: mgruebel@illinois.edu

Present Addresses

L.N. Department of Chemistry, Massachusetts Institute of Technology, 77 Massachusetts Ave. Building 2-216, Cambridge, MA, 02139

Author contribution

#S. Wiegold and N. Nienhaus contributed equally.

Notes

The authors declare no competing financial interest.

Acknowledgement

This work was supported by the Nanosystems Initiative Munich (NIM) (S.W. and U.H.) and the DFG projects HE3454/18-1 and -2, HE3454/23-1 (U.H. and F.F.S.), respectively ES349/1-1 and -2 (F.E. and F.L.K.). Research at Illinois was supported by a grant from the National Science Foundation, NSF CHE 1307002 (L.N., S.W., J.W.L. and M.G.). Electron beam evaporation was performed at the Micro and Nanotechnology Laboratory, University of Illinois. The authors thank Marian D. Rötzer and Maximilian Krause for assistance with sample preparation and Dalaver H. Anjum from the ‘Advanced Nanofabrication Imaging and Characterization’ lab at King Abdullah University of Science and Technology (KAUST) for his help in acquiring the STEM micrographs.

Supporting Information. Additional UV-VIS spectra of Au films and supported Pt clusters, AFM image of a thin gold film, HAADF-STEM micrograph and statistical analysis, Au line profiles and methylene blue UV-VIS spectra with corresponding calibration line.

REFERENCES

1. Zhang, X.; Chen, Y. L.; Liu, R. S.; Tsai, D. P., Plasmonic photocatalysis. *Rep. Prog. Phys.* **2013**, *76*, 046401.
2. Schweinberger, F. F.; Berr, M. J.; Döblinger, M.; Wolff, C.; Sanwald, K. E.; Crampton, A. S.; Ridge, C. J.; Jackel, F.; Feldmann, J.; Tschurl, M.; Heiz, U., Cluster size effects in the photocatalytic hydrogen evolution reaction. *J. Am. Chem. Soc.* **2013**, *135*, 13262-13265.
3. Christopher, P.; Xin, H.; Linic, S., Visible-light-enhanced catalytic oxidation reactions on plasmonic silver nanostructures. *Nat. Chem.* **2011**, *3*, 467-472.
4. Nienhaus, L.; Wieghold, S.; Nguyen, D.; Lyding, J. W.; Scott, G. E.; Gruebele, M., Optoelectronic Switching of a Carbon Nanotube Chiral Junction Imaged with Nanometer Spatial Resolution. *ACS Nano* **2015**, *9*, 10563-10570.
5. Christopher, P.; Ingram, D. B.; Linic, S., Enhancing Photochemical Activity of Semiconductor Nanoparticles with Optically Active Ag Nanostructures: Photochemistry Mediated by Ag Surface Plasmons. *J. Phys. Chem. C* **2010**, *114*, 9173-9177.
6. Stampelcoskie, K. G.; Kamat, P. V., Synergistic Effects in the Coupling of Plasmon Resonance of Metal Nanoparticles with Excited Gold Clusters. *J. Phys. Chem. Lett.* **2015**, *6*, 1870-1875.
7. Jain, P. K., Plasmon-in-a-Box: On the Physical Nature of Few-Carrier Plasmon Resonances. *J. Phys. Chem. Lett.* **2014**, *5*, 3112-3119.
8. Faucheaux, J. A.; Stanton, A. L.; Jain, P. K., Plasmon Resonances of Semiconductor Nanocrystals: Physical Principles and New Opportunities. *J. Phys. Chem. Lett.* **2014**, *5*, 976-985.
9. Kreibig, U., Electronic properties of small silver particles: the optical constants and their temperature dependence. *J. Phys. F: Met. Phys.* **1974**, *4*, 999-1014.
10. Lünskens, T.; Heister, P.; Thämer, M.; Walenta, C. A.; Kartouzian, A.; Heiz, U., Plasmons in supported size-selected silver nanoclusters. *Phys. Chem. Chem. Phys.* **2015**, *17*, 17541-17544.
11. Langhammer, C.; Yuan, Z.; Zorić, I.; Kasemo, B., Plasmonic Properties of Supported Pt and Pd Nanostructures. *Nano Lett.* **2006**, *6*, 833-838.
12. Zorić, I.; Zäch, M.; Kasemo, B.; Langhammer, C., Gold, Platinum, and Aluminum Nanodisk Plasmons: Material Independence, Subradiance, and Damping Mechanisms. *ACS Nano* **2011**, *5*, 2535-2546.

13. Sachtler, W. M. H.; Dorgelo, G. J. H.; Holscher, A. A., The work function of gold. *Surf. Sci.* **1966**, *5*, 221-229.
14. Kaack, M.; Fick, D., Determination of the work functions of Pt(111) and Ir(111) beyond 1100 K surface temperature. *Surf. Sci.* **1995**, *342*, 111-118.
15. Reuter-Hack, K.; Kasper, G.; Weber, A. P., Temperature dependence of the work function of free nanoparticle agglomerates. *Appl. Phys. A* **2009**, *95*, 629-634.
16. Tame, M. S.; McEnery, K. R.; Özdemir, Ş. K.; Lee, J.; Maier, S. A.; Kim, M. S., Quantum plasmonics. *Nat. Phys.* **2013**, *9*, 329-340.
17. Zuloaga, J.; Prodan, E.; Nordlander, P., Quantum description of the plasmon resonances of a nanoparticle dimer. *Nano Lett.* **2009**, *9*, 887-891.
18. Schwind, M.; Kasemo, B.; Zorić, I., Localized and propagating plasmons in metal films with nanoholes. *Nano Lett.* **2013**, *13*, 1743-1750.
19. Sannomiya, T.; Scholder, O.; Jefimovs, K.; Hafner, C.; Dahlin, A. B., Investigation of plasmon resonances in metal films with nanohole arrays for biosensing applications. *Small* **2011**, *7*, 1653-1663.
20. Williams, S.; Coe, J., Dispersion Study of the Infrared Transmission Resonances of Free-standing Ni Microarrays. *Plasmonics* **2006**, *1*, 87-93.
21. Doron-Mor, I.; Barkay, Z.; Filip-Granit, N.; Vaskevich, A.; Rubinstein, I., Ultrathin Gold Island Films on Silanized Glass. Morphology and Optical Properties. *Chem. Mater.* **2004**, *16*, 3476-3483.
22. Johnson, R. C.; Li, J.; Hupp, J. T.; Schatz, G. C., Hyper-Rayleigh scattering studies of silver, copper, and platinum nanoparticle suspensions. *Chem. Phys. Lett.* **2002**, *356*, 534-540.
23. Ballard, J. B.; Carmichael, E. S.; Shi, D.; Lyding, J. W.; Gruebele, M., Laser absorption scanning tunneling microscopy of carbon nanotubes. *Nano Lett.* **2006**, *6*, 45-49.
24. Möller, R.; Albrecht, U.; Boneberg, J.; Koslowski, B.; Leiderer, P.; Dransfeld, K., Detection of surface plasmons by scanning tunneling microscopy. *J. Vac. Sci. Technol. B* **1991**, *9*, 506-509.
25. Lenner, M.; Rácz, P.; Dombi, P.; Farkas, G.; Kroó, N., Field enhancement and rectification of surface plasmons detected by scanning tunneling microscopy. *Phys. Rev. B* **2011**, *83*, 205428.

26. Nienhaus, L.; Goings, J. J.; Nguyen, D.; Wieghold, S.; Lyding, J. W.; Li, X.; Gruebele, M., Imaging Excited Orbitals of Quantum Dots: Experiment and Electronic Structure Theory. *J. Am. Chem. Soc.* **2015**, *137*, 14743-14750.
27. Tagliacozzo, A.; Tosatti, E., Tunneling with coupling to surface phonons or surface plasmons. *Phys. Scr.* **1988**, *38*, 301-308.
28. Berndt, R.; Gimzewski, J. K.; Johansson, P., Inelastic tunneling excitation of tip-induced plasmon modes on noble-metal surfaces. *Phys. Rev. Lett.* **1991**, *67*, 3796-3799.
29. Zhang, T.; Oyama, T.; Aoshima, A.; Hidaka, H.; Zhao, J.; Serpone, N., Photooxidative N-demethylation of methylene blue in aqueous TiO₂ dispersions under UV irradiation. *J. Photochem. Photobiol., A* **2001**, *140*, 163-172.
30. Nienhaus, L.; Scott, G. E.; Haasch, R. T.; Wieghold, S.; Lyding, J. W.; Gruebele, M., Transparent Metal Films for Detection of Single-Molecule Optical Absorption by Scanning Tunneling Microscopy. *J. Phys. Chem. C* **2014**, *118*, 13196-13202.
31. Schweinberger, F. F., *Catalysis with Supported Size-selected Pt Clusters*. Springer International Publisher: New York, **2014**.
32. Lyding, J. W.; Shen, T. C.; Hubacek, J. S.; Tucker, J. R.; Abeln, G. C., Nanoscale patterning and oxidation of H-passivated Si(100)-2×1 surfaces with an ultrahigh vacuum scanning tunneling microscope. *Appl. Phys. Lett.* **1994**, *64*, 2010-2012.

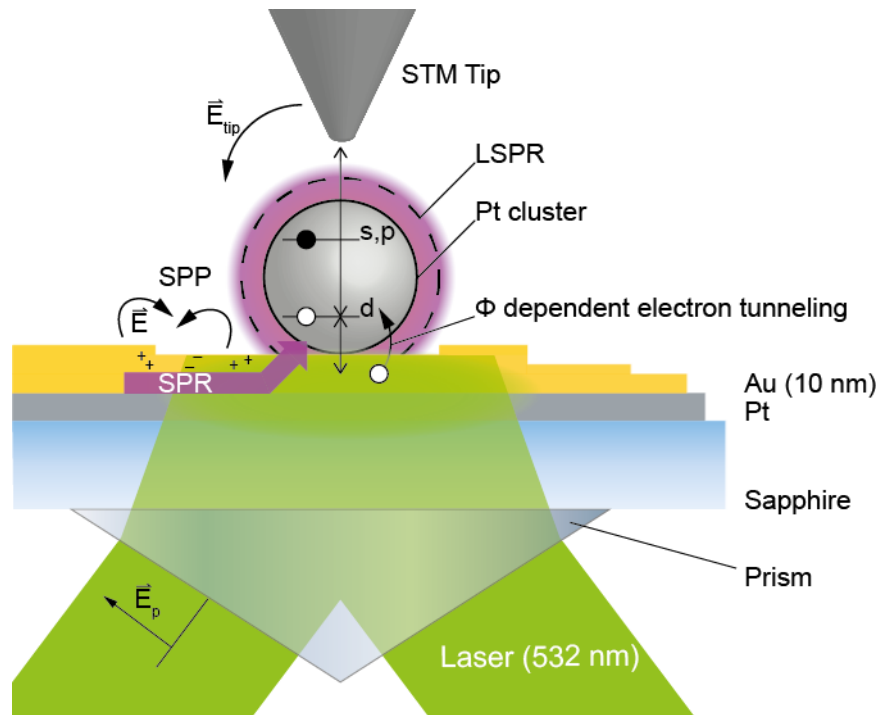


Figure 1 (Experimental schematic) Visible light is coupled through a prism and sapphire substrate onto the surface of the semi-transparent Au film by total internal reflection. A surface plasmon polariton and surface plasmon (SPR) is induced in the Au film by the visible light (left) and interacts with the ≈ 1 nm diameter Pt cluster (center). A LSPR is driven by excitation of d electrons in Pt. The change in local electron density caused by LSPR is detected by the STM tunneling current dependent on the tip bias applied (double arrows). Due to a slightly higher work function of the Pt clusters, their electron density can be enhanced by charging from the gold surface.

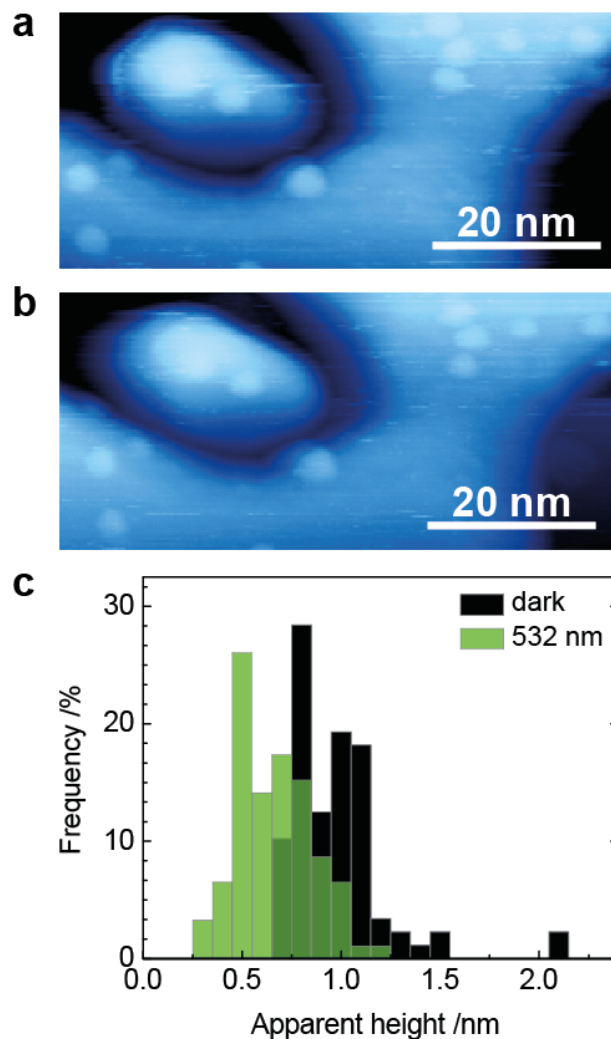


Figure 2 STM topography image of the Pt clusters taken (a) without (b) and with 532 nm illumination. When switching on the modulated illumination, we first observe a bias-independent tunneling current increase that leads to a net retraction of the tip. This effect is due to changes in tip photoconductivity and slight tip heating, and soon reaches a steady state. (c) In addition, the apparent cluster height drops by approximately 0.3 nm. The corresponding height distributions are based on at least 40 counted clusters. Scanning parameters: $I_t = 5$ pA, $V_t = 1$ V. Gold step edges do not change apparent height (Figure S5).

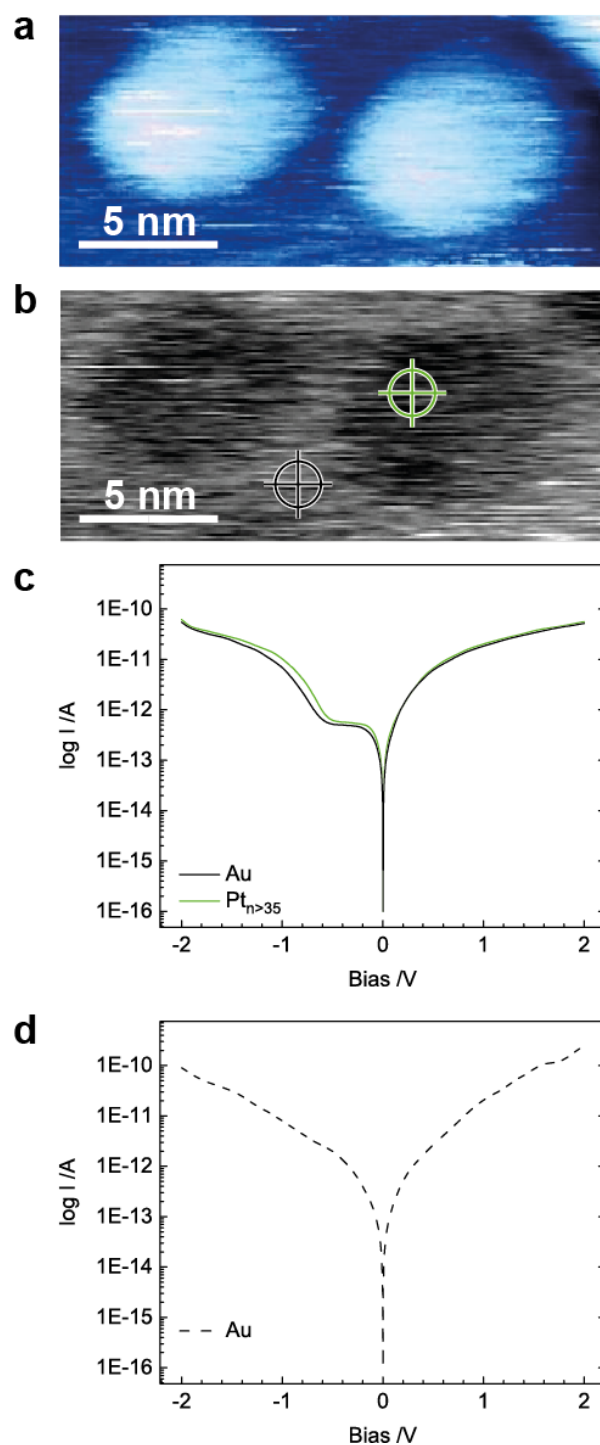


Figure 3 (a) STM topography image and (b) corresponding in-phase SMA-STM signal for Pt clusters on an Au film under 532 nm illumination. Although clusters cannot directly absorb the visible light, they show a net lock-in signal with respect to the Au surface; color scale from white (0.0 pA) to black (0.1 pA). The green and black cross-hair indicate the position where the STS of panel (c) were taken. Scanning parameters: $I_t = 5$ pA, $V_t = 1$ V. (c) I(V) spectra taken on the pure Au film (black curve) and on a supported Pt cluster (green curve), under illumination at 532 nm, with the feedback switched off. (d) Representative I(V) curve on a bare Au film without laser illumination.

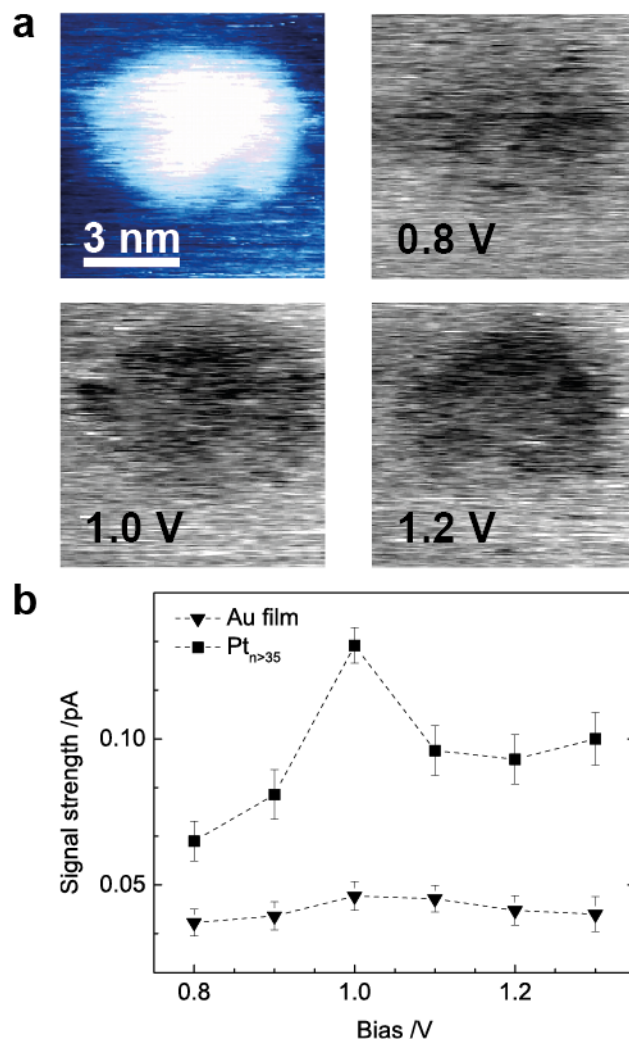


Figure 4 (a) STM topography image (top left) and in-phase SMA-STM signals measured at different sample biases. The average substrate signal has been subtracted and a color scale between white (-0.06 pA) and black (0.06 pA) is used. The tunneling current increases more on the clusters than on the gold support. Image sizes: 7 x 7 nm². (b) Plot of the SMA-STM signals averaged over the cluster in (a) or a similar-size area on the supporting Au film.

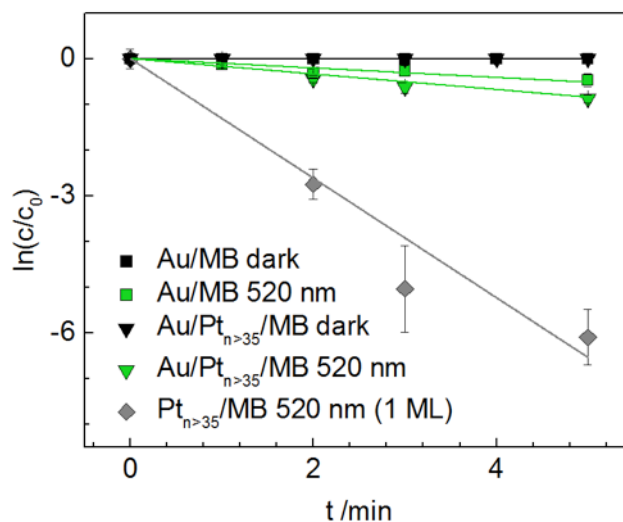
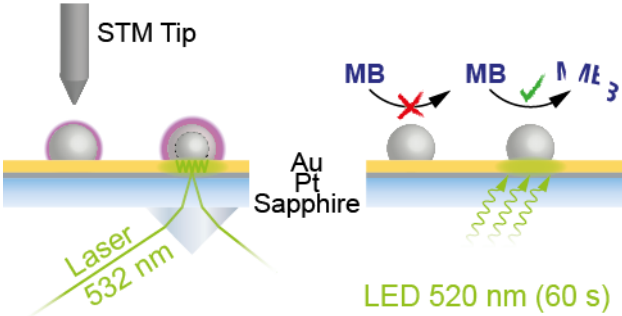


Figure 5 Oxidative decomposition of a dried methylene blue (MB) adlayer on a pure Au film (squares) and on a Au film with supported Pt clusters (triangles), in the dark (black) and under 520 nm illumination (green). The decomposition is quantified by the 657 nm MB extinction in the UV-VIS spectrum (calibration in SI Figure S6). Whereas the plasmonically active Au film itself is already capable of inducing the MB decomposition (green squares), this rate is further doubled by the additional 7% Pt cluster coverage (green triangles). The calculated reactivity on the Pt clusters alone, corrected for their small surface areas, is over an order of magnitude higher than the Au film (grey squares). Note that no reaction is observed in the dark on the gold film alone or with Pt clusters (black squares/triangles).

TOC Bild



Supporting Information

Plasmonic Activation of 1 nm Platinum Clusters for Photocatalysis

*S. Wieghold^{§, #}, L. Nienhaus^{&, †, #}, F. L. Knoller[§], F. F. Schweinberger[§], J. W. Lyding^{ⓔ, ^}, U. Heiz[§], M. Gruebele^{&, †, ⓑ, *}, F. Esch^{§, *}*

[§]Physical Chemistry and Catalysis Research Center, Chemistry Department, Technische Universität München, Lichtenbergstr. 4 and Ernst-Otto-Fischer-Str. 1, 85748 Garching, Germany

[&]Beckman Institute for Advanced Science and Technology, [†]Department of Chemistry, [^]Department of Electrical and Computer Engineering, and [ⓑ]Department of Physics, University of Illinois, Urbane, Illinois 61801

1. Extinction spectra and AFM image of gold layers of different thicknesses

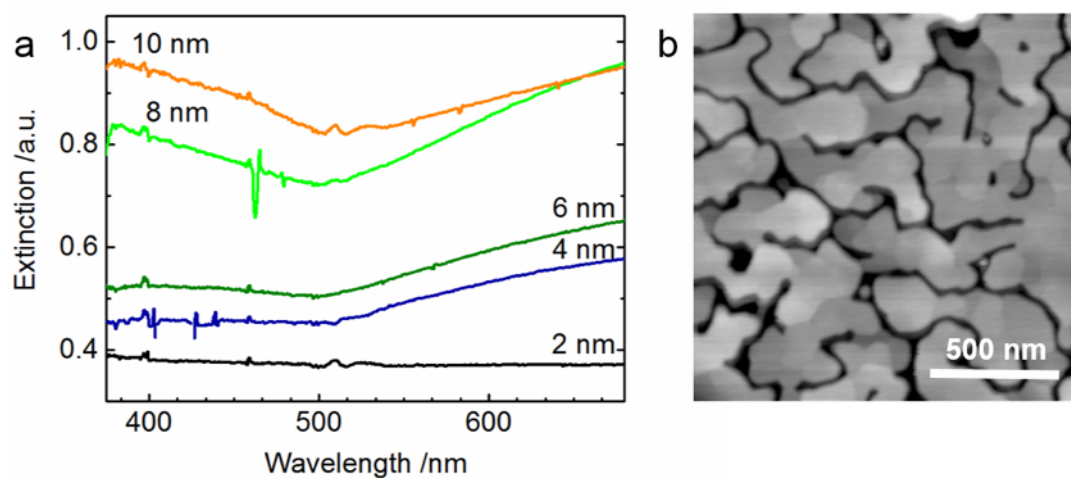


Figure S1 (a) UV-VIS spectra of gold films of different thicknesses supported by a Pt film (5 nm)/sapphire/prism support. The background extinction is due to reflectivity of the substrate-film interface. (b) AFM image of the corresponding 10 nm Au film showing the morphology of large, flat and interconnected islands. XPS showed no contamination of the Au surface by Pt.¹

2. Absorption of bare gold surfaces after annealing to 120° C

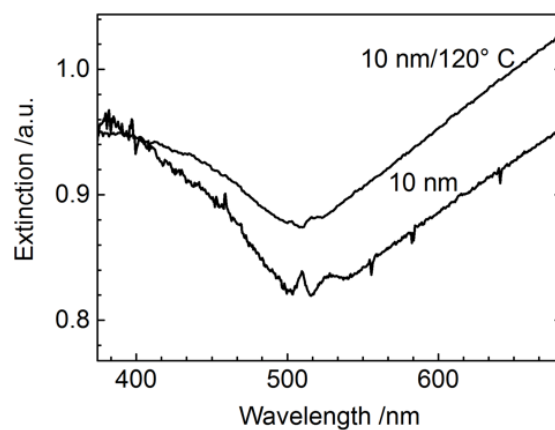


Figure S2 UV-VIS spectra of a 10 nm Au film with and without annealing in UHV to 120° C, the degassing temperature used for our samples before STM.

3. HAADF-STEM micrograph and statistical evaluation

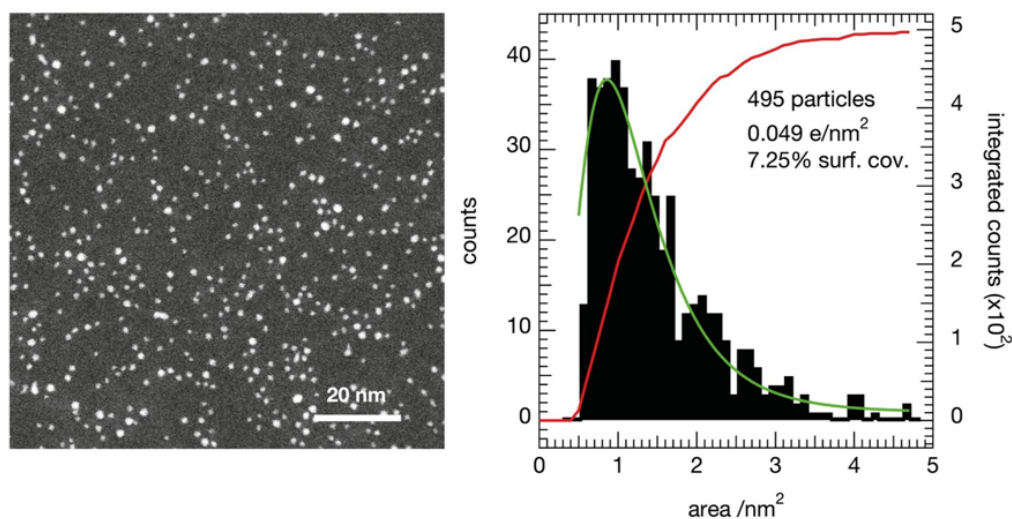


Figure S3 Representative high-angle annular dark field - scanning transmission electron microscope (HAADF-STEM) micrograph of $\text{Pt}_{n>35}$ clusters highlights the relatively homogenous size distribution (ca. 46 ± 10 atoms) of intact clusters achieved by mass high-pass filtering and soft landing conditions,^{2, 3} as well as the low (7.25%) surface coverage. The right plot shows the area distribution function along with a log-normal fit, well known for unselected cluster samples.⁴

4. Absorption of gold-supported Pt clusters

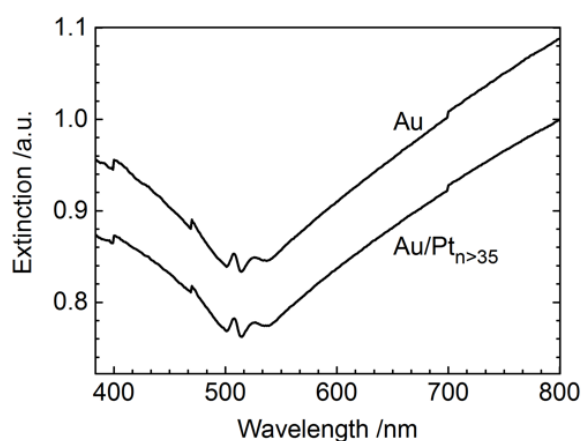


Figure S4 UV-VIS spectra of gold-supported Pt clusters.

5. STM evidence of plasmons on the gold surface

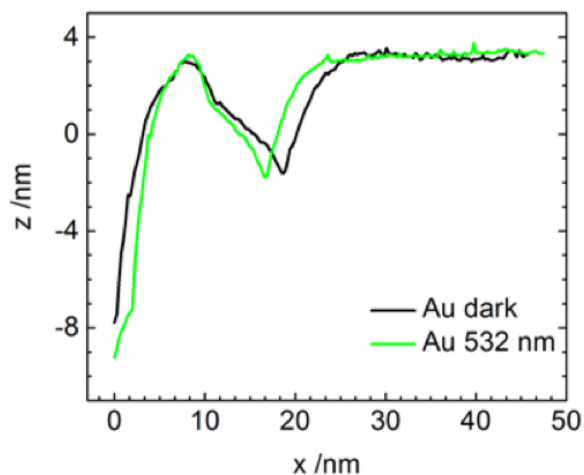


Figure S5 Step edge profiles of the Au support surface with (green) and without (black) laser illumination. No significant change in the step height is observed, indicating that excitation of surface plasmons on Au has the same electronic effect on both sides of a step, unlike the Pt-Au junction at a nanocluster, where apparent height of the Pt cluster decreases upon illumination.

6. Extinction spectra and calibration line of MB in ethanol

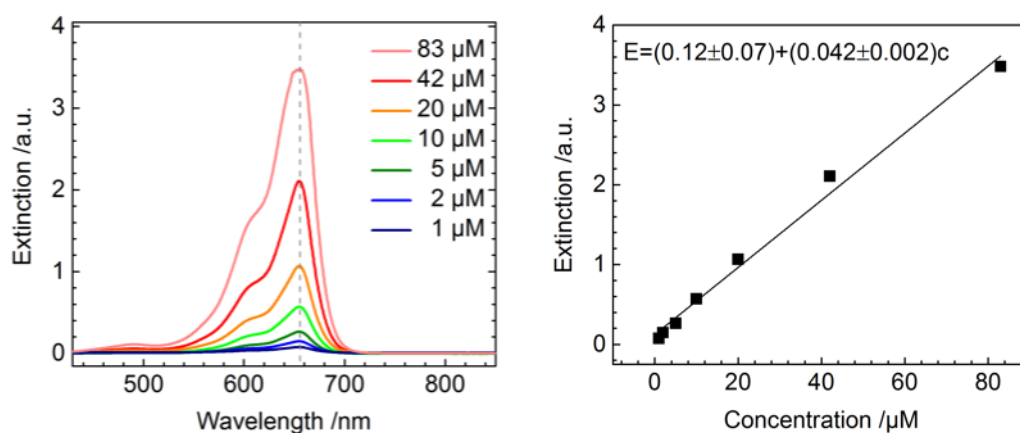


Figure S6 Left: UV-VIS spectra of MB in ethanol for different concentrations, showing a maximum at 657 nm (dashed line). Right: Calibration line for MB with indication of the fit parameters, based on the extinction value taken at 657 nm (left graph).

Additional SI References

1. Nienhaus, L.; Scott, G. E.; Haasch, R. T.; Wieghold, S.; Lyding, J. W.; Gruebele, M., Transparent Metal Films for Detection of Single-Molecule Optical Absorption by Scanning Tunneling Microscopy. *J. Phys. Chem. C* **2014**, *118*, 13196-13202.
2. Heiz, U.; Landman, U., *Nanocatalysis*. Springer-Verlag: Berlin Heidelberg, **2007**.
3. Schweinberger, F. F.; Berr, M. J.; Döblinger, M.; Wolff, C.; Sanwald, K. E.; Crampton, A. S.; Ridge, C. J.; Jackel, F.; Feldmann, J.; Tschurl, M.; Heiz, U., Cluster size effects in the photocatalytic hydrogen evolution reaction. *J. Am. Chem. Soc.* **2013**, *135*, 13262-13265.
4. Schweinberger, F. F., *Catalysis with Supported Size-selected Pt Clusters*. Springer International Publisher: New York, **2014**.

Conclusion

In this chapter, the coupling behavior of gold plasmons into metal clusters was presented providing further insights towards energy conversion systems. Since platinum clusters show a great potential to steer catalytic reactions, their use in light harvesting applications was demonstrated by decorating a plasmonically active thin gold film with unselected platinum clusters. The excitation and coupling was studied using a surface sensitive technique in combination with optical spectroscopy.

The presented results show that small clusters, which do not have an absorption in the visible range can be excited indirectly by plasmons of a gold surface. The excitation is observed in SMA-STM and additionally, in the oxidative decomposition of MB. The results pave the way towards quantum photonic applications since 'inactive' metal particles can be excited by plasmon polaritons which enhance photocatalytic reactions in the visible wavelength range. This investigations bear the potential to understand quantum-domain plasmonic systems towards nanoplasmonic device engineering on the nanoscale. Besides their use in conventional catalytic reactions, our results can impact the field of photoelectrochemistry towards novel anode materials.